2022

ROLE OF INHIBITION AND SPIKING VARIABILITY IN ORTHO- AND RETRONASAL OLFACTORY PROCESSING

Michelle F. Craft
Virginia Commonwealth University

ROLE OF INHIBITION AND SPIKING VARIABILITY IN ORTHO- AND RETRONASAL OLFACTORY PROCESSING

A Dissertation submitted in partial fulfillment of the requirements for the degree of Doctor of Philosophy at Virginia Commonwealth University.

by

MICHELLE F. CRAFT

M.S. in Mathematics at Virginia Commonwealth University – 2017-2020

B.S. in Mathematics at University of Mary Washington – 2012-2015

Advisor: Cheng Ly,

Associate Professor, Department of Statistical Sciences and Operations Research

Virginia Commonwealth University

Richmond, Virginia

December, 2022

Acknowledgements

Above all, I would like to thank my advisor, Dr. Cheng Ly, for not only providing me the wonderful opportunity to work on this research, but the immeasurable support without which this work would not exist. I would also like to thank our program director, Dr. Angela Reynolds, who always provided flexibility when my prior work schedule would not and whose guidance led me to this work that allowed me to focus my efforts full-time on completing this Ph.D.

Additionally, I would like to thank our collaborators: Dr. Andrea Barreiro, Dr. Woodrow Shew, and Dr. Shree Hari Gautam. I thank them for their work to collect, parse, analyze, and share the experimental data used throughout this work as well as their continued willingness to provide insightful feedback and helpful contributions to this research.

I also would like to thank my committee members: Dr. Kimberle Jacobs, Dr. Rebecca Segal, and Dr. Yanjun Qian. I could not have asked for a better, well-rounded expert committee to work with, and I thank you all for your time and efforts to review this work. I would also like to thank Dr. Anh Bui, I am ever grateful of the time you took to join in my proposal presentation as well as the feedback you provided.

Outside of academia, I would like to thank my family, friends, and future husband in supporting me on this journey. To Mama and Pa, even though the anti-algebra cartoon still hangs in your office, I am so fortunate to have had your love and support to guide me to who I am today and all that I have achieved. To all my friends, ones I've had for a lifetime and those I've made along the way, I am forever grateful for the fun and joy you've all brought to my life. Thanks for the coffee dates, early morning runs, VMFA picnics, pumpkin patch visit, calls, group chats, and beyond without which I would have struggled to maintain the healthy balance of work and play throughout this time. Finally to my future husband, Daniel, you are my rock, my biggest cheerleader, my shoulder to cry on, my listening ear when I need to

talk about all the thoughts and all the emotions, and the best dog dad to our girl, Scarlet. Thank you for all that you do and all that you are. I love you all!

TABLE OF CONTENTS

LIST OF TABLES

LIST OF FIGURES

Abstract

ROLE OF INHIBITION AND SPIKING VARIABILITY IN ORTHO- AND RETRONASAL OLFACTORY PROCESSING

By Michelle F. Craft

A Dissertation submitted in partial fulfillment of the requirements for the degree of Doctor of Philosophy at Virginia Commonwealth University.

Virginia Commonwealth University, 2022.

Advisor: Cheng Ly,

Associate Professor, Department of Statistical Sciences and Operations Research

Odor perception is the impetus for important animal behaviors, most pertinently for feeding, but also for mating and communication. There are two predominate modes of odor processing: odors pass through the front of nose (ortho) while inhaling and sniffing, or through the rear (retro) during exhalation and while eating and drinking. Despite the importance of olfaction for an animal's well-being and specifically that ortho and retro naturally occur, it is unknown whether the modality (ortho versus retro) is transmitted to cortical brain regions, which could significantly instruct how odors are processed. Prior imaging studies show different brain activity for the two modes, even with identical odors. However, odors are first processed via coordinated spiking of neurons in the olfactory bulb (OB) before being relayed downstream to higher cortical regions. Thus, we investigate responses of mitral cells (MC), one of principle neurons in OB, to ortho and retro stimulus to elucidate how the OB processes and codes this information.

We analyze our collected in vivo rat data to inform modeling of the OB circuitry and

MC responses to both modes of olfaction. Our efforts show that the OB does indeed process odors differently and that the temporal profile of each stimulus route to the OB is crucial for distinguishing ortho and retro odors. Additionally, we detail the rich spiking dynamics observed in our MC model and use a phenomenological model to explain the unexpected non-monotonic spike variability observed as weak-to-moderate background noise increases. Lastly in both anesthetized and awake rodents, we show that MCs with synaptic connections to cortical regions reliably transmit ortho versus retro input stimulus information. Drug manipulation affecting $GABA_A$-mediated synaptic inhibition leads to changes in decoding of ortho/retro and only affects firing response for one of the two modes. We have not only shown that ortho versus retro information is encoded to downstream brain regions, but with models and analysis, we uncover the network dynamics that promote this encoding.

CHAPTER 1

INTRODUCTION

1.1 Background information

Flavor perception is a fundamental governing factor of feeding behaviors and associated diseases such as obesity. Smells that enter the nose retronasally, i.e. from the back of the nasal cavity, play an essential role in flavor perception, yet the neuroscience of retronasal olfaction is only beginning to be understood. Pioneering studies, based on human psychophysics and neuroimaging, have demonstrated that retronasal olfaction and orthonasal olfaction (nasally inhaled smells) involve distinctly different brain activation, even for identical odors [1, 2, 3]. However, the neural mechanisms underlying differences between retro- and orthonasal information processing are largely unknown.

Olfaction occurs when odorant molecules enter the nasal cavity retro- or orthonasally creating action potentials within the olfactory receptor neurons (ORNs) that send electric signals through the olfactory system. The axons of these ORNs end at the olfactory bulb (OB), where they converge on the dendrites of OB neurons in small clusters called glomeruli. In the glomerular layer, reciprocally connected mitral cells (MCs) and periglomerular cells (PGCs) form connections with ORNs in order to receive olfactory information from the ORNs and transport it to the external plexiform layer (EPL) of the OB. The connection from the glomerular layer to the EPL is constructed by reciprocal synaptic interactions between the MCs and granule cells (GCs). The information is finally sent to the olfactory cortex, the main site for the processing of olfactory information [4].

Prior experiments demonstrated how synaptic input to the OB in the nose differs for retro- versus orthonasal olfaction in rats [5, 6, 7, 8]. However, perception and coding of

retronasal smells dependent on the closely located neural spikes in OB, have not yet been investigated. Thus, the following questions remain: How do spiking statistics differ between retro- and orthonasal olfaction and what are potential sources for these differences? How do neurons in OB encode retronasal stimuli? Our work addresses these questions, dramatically advancing current understanding of retronasal olfaction.

The primary purpose of this research is to determine how OB inhibitory interactions impact dynamics of retro- and orthonasal selectivity. For the first time, our results determine differences between retro- and orthonasal neural spiking responses at the level of MCs, PGCs, and GCs. Additionally, we explore how the circuit mechanisms and external input causes differences between retro- and orthonasal spike count statistics. These results are validated and compared to empirical data collected *in vivo*.

1.2 Outline

In chapter 2, we present single-compartment biophysical OB model that is able to reproduce key properties of important OB cell types. Given insights from prior studies, the OB model captures the salient trends observed in our *in vivo* rat data. Further, we analyse how first and second order input statistics to the OB dynamically transfer to output statistics from the OB with a phenomenological linear-nonlinear filter model.

In chapter 3, we study the spike response of a single compartment biophysical MC model described in chapter 2 subject to constant current input with background white noise. The spike dynamics of the MC model with noise are analyzed and additionally explained using a phenomenological model of the interspike interval (ISI) probability density function.

In chapter 4, we present analysis of *in vivo* rat data individual cell decoding accuracy of ortho versus retronasal stimulus given different inhibitory drugs (no drug, drug-induced inhibition, drug-reduced inhibition). The data insights inform the construction of a simple firing rate model that includes synaptic plasticity to enhance differing inhibitory drug effects.

Finally, we present findings of an analogous analysis of awake mice data to compare the decoding and role of inhibition of ortho and retronasal stimulus in relation to the breath cycle.

CHAPTER 2

DIFFERENCES IN OLFACTORY BULB MITRAL CELL SPIKING WITH ORTHO- AND RETRONASAL STIMULATION REVEALED BY DATA-DRIVEN MODELS

2.1 Introduction

This work is a published article in the journal Public Library of Science (PLoS) Computational Biology [9].

Olfactory processing naturally occurs in two distinct modes: orthonasal (**ortho**) where odors enter the front of the nasal cavity and retronasal (**retro**) where odors enter the rear through the throat. Orthonasal olfaction is essential for avoiding predators [10, 11], social interactions, and finding food, and has been studied most extensively in olfaction research. Retronasal olfaction is far less studied, but has a critical role in eating behaviors as chewed foods generate odorants that enter the nasal cavity upon exhalation. Retronasal olfaction drives flavor perception [12, 13, 14] and aids in avoiding harmful foods. Moreover, studies have shown that olfactory dysfunction with food odors is directly linked to obesity [15, 16, 17]. Previous studies have reported differences in cortical fMRI BOLD signals for ortho versus retro stimuli [2] and recent evidence suggests that food odors are easier to recognize when delivered retronasally versus orthonasally [18]. Calcium imaging studies have shown that the input to olfactory bulb from the nose differs for ortho versus retro stimulation [6]. However, the neural mechanisms that differentiate ortho versus retro olfactory processing at the level of spiking activity in olfactory bulb remain unknown.

Odor information is primarily processed in the olfactory bulb (**OB**) and then subsequently relayed to cortical areas via mitral cell (**MC**) (and tufted cell) spiking. Thus, any

differences in MC spiking between ortho and retro are related to both the efficiency and accuracy [19, 20, 21, 22] of odor coding, but any such differences are largely unknown. Presynaptic to the OB are olfactory receptor neurons (**ORN**s) whose activity is known to differ for ortho versus retro stimulation, as observed in prior imaging studies with fMRI [23], calcium imaging [6], and optical imaging in transgenic mice [24]. These and other prior studies [25, 26, 27] suggest that ORN synaptic inputs is a key factor for differences in OB activity. The two routes of stimulation make contact on different locations of the olfactory epithelium (shown in light green in Fig 2.1 experimental diagram) and thus activate different ORN receptor types within the epithelium. However, the implications of these differences in ORN activity for MC spiking have yet to be explored.

We perform *in vivo* recordings of rat OB mitral cells using multi-electrode arrays with a food odor (Ethyl Butyrate) stimulus, delivered by both modes of stimulation, to determine whether differences exist. We find significant differences in odor-evoked MC spiking with ortho versus retro stimulation in both firing rate (larger with retro) and spike count covariance (larger with ortho). However, understanding how retro stimulation can elicit both larger firing rates and smaller co-variablity than ortho is generally difficult in reciprocal networks because of the numerous attributes that shape spike statistics [28, 29, 30, 31]. Additionally, dissecting how components of ORN inputs alter OB spiking is difficult experimentally due to the complexity of both the reciprocal circuitry in the OB [32, 33] and resulting spatiotemporal ORN responses [25, 27]. So we develop a single-compartment biophysical OB model that accounts for differences in ORN input to investigate how they affect MC spiking responses. Specifically, we model ORN input as a time-varying inhomogeneous Poisson Process [34], where the input rate has slower increase and decay for retro than ortho [24, 6], and the ORN input correlation is smaller for retro than ortho [24, 6]. With these specifications, our biophysical OB network model is able to capture the salient ortho versus retro MC spiking response trends in our experimental data.

However, our biophysical OB model is too complex to directly analyze mathematically in order to address the neural encoding problem of characterizing how MCs convert ORN input to spike responses. We use a simple linear-nonlinear (**LN**) model framework to assess how our biophysical OB network transfers input statistics (from ORN) to outputs (MC spike statistics). We find that the linear filter component of the LN model, i.e., convolution with ORN inputs, consistently has larger absolute values with retro than with ortho input. Thus the OB network model is more sensitive to ORN fluctuations with retro-like inputs than with ortho. Finally, we use our models to examine which key attribute(s) of ORN inputs (temporal profile, amplitude, input correlation) are most significant for capturing our data. We find that temporal profile is the critical attribute for ortho versus retronasal stimulus response.

This work provides a framework for how to analyze the sources driving different OB spiking responses to different modes of olfaction, as well as important insights that have implications for how the brain codes odors.

2.2 Material and methods

See `https://github.com/michellecraft64/OB` for MATLAB code implementing the single-compartment biophysical model, the equations for synaptic input statistics, and the linear-nonlinear (LN) model.

2.2.1 Single-compartment biophysical OB model

We consider two glomeruli each with a representative MC, periglomerular cell (**PGC**), and granule cell (**GC**) (see Fig 2.2B). Models of all three cell types (MC, PGC, GC) are based on models developed by the Cleland Lab [35, 36]. Each cell is a conductance-based model with intrinsic ionic currents. The voltage responses of all three cell types, measured in experiments and in a multi-compartment model [35, 36], are generally captured in our

single-compartmental model, see Fig 2.2A. Here we describe all of the pertinent model details thoroughly; for other extraneous details and implementation, please refer to provided code on GitHub.

2.2.1.1 Individual cell model

$$C_j \frac{dV_j}{dt} = I_{j,\text{App}} - \sum I_{j,\text{Ion}} - \sum I_{j,\text{Synapse}} - \sum I_{j,\text{ORN}}, \tag{2.1}$$

The voltages of all model cells are governed by a Hodgkin-Huxley type current balance equation (Eq (2.1) above for the j^{th} cell) consisting of voltage (V), membrane capacitance (C), applied current (I_{App}), ionic currents (I_{Ion}), synaptic currents (I_{Synapse}), and ORN inputs (I_{ORN}); see Table 12 for units and numerical values. For our modeling purposes, the ionic currents and the ORN inputs are modified from [35, 36] and described below.

2.2.1.2 Ionic currents

$$I_i = g_i m^p h^q (V - E_i), \tag{2.2}$$

The ionic currents are defined by Eq (2.2) above (for specific ion type i) and account for maximal conductance (g), activation variable (m) with exponent (p), inactivation variable (h) with exponent (q), time-varying voltage (V assumed to be isopotential), and reversal potential (E_i). All parameters and function for intrinsic ionic currents and their gating variables are the same as in [35, 36] with the exception of maximal conductance. We chose to condense the model as defined in [35, 36] by collapsing all compartments to a single-compartment, and we set the maximal conductance as the sum of all maximal conductance values (e.g., in PGC, I_{Na} has maximal conductance $g_{\text{Na}} = 70\,\text{mS/cm}^2$ because [35] set $g_{\text{Na}} = 50\,\text{mS/cm}^2$ in

the soma and $g_{\mathrm{Na}} = 20\,\mathrm{mS/cm^2}$ in the spine). All summed maximal conductance values used are listed for reference in Table 12. The calcium dynamics used to define the calcium-related ionic currents are the same as in [35, 36].

2.2.1.3 Synaptic currents

$$I_{\mathrm{syn}} = w g_{\mathrm{syn}} s B(V)(V - E_{\mathrm{syn}}), \tag{2.3}$$

$$\frac{ds}{dt} = \alpha F(V_{\mathrm{pre}})(1 - s) + \beta s, \tag{2.4}$$

Eqs (2.3) and (2.4) are the equations for the synaptic variables, where all presynaptic GCs and PGCs provide $\mathrm{GABA_A}$ inputs, and all presynaptic MCs provide both AMPA and NMDA inputs. $B(V)$ in Eq (2.3) is the NMDA-specific magnesium block function ($B(V) = 1$ for all other synapses), and $s(t)$ is the fraction of open synaptic channels. The channel opening rate constants (α and β) are normalized sigmoidal function of presynaptic membrane potential ($F(V_{\mathrm{pre}})$ in Eq (2.4)), the same as in [35, 36]. We also define the conductance parameter (g_{syn}) and reversal potentials (E_{syn}) as [35, 36] have, with $g_{\mathrm{GABA}} = 1.5\,\mathrm{nS}$ for GC→MC synapses, $g_{\mathrm{GABA}} = 2\,\mathrm{nS}$ for PGC→MC synapses, $g_{\mathrm{AMPA}} = 2\,\mathrm{nS}$ and $g_{\mathrm{NMDA}} = 1\,\mathrm{nS}$ for both MC→PGC and MC→GC synapses; $E_{\mathrm{syn}} = 0\,\mathrm{mV}$ for AMPA and NMDA currents, and $E_{\mathrm{syn}} = -80\,\mathrm{mV}$ for $\mathrm{GABA_A}$ currents.

2.2.1.4 ORN input

$$I_{\mathrm{ORN}} = S(t)(V - E_X), \tag{2.5}$$

$$\tau_X \frac{dS}{dt} = -S + a_X \tau_X \sum_j \delta(t - t_k), \tag{2.6}$$

The ORN inputs for each cell consist of both excitatory and inhibitory inputs as specified

in Eqs (2.5) and (2.6) where $X \in \{E, I\}$. The reversal potential value (E_X) is much larger for excitatory inputs and smaller for inhibitory. The function $S(t_k^+) = S(t_k^-) + a_X$ accounts for the random times (t_k) when S instantaneously increases by a_X. The random times, t_k, are governed by an inhomogeneous Poisson process with rate $\lambda_X(t)$. This aligns with experimental evidence that ORN spiking is Poisson-like in the spontaneous state [34]. Thus, we extend the notion that ORN spiking would be Poisson-like in the evoked state with increased rate $\lambda_X(t)$ varying in time. Finally, we set the synaptic rise and decay time constants (τ_X) to be 5.5 ms for PGCs and GCs, 10 ms for MCs, as in [35, 36].

The ORN input rates can be pairwise correlated, which is achieved by the parameter $c_{j,k} \in [0, 1]$, for cells j and k detailed by Eq (2.7) below:

$$\lambda_j(t) = \tilde{\lambda}_j(t) - \bar{\lambda}(t)c_{j,k}(t). \tag{2.7}$$

where $\tilde{\lambda}_j(t)$ and $\tilde{\lambda}_k(t)$ are the individually defined ORN input rates for cells j and k, and $\bar{\lambda}(t) := \min(\tilde{\lambda}_j(t), \tilde{\lambda}_k(t))$.

2.2.2 Fitting biophysical network model to data

The biophysical OB model described thus far was adopted directly from Li & Cleland, aside from our single-compartment simplification where we lumped all ionic currents into one compartment and used the sum of the (maximal) conductances from all compartments. Here we describe how the network model was tuned to capture the salient features of our experimental data. We did not systematically consider large volumes of parameter space due to the enormous computational resources required for 50,000 simulations of the model for each parameter set to accurately simulate the spike count statistics. After model parameters were set, the only manual tuning we did was to consider several Poisson input rates $\lambda_{O/R}(t)$ (see Eqs (2.5)–(2.7)) for the ORN input synapses (see Fig C.3) – even the ORN input correlations $c_{j,k}(t)$ that we arbitrarily chose were fixed throughout.

Note that we did not further tune the intrinsic properties of the individual cells; the PGC, MC, and GC parameters are as stated above with behavior shown in Fig 2.2A.

2.2.2.1 Specifying coupling strengths

We used the same equations for the synaptic variables as Cleland [36], but set the coupling strengths w (see Eq (2.3)) to: $w_{M\leftarrow G} = 3$ (independent inhibition), $w_{M\leftarrow Gc} = 0.3$ (common inhibition to MC), $w_{G\leftarrow M} = 1$ (same for both AMPA, NMDA), $w_{Gc\leftarrow M} = 0.5$ (inhibition to common GC), $w_{P\leftarrow M} = 1$ and $w_{M\leftarrow P} = 2$ (same for both AMPA, NMDA). These coupling strengths were chosen in part from results in Ly et. al [37] who used a related/simpler OB network model with the same 2 glomeruli architecture to find regions of parameter space that best fit orthonasal experimental data. Similar to Ly et. al [37] (see their Figs 2, 3, and 6), we set independent inhibition from GC to MC to be greater than excitation from MC to GC, and shared GC inhibition to MC to be relatively weak (i.e., $w_{Gc\leftarrow M} \leq w_{G\leftarrow M} \leq w_{M\leftarrow G}$). The coupling strengths were never tuned, they were fixed throughout.

2.2.2.2 Specifying ORN input

The ORN inputs (Eqs (2.5)–(2.7)) consists of a Poisson input rate, and input correlation between pairs of cells. We set the correlation ($c_{j,k}$) between the following cell pairs: MC and PGC pair within a glomerulus have $c_{j,k} = 0.3$ because they receive inputs from the same ORN cells; the two MCs have correlated ORN input [38] ($c_{j,k}(t)$ time-varying as in Fig 2.2Cii); and between all 3 GCs because they are known to synchronize [36, 39] ($c_{j,k} = 0.3$ for all 3 different pairs of GCs). All other pairs of cells have no ORN input correlation. Note that input correlation for the 2 MCs increased with odor to mimic increased correlation of glomeruli activity. In Fig 2.2Cii, input correlation for the 2 MCs are constrained such that $c_R(t) < c_O(t)$. This is based on prior imaging studies that show retronasal stimulation

activates spatially smaller regions of glomeruli inputs than orthonasal, and that the activation regions from retro are subsets of ortho [24, 6]. For specific algebraic formula of $c_{R/O}(t)$, please refer to code on GitHub.

We considered several different $\lambda_{O/R}(t)$, the inhomogeneous Poisson input rate of t_k in Eq (2.6) (with constraints described below) and chose the ones that best matched the time-varying firing rates (Fig 2.7A). The ortho- vs. retronasal odor input rates, $\lambda_{O/R}(t)$, are constrained such that $\lambda_O(t)$ increases faster and more abruptly than $\lambda_R(t)$ with odor, and $\lambda_R(t)$ decays slower than $\lambda_O(t)$; this is all based on ORN imaging studies [24, 6]. Inputs consist of both excitatory synapses (with rate $\lambda_{O/R}(t)$) and inhibitory synapses (with rate $0.75\lambda_{O/R}(t)$) to capture other unmodeled inhibitory effects.

To first understand how MC firing rates depends on $\lambda(t)$ without any consideration for ortho or retro, we used a simple alpha-function form in the evoked state: $\lambda(t) = te^{-t/\tau}$, surveying 6 different τ (see Fig C.3A, left). The resulting MC firing rates (Fig C.3A, right with 2,000 realizations) was informative for how to manually set the input values (spontaneous, peaked-evoked, etc.). Fig C.3B shows all of the $\lambda_{O/R}(t)$ we tried, notice that they all satisfy the constraints described above. Via trial and error with 2,000 realizations, we only looked at the resulting firing rates (PSTH), insuring the simulations matched the ortho data well. We were fortunate in fitting the retro firing rate data, trying only 2 $\lambda_R(t)$. The other spike statistics (e.g., covariance, Fano factor) were never accounted for in our consideration of different $\lambda_{O/R}(t)$, which is perhaps why the fit to the spike covariance data is so bad.

2.2.3 Calculating time-varying ORN input statistics of synapses

Here we describe a method to capture the effects of ORN input statistics of synapses to the biophysical OB model, in the limit of infinite realizations. These methods are very useful as inputs for the LN model, without which one would have to use averages from Monte Carlo simulations that contain deviations from finite size effects. Taking the expected value of Eq

(2.6) results in an equation for the average of $S(t)$, $\mu_S(t)$:

$$\tau_X \mu_S(t) = -\mu_S + \tau_X a_X \lambda(t), \tag{2.8}$$

To derive the equation for variance $\sigma_S^2(t)$, we multiply Eq (2.6) by itself. We can equivalently rewrite Eq (2.6) as an integral:

$$S(t) = a_X \int_{-\infty}^{t} e^{-(t-u)/\tau_X} D(u)\, du, \tag{2.9}$$

where $D(t) := \sum_j \delta(t - t_k)$. So

$$S^2(t) = (a_X)^2 \int_{-\infty}^{t}\int_{-\infty}^{t} D(u)D(v)e^{-(t-u)/\tau_X} e^{-(t-v)/\tau_X}\, dudv \tag{2.10}$$

Recall that $\mathbb{E}\left[D(u)D(v)\right] = \lambda(v)\delta(u-v) + \lambda(u)\lambda(v)$, so we have:

$$\begin{aligned} \mathbb{E}\left[S^2(t)\right] &= (a_X)^2 \int_{-\infty}^{t} \lambda(v) e^{-2(t-v)/\tau_X}\, dv + \Big(\mu_S(t)\Big)^2 & (2.11)\\ \Rightarrow \sigma_S^2(t) &= (a_X)^2 \int_{-\infty}^{t} \lambda(v) e^{-2(t-v)/\tau_X}\, dv, & (2.12) \end{aligned}$$

Equivalently, $\sigma_S^2(t)$ satisfies the ODE:

$$\tau_X \frac{d\sigma_S^2(t)}{dt} = -2\sigma_S^2 + \tau_X (a_X)^2 \lambda(t), \tag{2.13}$$

Similarly for $S_j(t)S_k(t)$ correlated synapses, we have:

$$S_j(t)S_k(t) = \left(a_{X_j} a_{X_k}\right) \int_{-\infty}^{t}\int_{-\infty}^{t} D(u)D(v)e^{-(t-u)/\tau_{X_j}} e^{-(t-v)/\tau_{X_k}}\, dudv, \tag{2.14}$$

By our model construction $\mathbb{E}\left[D(u)D(v)\right] = c_{j,k}(v)\bar{\lambda}(v)\delta(u-v) + \lambda_j(u)\lambda_k(v)$, where

$\bar{\lambda}(t) := \min(\lambda_j(t), \lambda_k(t))$, so we have:

$$\mathbb{E}[S_j(t)S_k(t)] = \left(a_{X_j}a_{X_k}\right)\int_{-\infty}^{t} c_{j,k}(v)\bar{\lambda}(v)e^{(-\tau_{X_j}-\tau_{X_k})(t-v)/(\tau_{X_j}\tau_{X_k})}\,dv + \mu_{S_j}(t)\mu_{S_k}(t) \tag{2.15}$$

$$\Rightarrow \mathrm{Cov}(S_j(t), S_k(t)) = \left(a_{X_j}a_{X_k}\right)\int_{-\infty}^{t} c_{j,k}(v)\bar{\lambda}(v)e^{(-\tau_{X_j}-\tau_{X_k})(t-v)/(\tau_{X_j}\tau_{X_k})}\,dv, \tag{2.16}$$

$\mathrm{Cov}(S_j(t), S_k(t))$ equivalently satisfies the ODE:

$$\tau_{X_j}\tau_{X_k}\frac{d\mathrm{Cov}(S_j(t), S_k(t))}{dt} = -(\tau_{X_j}+\tau_{X_k})\mathrm{Cov}(S_j(t), S_k(t)) + (\tau_{X_j}\tau_{X_k})\left(a_{X_j}a_{X_k}\right)c_{j,k}(t)\bar{\lambda}(t), \tag{2.17}$$

The calculations for the dynamic (time-varying) synapse statistics are important for capturing realistic statistics because a steady-state approximation can be very inaccurate, especially when the time-varying correlation and ORN spiking rate change quickly relative to the time-scales (τ_X). The quasi-steady-state approximation is:

$$\mu_S(t) \approx \tau_X a_X \lambda(t) \tag{2.18}$$

$$\sigma_S^2(t) \approx \frac{\tau_X (a_X)^2 \lambda(t)}{2} \tag{2.19}$$

$$\mathrm{Cov}(S_j(t), S_k(t)) \approx \frac{\tau_{X_j}\tau_{X_k}}{\tau_{X_j}+\tau_{X_k}} a_{X_j}a_{X_k}c_{j,k}(t)\bar{\lambda}(t) \tag{2.20}$$

Fig C.4 shows several more examples demonstrating the accuracy of the calculations (Eqs (2.8), (2.13), (2.17)) and how inaccurate Eqs (2.18)–(2.20) can be.

2.2.4 Linear-Nonlinear (LN) model: numerical details

We use the above described ODEs (Eqs (2.8), (2.13), and (2.17)) to simplify the calculations of ORN input statistics for use with the LN model framework. Previous work has implemented LN-type models as an alternative to biophysical spiking models with various conditions (see [40, 41, 42] and Subsection 2.4 Discussion). Fig 2.4A illustrates a schematic of the LN model parameters, linear filter (k) and shift (b), that are used with the ORN input

statistics ($X \in \{\mu_S,\ \sigma_S^2,\ \mathrm{Cov}(S_1, S_2)\}$) in order to construct an approximation (Y) to the biophysical OB network model's output MC spike statistics (PSTH(t), σ_R^2, Cov(R_1, R_2)).

The LN model is summarized as:

$$Y(t) = f\left(\int_{-\infty}^{t} k(\tau - t)X(\tau)d\tau + b\right) \tag{2.21}$$

Where we define our function f as an exponential, and we can approximate the integral numerically as follows:

$$\int_{-\infty}^{t} k(\tau - t)X(\tau)d\tau + b \approx \sum_{l=0}^{n-1} \vec{k}(l)\vec{X}(j - l)\,\Delta\tau + \vec{b} \tag{2.22}$$

Where n denotes the number of time points included in the linear filter, and j denotes the points in time of input statistic $\vec{X}$ of size Lt. Then, we can rewrite Eq (2.22) in matrix vector form $A\vec{w} = \vec{v}$ where: A is the Toeplitz matrix of size $(\mathrm{Lt} - n + 1) \times n$ of our input statistic ($\vec{X}$) with an additional row of value one to account for shift; $\vec{w}$ is our linear filter ($\vec{k}$) and shift ($\vec{b}$); and $\vec{v}$ is our OB network MC spike statistic to which we fit our filter. Then, we solve for $\vec{w}$ using Least Squares approximation by QR decomposition. The linear filter ($\vec{k}$) converges to 0 by construction, therefore we truncate the filter at $-0.1\,\mathrm{s}$ and set $k = 0$ for the remaining time $-1 \leq t < -0.1$. Then, the LN output approximation (Y) of the MC spike statistic is calculated as follows:

$$Y(t) = f\left(K \cdot \vec{X} + \vec{b}\right) \tag{2.23}$$

Where K denotes the convolutional matrix constructed from the truncated linear filter k.

2.2.5 Electrophysiological recordings

We decided to use recordings from a single rat, with recordings from 3 sessions. We took this conservative approach to control differences in nasal cavity structure that can vary across rats [43, 44], which may shape differences in ortho versus retro activity [6, 45]. See provided

GitHub code for statistical summary of experimental data. Additionally, see Appendix A for details on collecting *in vivo* rat OB data.

2.3 Results

We performed *in vivo* multi-electrode array recordings of the OB in the mitral cell layer of anesthetized rats (see Appendix A for details) to capture odor evoked spiking activity of populations of putative MCs. This yielded a large number of cells (94) and simultaneously recorded pairs of cells (1435) with which to assess population average spiking statistics. The spike statistics are trial-averaged responses of a rat to a single odorant, Ethyl Butyrate (food odor). We focus on a food odor because they dominate retronasal smells, and a recent study showed that humans can more accurately detect food odors (vs. non-food odors) delivered retronasally [18]. In addition, an fMRI study showed different cortical activity [2] in humans for ortho versus retronasal stimulus, specifically with food odors.

The first and second order spike statistics are summarized in Fig 2.1, including the firing rate (peri-stimulus time histogram, **PSTH**, Fig 2.1A), the spike count variance (Fig 2.1B), the spike count covariance (Fig 2.1C), Fano Factor (variance divided by mean, Fig 2.1D), and Pearson's correlation (Fig 2.1E). For each cell and simultaneously record pair of cells, we calculated the trial-averaged spike statistics with half-overlapping 100 ms time windows. The time window 100 ms is an intermediate value between shorter (membrane time constants, AMPA, $GABA_A$, etc.) and longer time scales (NMDA, calcium, and other ionic currents) known to exist in the OB.

We find statistically significant differences between ortho and retro stimulation in almost all of the first and second order MC spike count statistics. At odor onset, orthonasal stimulation elicits larger firing rates with a faster rise than retronasal, after which retronasal firing is larger and remains elevated longer than with orthonasal. These trends are consistent with imaging studies of the glomeruli layer in OB in transgenic mice (see [24], their

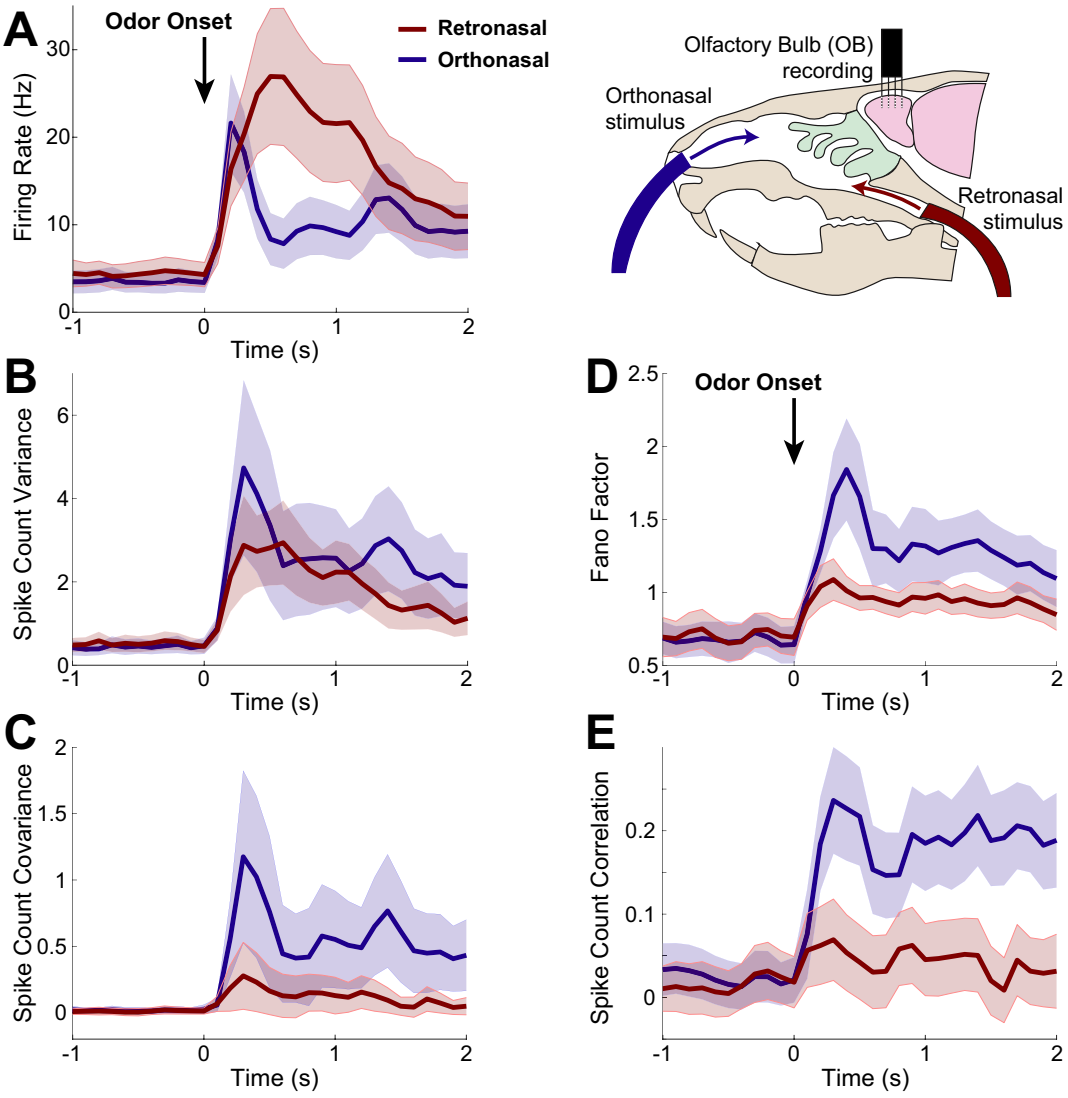

Fig. 2.1.: Spike statistics from *in vivo* multi-electrode array recordings.

Population average spike statistics for orthonasal (blue) and retronasal (red) with stimulus onset at time $t = 0\,\mathrm{s}$ as indicated by black arrow for 1 s duration. A) Firing rate (Hz) is statistically significantly different between ortho and retro for the duration of the evoked period ($0.4 \leq t \leq 1.1\,\mathrm{s}$). B) Spike count variance has no statistically significant difference between ortho and retro. C) Covariance of spike counts are statistically significant different throughout the evoked state ($0 \leq t \leq 2$) with ortho having larger values. Scaled measures of variability shown for completeness: Fano Factor (D) is the variance divided by mean spike count, and Pearson's correlation (E) is the covariance divided by the product of the standard deviations; both are also different with ortho versus retro. Spike counts in 100 ms half-overlapping time windows averaging over all 10 trials. Significance: two-sample t-tests (assuming unequal variances) for each time bin to assess differences in population means, $p < 0.01$, also see Figs C.1 and C.2. From 94 total cells and 1435 simultaneously recorded cell pairs; shaded regions show relative population heterogeneity: $\mu \pm 0.2$std (standard deviation across the population/pairs after trial-averaging; 0.2 scale for visualization).

figure 2) as well as EOG recordings of the superficial layers of the OB in rats (see [26], their figure 7). More specifically, we find statistical significance ($\alpha = 0.01$) between ortho- and retronasal firing rate after and for the duration of the odor stimulation. We also find that MC spike count covariance for ortho is significantly larger than retro for the entirety of the evoked state. MC spike count variance, however, is not significantly different. Note that we specifically tested whether the population averages (averaged over all cells for PSTH and spike variance, over all simultaneously recorded pairs for spike covariance) are significantly different between ortho and retro, via a two-sample t-test assuming unequal variances with the null hypothesis of equal population averages (see Fig C.1). Further, we calculated Cohen's d value to measure effect size [46], and find medium effect size for the majority of the evoked time period for all spike statistics considered except for variance, see Fig C.2.

Hereafter, we mainly focus on understanding the differences in firing rate and spike count covariance because they directly impact common coding metrics (e.g. the Fisher information) in contrast to scaled measures of variability (Fano factor and Pearson's correlation) that are nonlinear functions of the entities that impact coding [19]. Moreover, Fano factor and correlation both depend on variance, which is not statistically different with ortho and retro (but see Fig C.1D and C.1E for completeness).

2.3.1 OB network model captures data trends

To better understand how differences in MC spiking with ortho and retro stimulation come about, we developed a single-compartment OB network model based on Li & Cleland's multi-compartment model [35, 36]. Our model is more computationally efficient than their larger multi-compartment models [35, 36], requiring a fraction of the variables (tens of state variables instead of thousands). Importantly, our single-compartment model retains important biophysical features (Fig 2.2A).

In Fig 2.2A, we see in both models of MC (uncoupled) that the time to spiking decreases

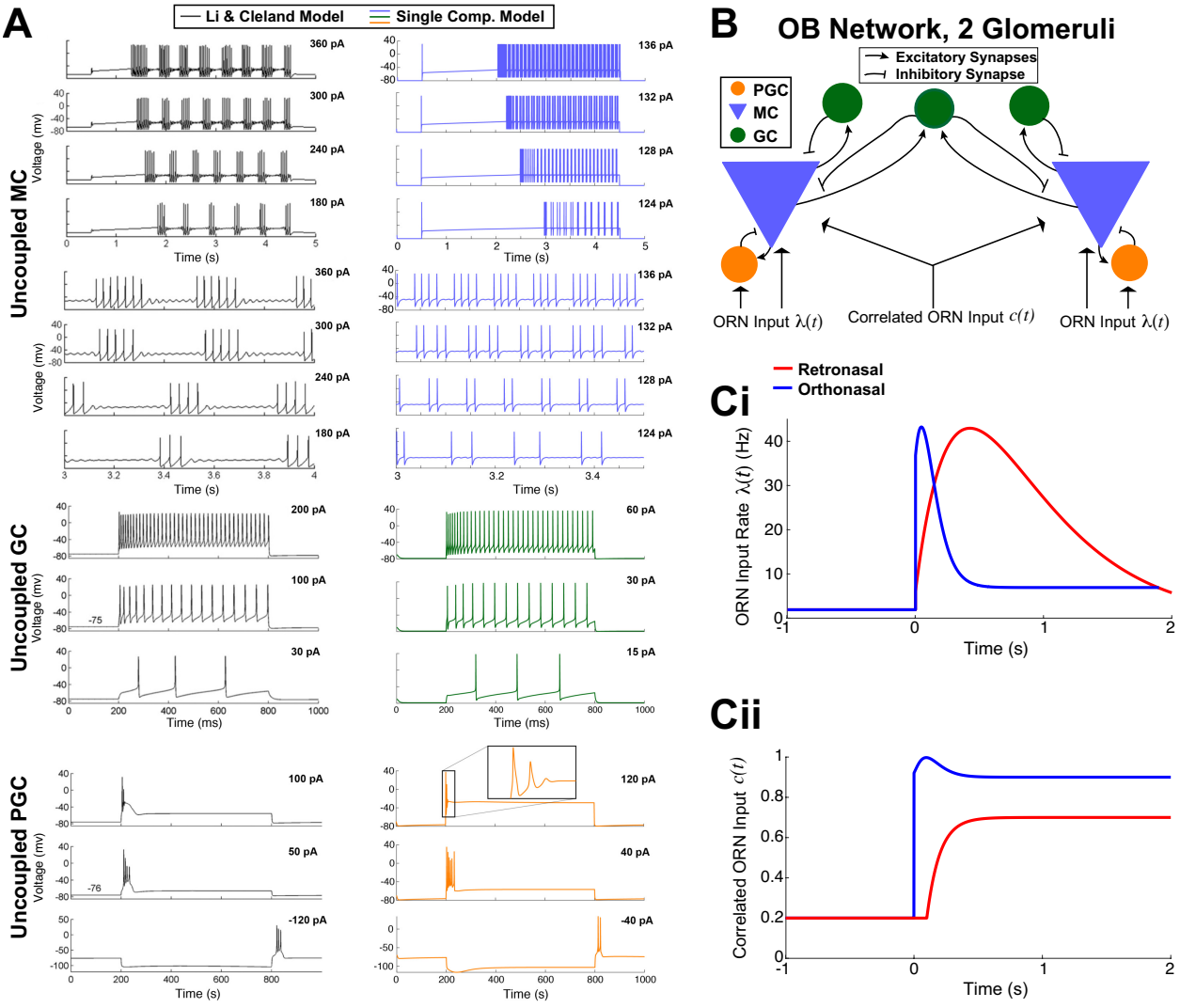

Fig. 2.2.: Biophysical OB model.

A) Dynamics of the 3 uncoupled cell models. MC voltage dynamics with current step inputs in Li & Cleland models (black curves on the left, copied from Li & Cleland [35]) are captured by our single-compartment model (blue on the right). Rows 5–8 show expanded time view of first 4 rows to highlight spike cluster sizes and sub-threshold oscillations (same voltage axis for each). GC voltage responses to three different levels of current injection in the Li & Cleland model (black curves on the left) is similar to our model (green on the right). PGC responses with depolarizing current steps again are similar in both models. Note that release from a hyperpolarizing current injection leads to transient spiking in both models (bottom). B) Coupled OB network model of 2 glomeruli with ORN inputs. ORN synapses are driven by correlated inhomogeneous Poisson Processes (Eqs (2.5)–(2.7)). **C)** Based on ORN imaging studies, we set $\lambda_O(t)$ to increase and decay faster than $\lambda_R(t)$ with odor onset at time 0 s (i). Similarly, we set the input correlation of ORN synapses to the 2 MCs to $c_{R/O}(t)$ where $c_R(t) < c_O(t)$ and $c_O(t)$ rises quicker than $c_R(t)$ (ii).

with increasing current values, and the number of spikes in a cluster increases with current values consistent with prior electrophysiological experiments [47, 48, 49]. The spacing between spike clusters and number of spikes in a cluster in our model (right) qualitatively match the Li & Cleland model (left). The sub-threshold oscillations are not as prominent as in Li & Cleland, but still apparent. In the uncoupled GC models, both ours and Li & Cleland's models exhibit a delay to the first spike with weak current step [50] (Fig 2.2A, bottom) and tonic firing without appreciable delay for higher current injections [51] (Fig 2.2A, middle and top). In the uncoupled PGC models, we do not observe repetitive firing in either models (Fig 2.2A, top and middle). Also, releasing from a hyperpolarizing current injection (bottom) can illicit spiking in both models, as observed by McQuiston & Katz [52]. Thus, we have a condensed OB model by using far less equations than Cleland's models while retaining many of the biophysical dynamics known to exist in these 3 important OB cell types.

Since our focus is on first and second order population-averaged spiking statistics, we use a minimal OB network model with 2 glomeruli (Fig. 2.2B). Each glomerulus has a PGC, MC and GC; we also include a common GC that provides shared inhibition to both MCs because GCs are known to span multiple glomeruli and shape MC spike correlation [33, 53, 54]. Within the OB network, the PGC and GC cells provide presynaptic $GABA_A$ inhibition to the MCs they are coupled to, while MC provide both AMPA and NMDA excitation to PGC and GCs (see Appendix B for further details). The ORN synaptic inputs are an important component of this coupled OB network; they are driven by correlated inhomogeneous Poisson Process with increases in rate and correlation at odor onset. The specific time-varying input rate and correlation we use are shown in Figs. 2.2Ci and Cii, respectively. The differences in ortho versus retro (Fig. 2.2Ci and Cii) are based on prior studies of ORN input to the OB in response to both ortho and retro stimulation [24, 6]. We fixed all model components and manually varied the ORN input rate $\lambda_{O/R}(t)$, see Subsection

2.2.2 for further details.

A comparison of first and second-order statistics between our OB model and *in vivo* data is shown in Fig 2.3. With the ORN activity specified in Fig 2.2C, our OB model is able to qualitatively capture trends seen in our data for firing rate and spike count covariance. Firing rates in Fig 2.3A show that both the model and data exhibit larger firing rates for ortho at odor onset followed by a sharper decline. After the initial increase in ortho firing rates, retro firing rates continue to increase, eventually becoming larger than ortho and remaining elevated longer, consistent with optical imaging experiments (see [24] their Fig 2). Although there is no significant difference in the spike count variance between ortho and retro in our experimental data, we show our data with model for completeness (Fig 2.3B).

Our OB model captures the trend that ortho spike count covariance is larger than retro after odor onset, Fig 2.3C (left). The OB model certainly does not capture the magnitude of the spike count covariance in the data; recall that covariance in our experimental data is the population average over all 1435 simultaneously recorded pairs with significant heterogeneity while our model is homogeneous. But the relative differences between retro and ortho (as measured by the ratio of retro to ortho covariance in the evoked state) are similar (Fig 2.3C, right). Thus our OB model captures the salient trends of the population-averaged spike count statistics. We also show comparisons of Fano Factor (Fig 2.3D) and Pearson's correlation (Fig 2.3E) for completeness. Consistent with our data, our OB model has larger Fano Factor and spike count correlation for ortho than with retro. In the evoked state, the OB model matches spike count correlation for both ortho and retro well. The larger ortho Fano factor in our data is captured in our model, but the difference is very modest.

2.3.2 How OB network transfers ORN input statistics

We next sought to better understand how our OB network model operates with different ORN inputs. In particular, we investigated whether the same OB network model transfers

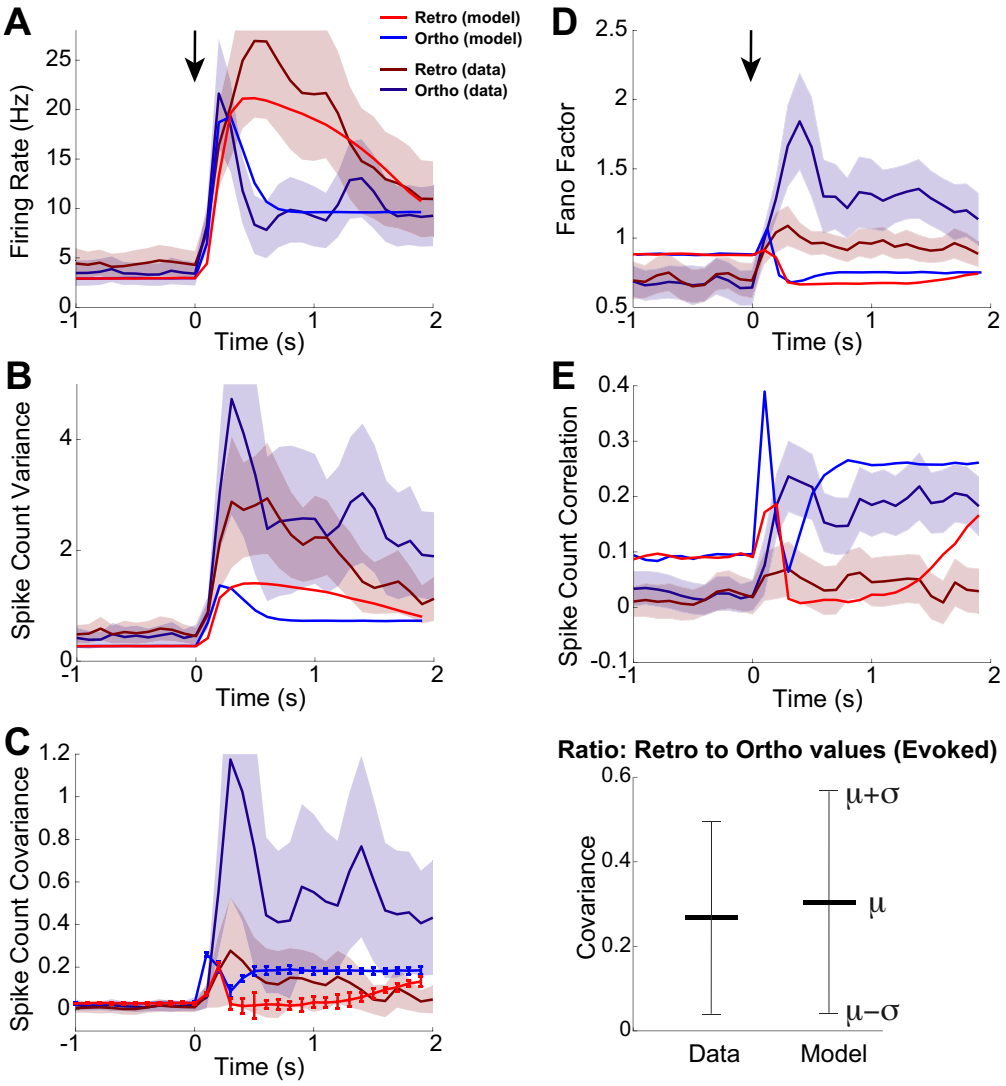

Fig. 2.3.: OB model captures trends in our data.

Comparison of all first and second-order statistics of coupled OB network model to our data. A) Firing rate of ortho increases and decays faster than retro in both data and model. B) Variance of spike counts for ortho and retro shown for completeness, but recall that in experimental data that they are not statistically different. C) Covariance of spike counts is larger for ortho than retro in both data and model (left), but the magnitudes of data and model differ. Comparison of the ratio of retro covariance to ortho covariance in the evoked state (right) shows that the model captures the relative differences between ortho and retro – here μ (resp. σ) is the average (resp. standard deviation) ratio over 20 time bins in the evoked state. For A–C, top shaded error regions of data (retro in A, ortho in B,C) are cut-off to better compare model and data. Comparisons of the (D) Fano factor and (E) Pearson's spike count correlation shown for completeness despite both measures depending on spike count variance. D) The model has slightly larger Fano factor with ortho, consistent with the data. E) The model does qualitatively capture the spike count correlation for both ortho and retro, at least in the evoked state.

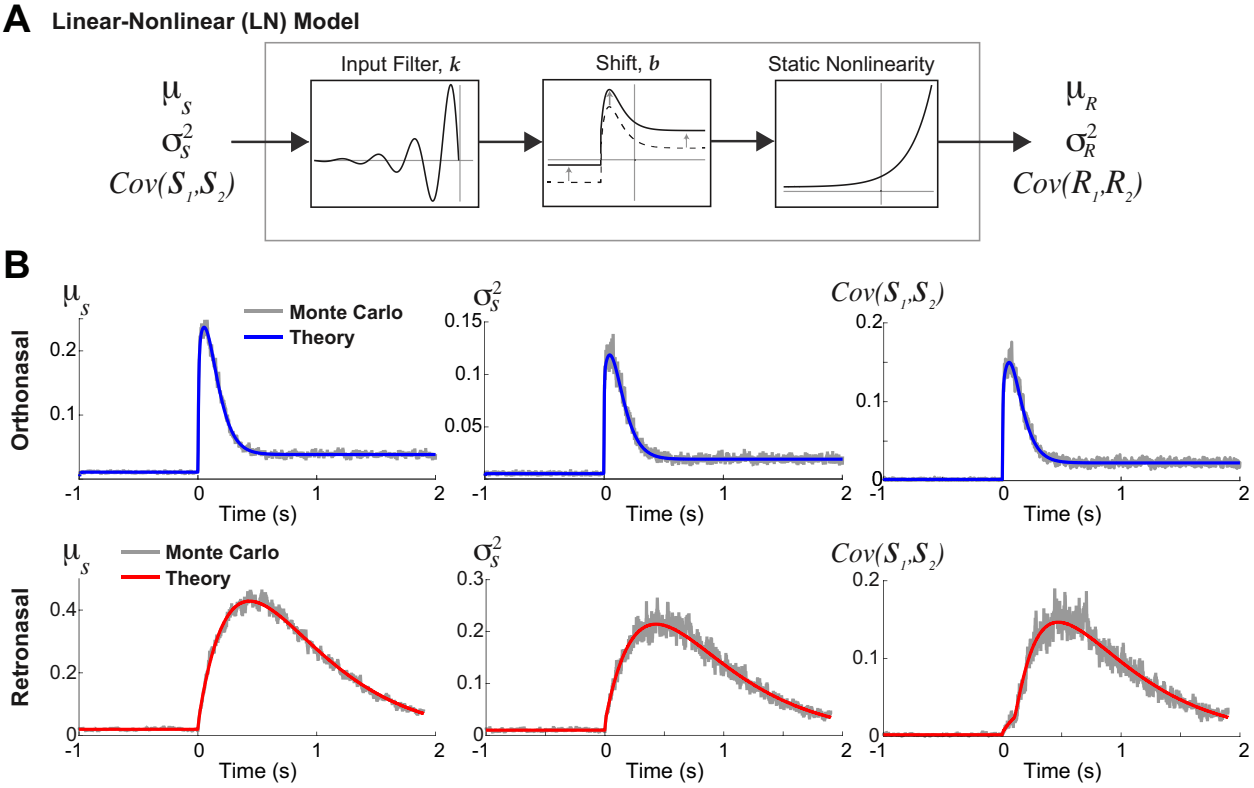

Fig. 2.4.: LN framework used to analyze OB transfer of input statistics.

A) Schematic of the phenomenological linear-nonlinear (LN) model to approximate how the OB network transfers input statistics. B) The actual ortho (top row) and retro (bottom row) input synapses used in the biophysical OB model results in Fig 2.3. Comparisons of the Monte Carlo simulations (Eqs (2.6)–(2.7)) and theoretical calculations (Eqs (2.8), (2.13), (2.17) for respective columns) show smooth curve matches even for correlated time-varying (inhomogeneous) Poisson processes.

ortho and retro ORN inputs to MC spike outputs differently or not. We addressed this in a simple and transparent manner with a phenomenological LN model (Fig 2.4A) to approximate the overall effects of the OB network on ORN inputs. LN-type models have often been used to circumvent the complexities in biophysical spiking models (see [40, 41, 42] and Subsection 2.4 Discussion).

2.3.2.1 Description of the LN model

The LN model first applies a linear filter to the input, $X(t)$, i.e., a convolution with a fixed temporal linear filter k, shifts the result by b, followed by a static non-linearity (exponential function) to produce an output $Y(t)$, see Fig 2.4A:

$$Y(t) = \exp\left(\int_{-\infty}^{t} k(\tau - t)X(\tau)d\tau + b\right) \tag{2.24}$$

For our purposes, $X(t) \in \{\mu_S(t),\ \sigma_S^2(t),\ \mathrm{Cov}\left(S_1(t), S_2(t)\right)\}$ are the statistics of ORN input synapses to the MCs, and $Y(t)$ is an approximation to the statistics of MC spiking response: $\{\mathrm{PSTH}(t),\ \sigma_R^2(t),\ \mathrm{Cov}\left(R_1(t), R_2(t)\right)\}$. We calculate $Y(t)$ (Eq (2.24)) by minimizing the L_2-norm of the difference between $Y(t)$ and the simulated MC spike statistic from the biophysical OB model. The LN model is applied separately to each statistic (further details to follow, see Eq (2.26)–(2.28)). For example, for ortho firing rate (Fig 2.5A, top left), $\mathrm{PSTH}(t)$ is the blue curve in Fig 2.5A, top left, the best fit $Y(t)$ is black dotted curve in Fig 2.5A (top left), found via:

$$(k(t), b) = \arg\min_{k(t),b} \|Y(t) - \mathrm{PSTH}(t)\|_{L_2} \tag{2.25}$$

(also see Subsection 2.2.4). This procedure is repeated for each statistic and mode of olfaction:

$$\mu_S(t) \underset{\mathrm{LN}}{\longrightarrow} \mathrm{PSTH}(t) \tag{2.26}$$

$$\sigma_S^2(t) \underset{\mathrm{LN}}{\longrightarrow} \sigma_R^2(t),\ \text{(spike count variance)} \tag{2.27}$$

$$\mathrm{Cov}\left(S_1(t), S_2(t)\right) \underset{\mathrm{LN}}{\longrightarrow} \mathrm{Cov}\left(R_1(t), R_2(t)\right),\ \text{(spike count covariance)} \tag{2.28}$$

That is, we consider different, separate LN models for each statistic, without any mixing effects (e.g., $\sigma_S^2(t)$ does not directly affect $\mathrm{PSTH}(t)$). Although output statistics generally depend on all input statistics [55, 56, 57], we emphasize that our ad-hoc approach here is meant to better understand how the OB model operates *on each statistic* and is not a

principled alternative model.

By construction, in the biophysical OB model, both the inputs to each MC and the spike output of each MC have identical marginal statistics, so we are using the LN model to assess how univariate input statistics (mean/var) are mapped to univariate output statistics (mean/var). The covariances depend on 2 variables (bivariate: (S_1, S_2) for input and (R_1, R_2) for output), but the LN model is only for assessing how covariance of inputs maps to covariance of outputs without directly modeling multiple random variables.

For the inputs to the LN model, we use an exact theoretical calculation for $\mu_S(t)$, $\sigma_S^2(t)$, $\mathrm{Cov}\left(S_1(t), S_2(t)\right)$ rather than relying on Monte Carlo simulations. The ORN input synapses are driven by correlated time-varying inhomogenous Poisson processes yet we are still able to calculate the first and second order statistics of the ORN inputs in the limit of infinite number of realizations; detailed in 2.2 Calculating time-varying ORN input synapses, Eqs (2.8), (2.13), (2.17). A comparison of Monte Carlo simulations of the actual ORN inputs used in our OB model results (Eqs (2.6)–(2.7)) to the theoretical calculation (Eqs (2.8), (2.13), (2.17)) is shown in Fig 2.4B. We clearly see that the calculations (labeled 'Theory') matches all three ORN input statistics with smooth curves, properly accounting for both time-varying ORN input and time-varying input correlation. These calculations do not depend on any asymptotic assumptions; see Fig C.4 for more examples.

2.3.2.2 Applying LN models to biophysical OB model results

The LN model is able to fit well to the biophysical OB model output MC spike statistics for both ortho and retro stimuli, shown in Fig 2.5A. For this reason, we can assume that the LN model provides a decent approximation of how the biophysical OB model transfers the different ORN input statistics. Thus, the resulting linear filters, $k(t)$ in Fig 2.5B, succinctly show how the various ORN input statistics are convolved in time by the biophysical OB network model. For all 3 spike statistics, retro input statistics result in filters with larger

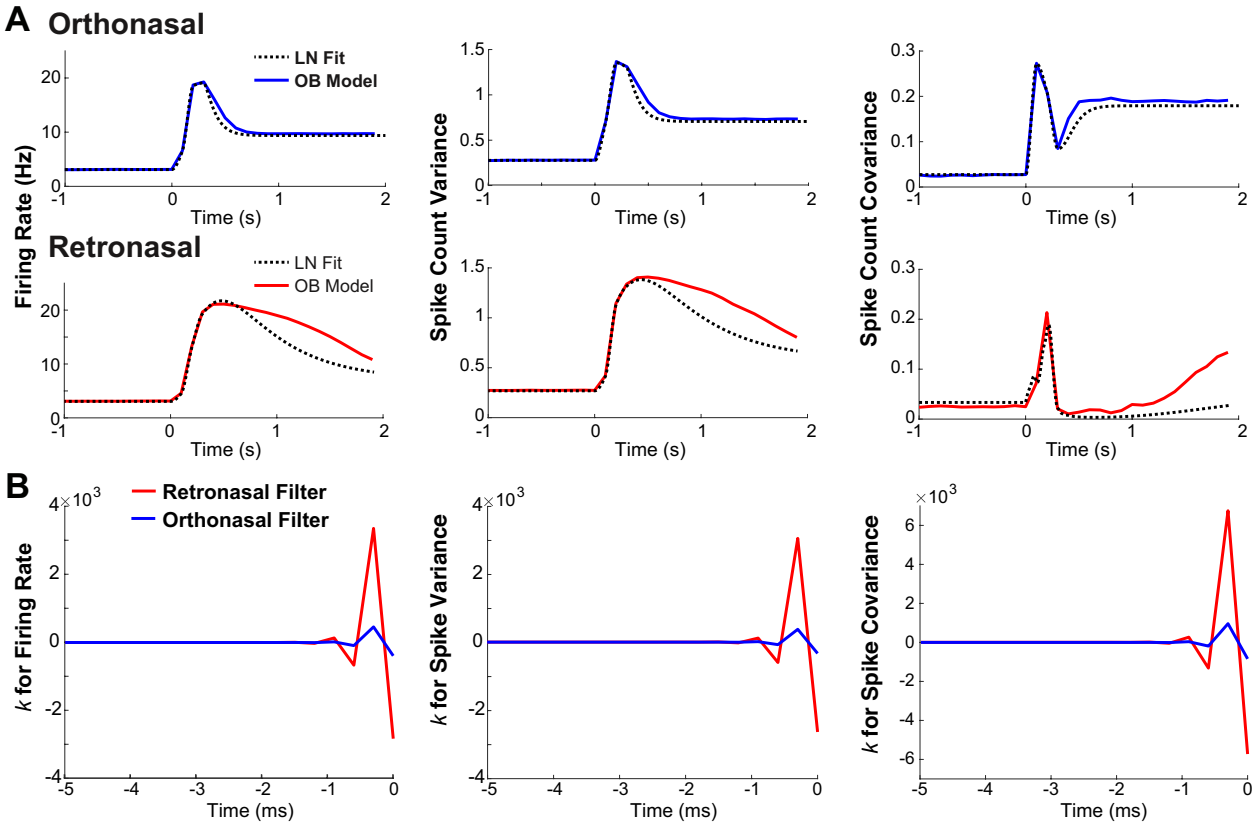

Fig. 2.5.: LN model shows that retronasal input results in linear filters with larger magnitudes.

A) Comparison of LN model output (dashed black curves) to OB network model output statistics for ortho (solid blue curves in top panels) and retro (solid red curves in bottom panels) stimulus with onset at $t = 0\,\mathrm{s}$. The LN output qualitatively captures OB model output statistics. B) Linear filters $k(t)$ in LN model for ortho (in blue) and retro (in red) stimulus over time ($-5 \leq t \leq 0\,\mathrm{ms}$). Linear filters for retro have larger positive and negative values than with ortho.

Table 1.: Shift parameter b for LN model values of fit to MC spiking statistics in Fig 2.5.

The parameter b for the LN model fits (Eq (2.24)) between orthonasal and retronasal are similar for a given statistic, except for spike count covariance.

	PSTH	Variance	Covariance
Orthonasal	2.10	-0.50	-1.56
Retronasal	1.94	-0.55	-3.02

absolute values (both positive and negative) than ortho, suggesting that the OB network operates in a regime where MC responses are more sensitive to fluctuations with retro input. The resulting b values are listed in Table 1; they represent an absolute shift independent of the temporal dynamics. The b values are similar for ortho and retro for all statistics except spike count covariance. Although b is important for the resulting LN curves (dot-black in Fig 2.5A), it is not a part of the temporal processing of ORN inputs.

2.3.3 ORN input signatures for ortho/retro

Despite retro eliciting larger firing rates than ortho, the spike count covariance (as well as correlation and Fano factor) with retro stimulation is smaller than with ortho. It has long been known theoretically and experimentally that in uncoupled cells, the spike correlation increases with firing rate (at least with moderate to larger window sizes) [58], in contrast with our data. In coupled networks, the change in correlation with firing rate is complicated and depends on numerous factors [28, 29, 30, 31]. Thus, the components of ORN inputs that result in these differences (higher firing and less covariance for retro than with ortho) in the same OB network are not obvious.

So we use our computational framework to uncover the important feature(s) of ORN input that: i) results in MC spike statistics consistent with our salient data trends, and ii) linearly filters ORN inputs with larger values with retro than with ortho input. Here we disregard the biological differences in ortho and retro ORN inputs to consider 3 core

attributes of ORN inputs that influence how the biophysical OB model operates:

- Temporal (faster increase and decay, or slower increase and decay; see Fig 2.6A, left)
- Amplitude (low or high, see Fig 2.6A, left)
- Input correlation (lower or higher, black and gray curves respectively, in Fig 2.6A, right)

We consider a total of 8 different ORN input profiles consisting of various combinations of amplitude, input correlation, temporal profiles. The LN model fit to the OB model (i.e., MC spike statistics) for these 8 different ORN input profiles are all similar, well approximating how the OB coupled network transfers input statistics (see Fig 2.5A and Fig C.5). Fig 2.6B clearly shows that the slower increase and decay in input rate (redish/lighter) consistently results in linear filters $k(t)$ with larger absolute values than with faster increase/decay (bluish/darker). The larger filter values holds with all 3 statistics, and with all variations of amplitude and input correlation. Thus, the OB network consistently has filters with larger absolute values when the input profile is slower (i.e., retronasal-like). The resulting LN model b values are listed in Table 2 for reference, although these values represent an absolute scaling independent of the temporal dynamics.

Fig 2.7 shows all 8 OB model results for each spike statistic. For all first and second order statistics, including scaled measures of variability, the most distinct attribute that distinguishes our model results is the temporal profile of input. Importantly, the temporal profile is the key attribute to best capture the differences in ortho and retro our experimental data (see Fig. 2.3). The slow increase and decay in input rate consistently results in retro-like spiking trends while the fast increase and decay in input rate results in ortho-like spiking trends. Thus, our models show that the temporal profile is a signature of retro and ortho stimulation, and emphasizes the critical role of ORN inputs for shaping how the same OB network modulates ortho and retro stimuli.

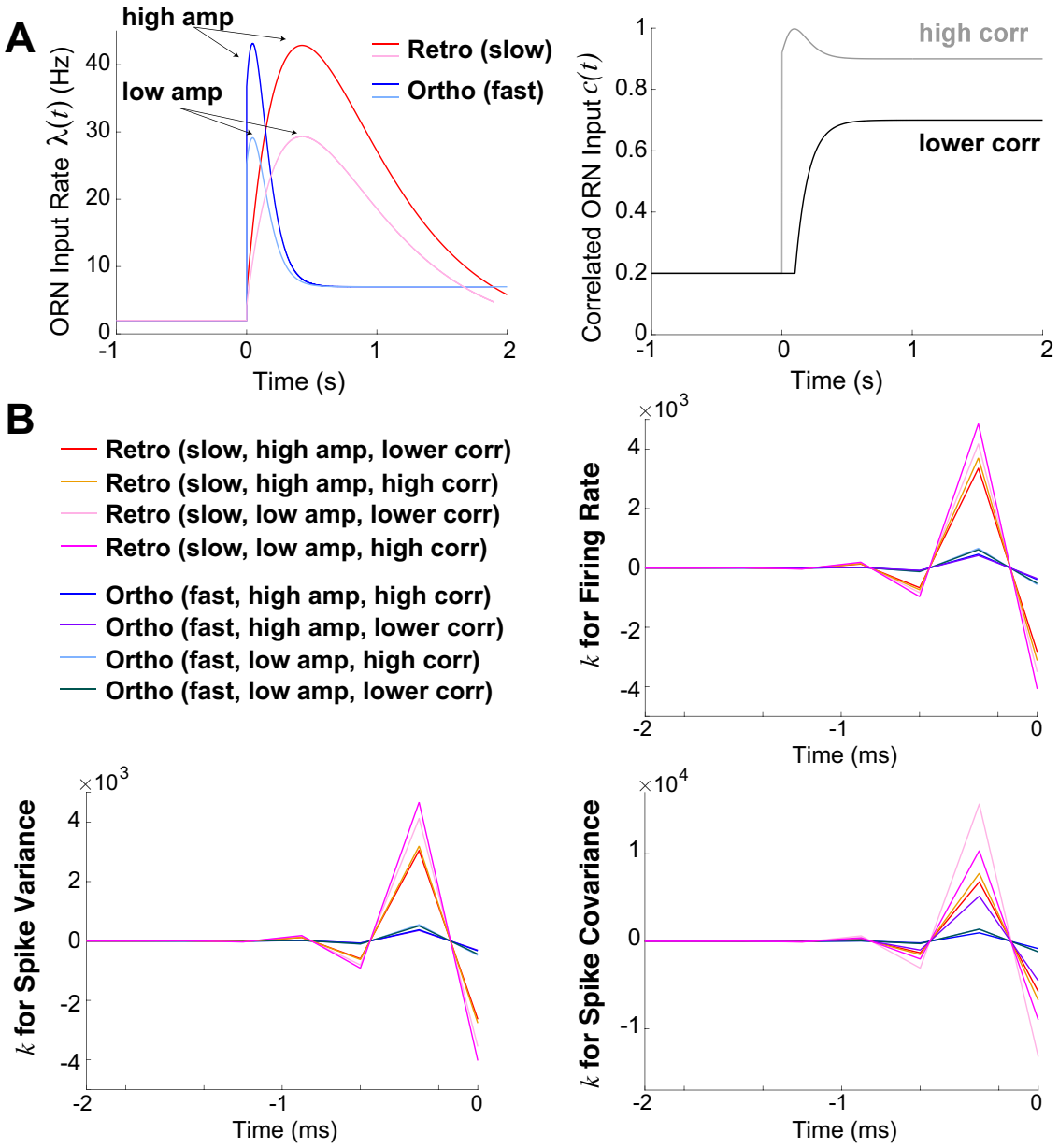

Fig. 2.6.: Comparison of ortho versus retro-like ORN input with different amplitudes and their resulting OB model output statistic linear filters, $k(t)$, from the LN model.

Temporal profile is crucial for larger magnitude filters. A) Different combinations of input rates (left) including slower increase and decay (retro-like) and faster increase and decay (ortho-like) as well as high and low amplitude as labelled. Two different input correlations (right), with high correlation in gray, and lower correlation in black. B) Resulting linear filters $k(t)$ have consistently larger absolute values when temporal profile of ORN inputs is slower (retro-like), compared to faster (ortho-like).

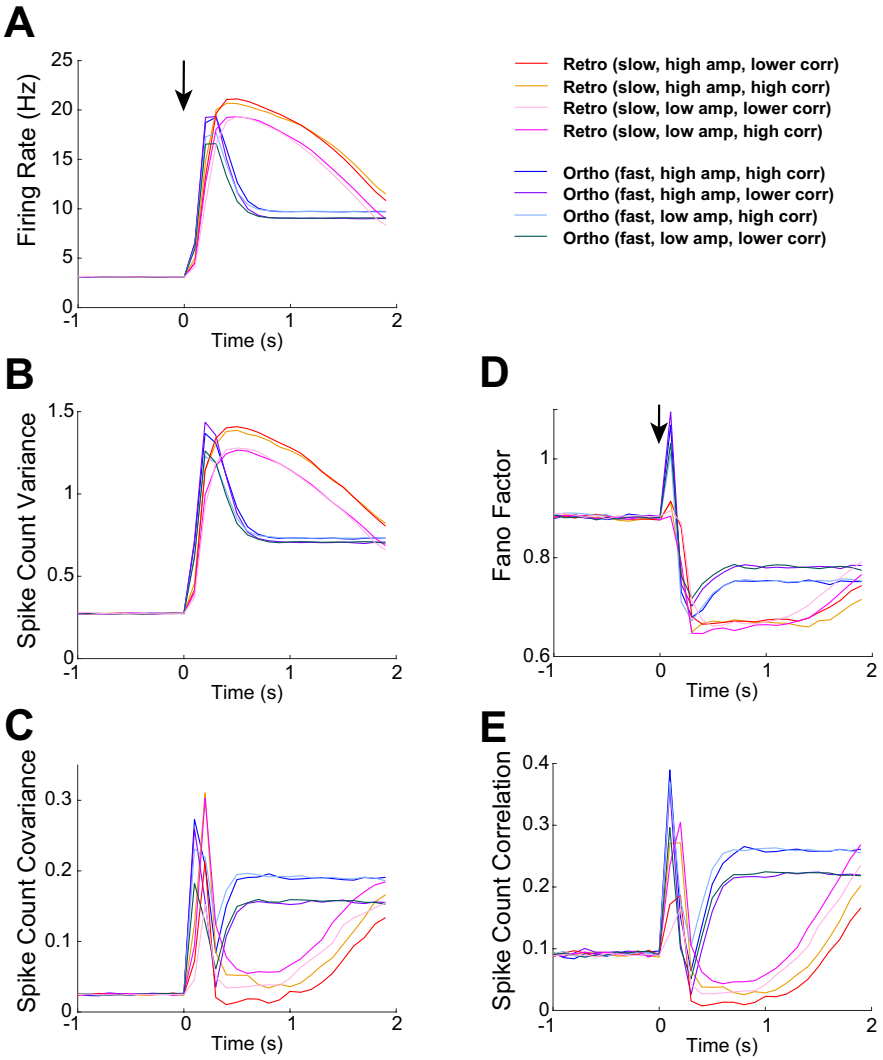

Fig. 2.7.: Comparison of all 8 OB model results given different input attributes.

The 8 different OB model results are from varying temporal profile, amplitude height, and input correlation (2 ways each, see Fig 2.6A). Different temporal profiles is key for both having different model spike statistics **and** for best matching qualitative differences in our data (see Fig. 2.3). A) Firing rate in Hz (left) is slightly lower with low input rate amplitude, but no significant difference with different input correlations. B) Spike count variance, similar to firing rate, has only slightly lower values with low input rate amplitude. C) Spike count covariance is lower with lower input correlation for all of ortho evoked state (not surprisingly). However, retro (fast) with lower amplitude steadily increases above higher amplitude after about 1 s in the evoked state. D) Fano Factor model results only change modestly. E) Pearson's spike count correlation, similar to spike count covariance, is lower with lower input correlation and similarly for retro (fast), there is an increase with higher input correlation.

Table 2.: Shift parameter b for LN model values of fit to MC spiking statistics in Fig 2.6.

The parameter b for the LN model fits (Eq (2.24)) of the various parameters for temporal profile, amplitude, and input correlation. Amplitude and ORN input correlation profiles as defined for Figs 2.3-2.5 and associated values previously listed in Table 1 are noted in bold.

Temporal	Amplitude	ORN correlation	PSTH	Variance	Covariance
Fast (ortho)	**High**	**High**	**2.10**	**-0.50**	**-1.56**
	High	Low	1.99	-0.56	-1.35
	Low	High	2.03	-0.55	-1.62
	Low	Low	1.97	-0.61	-3.42
Slow (retro)	High	High	2.04	-0.50	-1.11
	High	**Low**	**1.94**	**-0.55**	**-3.02**
	Low	High	1.70	-0.72	-1.36
	Low	Low	1.59	-0.81	-3.18

2.4 Discussion

We investigated how odors processed via the orthonasal and retronasal routes result in different OB spike statistics, analyzing in detail how ORN inputs transfer to MC spike outputs. Motivated by our *in vivo* rat recordings that showed significant differences in first and second order spiking statistics of MC, we developed a realistic OB network model to investigate the dynamics of stimulus-evoked spike statistic modulation (higher firing and lower covariance/correlation with retro than with ortho). Our OB model balances biophysical attributes [35, 36] with computational efficiency. The OB model is able to capture salient trends in our data with both ortho and retro stimulation, and should be useful for future studies of OB. We successfully used the biophysical OB model, paired with a phenomenological LN model, to analyze how different ORN inputs lead to different dynamic transfer of input statistics. We also showed that the temporal profile of ORN inputs is a key determi-

nant of ortho versus retro input via model matching our data. The output spike statistics are crucial because the OB relays odor information to higher cortical regions, and thus our work may have implications for odor processing with different modes of olfaction [2, 18, 6].

To the best of our knowledge, our experiments detail the differences in MC spiking with ortho and retro stimuli for the first time. However, the work of Scott et al. [26] is related; they used 4 electrodes to record OB spiking activity in the superficial layers of OB in rats. Their results are difficult to directly compare to ours as they focus on superficial OB in the epithelium rather than the mitral cell layer, but at least the trial-averaged firing rates in their data appear to be consistent with our data. Moreover, our multi-electrode array recordings enable us to consider trial-to-trial covariance of spiking.

The key attribute(s) of ORN inputs that can result in different ortho and retro MC spike statistics consistent with our data are not obvious. Indeed, retro stimulation resulted in larger firing rates than ortho, and the spike count covariance (as well as correlation and Fano factor) with retro stimulation is smaller than with ortho, in contrast to uncoupled cells where correlation increases with firing rate [58]. Using various models, we were able to consider how three components of ORN inputs (temporal profile, amplitude, and input correlation) result in different OB dynamics with regards to transferring input statistics to outputs. Prior experiments [23, 24, 6] have shown these input components can differ with ortho and retro inputs. We found that the temporal profile (fast versus slow) plays a critical role for both capturing our data and for shaping the transfer of inputs to outputs, i.e., retro inputs consistently resulted in larger temporal filter values, so the OB network is more sensitive to fluctuations of retro input statistics than ortho. To capture the salient trends in our data, we find slower input rate (rise and decay) is a key signature of retronasal stimulation, while faster rise and decay [24, 6, 26] is similarly a key signature of orthonasal stimulus.

The temporal differences between ortho versus retro have previously been thought to

play a role in distinguishing ortho/retro stimulation at the ORN [23, 6, 24, 26, 27], but whether this carried over to the OB and if this held at the level of spiking was unknown. Here we demonstrate the importance of different temporal input to OB for ortho versus retro.

We used an ad-hoc LN model framework because many of biological complexities are removed yet important features are retained. That is, neurons are known to linearly filter inputs, and spike generation is inherently nonlinear, i.e., finding linear filters of neurons is not new [42], and they are related to the spike-triggered average [59]. Thus, LN-type models have been used in many contexts, often to circumvent biophysical modeling, and most notably with generalized linear models [60, 61] (also see [41]) where various filters (stimulus, post-spike) and model components are fit to data using maximum likelihood. Connecting the large gap between biophysical models and LN models is daunting, but see Ostojic and Brunel [40] who relate stochastic integrate-and-fire type models to LN. Our approach here is much simpler than the aforementioned works because we simply wanted to assess how a particular statistic (mean, variance or covariance) mapped via the OB network model in a simple and transparent manner. An enhanced data-driven approach to fitting an LN-type model that relies on experimental data of *both* ORN inputs and MC spike outputs with many trials might better reveal differences in how the OB operates with ortho versus retro. However, we currently do not know if such a dataset exists.

Here we list some limitations of our study. We only considered the MC response to a single food odor despite a large variety of food (and non-food) odors animals encounter. Different odors activate different olfactory receptors that could lead to qualitatively different population MC spiking activity than what we report here. Retronasal odors are predominately food odors, and studies have shown that humans can more accurately detect food odors (vs. non-food odors) delivered retronasally [18]. Frasnelli et al. [62] showed that food versus non-food odors illicit varying neural responses in humans when introduced ortho-

versus retronasally. An fMRI BOLD study showed that cortical activity in humans differed when odors were introduced via the ortho or retro routes, specifically with food odors [2]. Thus our choice of a food odor is a natural first step for investigating retronasal MC responses. Also, we attributed the differences in ortho/retro MC responses solely to ORN inputs when in fact many regions synapse to OB [63]. For example, optogenetic studies [64, 65] have shown that feedback from olfactory cortex to OB is relatively strong and inhibition dominated. Whether this cortical feedback (or other external modulation) differs for ortho and retro stimulation is currently unknown. Moreover, odor-specific cortical feedback to OB [66] could alter the OB spike correlation, a factor that our modeling study did not account for. Finally, our data is from anaesthetized rats that enabled control of odor delivery and excluded confounding factors such as the breath cycle and sniff rate [67, 68]. However, the MC spike activity in awake rodents can be quite different than in anesthetized [69], so whether our reported differences in ortho versus retro MC spiking hold in awake rodents is an open question. We hope our work here inspires more research into the differences between ortho versus retro olfaction, in particular in downstream olfactory circuits and with other experimental preparations.

With a combination of experiments and different scales of neural network modeling, we provide a basis for understanding how differences in OB spiking statistics arise with these 2 natural modes of olfaction. More generally, our model framework provides a road map for how to analyze attributes responsible for different OB spiking when driven by differences in ORN inputs.

CHAPTER 3

THE EFFECTS OF BACKGROUND NOISE ON A BIOPHYSICAL MODEL OF OLFACTORY BULB MITRAL CELLS

3.1 Introduction

This work is a published article in the Bulletin of Mathematical Biology (BMB) journal [70].

The spiking statistics and dynamics of neural models are crucial in theoretical investigations for how animals accurately and efficiently code sensory signals. This fact has sparked numerous theoretical tools to quantify spiking behavior [71, 72]. These mathematical tools have led to great advances in our understanding of sensory neural networks, but often require making simplifying assumptions (e.g., low dimensional state variables, stable periodic dynamics, very weak or very strong noise). These limiting assumptions are easily violated when models incorporate biological realism, in which case, non-conventional or systems specific approaches must be used to better understand model behavior.

Mitral cells (**MC**) are excitatory cells in the olfactory bulb that are responsible for relaying odor information to downstream cortical regions. One of the most realistic biophysical olfactory bulb MC models was developed by the Cleland lab [35, 36]. Their high-dimensional multi-compartment model captured known physiology of mammalian MC cells reported in experiments by several labs [47, 48, 49]. The Cleland model is ideal for simulating MC behavior for a single instance of odor stimuli, and accounts for different compartments (i.e., soma, spine, dendrite). Indeed, the olfactory bulb circuit has fast dendrodendritic synaptic coupling [32] that a simple model cannot fully capture. However, large dimensional spatial models are less ideal for noise-driven systems when averaging over realizations is necessary to

assess spike statistics. To this end, we have recently developed a modification of this model, removing spatial aspects and collapsing the model to a single compartment [9]. Like the Cleland models, our model contains 7 ionic currents (sodium, potassium, L-type calcium, delayed rectifier, etc., see Section 3.2 and Appendix B) and 13 total state variables.

In this paper we study the spike statistics of our single-compartment MC model (based on [35, 36]) with background fluctuations. Our model enables efficient yet biophysically complex simulations with which to analyze MC spiking dynamics. Our prior use of this model in [9] centered around addressing how different modes of olfaction (inhale or 'orthonasal' versus exhale or 'retronasal') could manifest different operating regimes of the olfactory bulb network; we applied the model to a specific experimental data set. The general behavior of this MC model has not been investigated in detail. A natural first step is to consider the behavior of our MC model subject to background fluctuations (i.e., white noise) that is often used to mimic network and other random effects. We observe complex spiking even with constant current input, including modulation of multi-modal peaks in the interspike interval distribution **(ISI)**. With modest changes to input fluctuations (noise), the spiking variability can change dramatically even though the firing rates do not change much, exhibiting non-monotonic spike variability not commonly observed in simple spiking neuron models. We explain these dynamics with a phenomenological model of the ISI probability density function. This paper provides insights to some of the complexities of MC spiking dynamics.

3.2 Material and methods

See GitHub page `https://github.com/michellecraft64/MCuncoup` for freely available code simulating the models in this paper.

Our MC model is based on a multi-compartment model developed by the Cleland Lab [35, 36], where all compartments (soma, dendrite, axons, spin) are combined into a single

compartment, as in [9]. All parameters and function for intrinsic ionic currents and their gating variables are the same as in [35, 36] except the maximal conductance, which is set to be the sum of all maximal conductance values from all compartments. Excluding the many auxiliary functions, there are a total of 13 state variables (ODEs).

$$
\begin{aligned}
C_m \frac{dV}{dt} &= I - \frac{1}{R_m}(V - E_{\mathrm{L}}) - \sum_j I_{\mathrm{Ion,\,j}} + \sigma\xi(t), && (3.1)\\
I_{Ion,j} &= g_j m_j^p h_j^q (V - E_j), && (3.2)\\
\frac{dX_j}{dt} &= \alpha_{X_j}(1 - X_j) - \beta_{X_j} X_j && (3.3)\\
\frac{d[\mathrm{Ca}^{2+}]}{dt} &= -I_{\mathrm{CaL}}/(2wF) + \frac{0.05 - [\mathrm{Ca}^{2+}]}{10}. && (3.4)
\end{aligned}
$$

The variable X (Eq (3.3)) generically represents 11 different gating variables for the 7 different ionic currents (see Table 12), and the transition rates α, β can depend on V, $[\mathrm{Ca}^{2+}]$, etc. (see Table 13 for gating variable equations). Note, I_{NaP} current is not represented by Eq (3.3) since it is defined by $m = m_\infty(V)$. The noise level is measured by $\sigma \geq 0$, and $\xi(t)$ is white noise with $\langle \xi(t) \rangle = 0$ and $\langle \xi(t)\xi(t') \rangle = \delta(t - t')$.

3.3 Results

3.3.1 Non-standard spiking dynamics

The MC model we developed captures some real biological features exhibited in experiments. To mimic slice experiment recordings of MC, we start by analyzing the voltage traces of the MC model in response to step current injection (Fig 3.1). For 3 different levels of current injection ($I = 122, 125, 130\,\mu\mathrm{A/cm}^2$), Fig 3.1a clearly shows that the time to sustained spiking decreases as the current value is increased, consistent with slice experiments in [49]. Zoomed-in plots of the voltages (Fig 3.1b) shows clusters of spikes, with the number of spikes increasing with current injection value, again consistent with experiments [49].

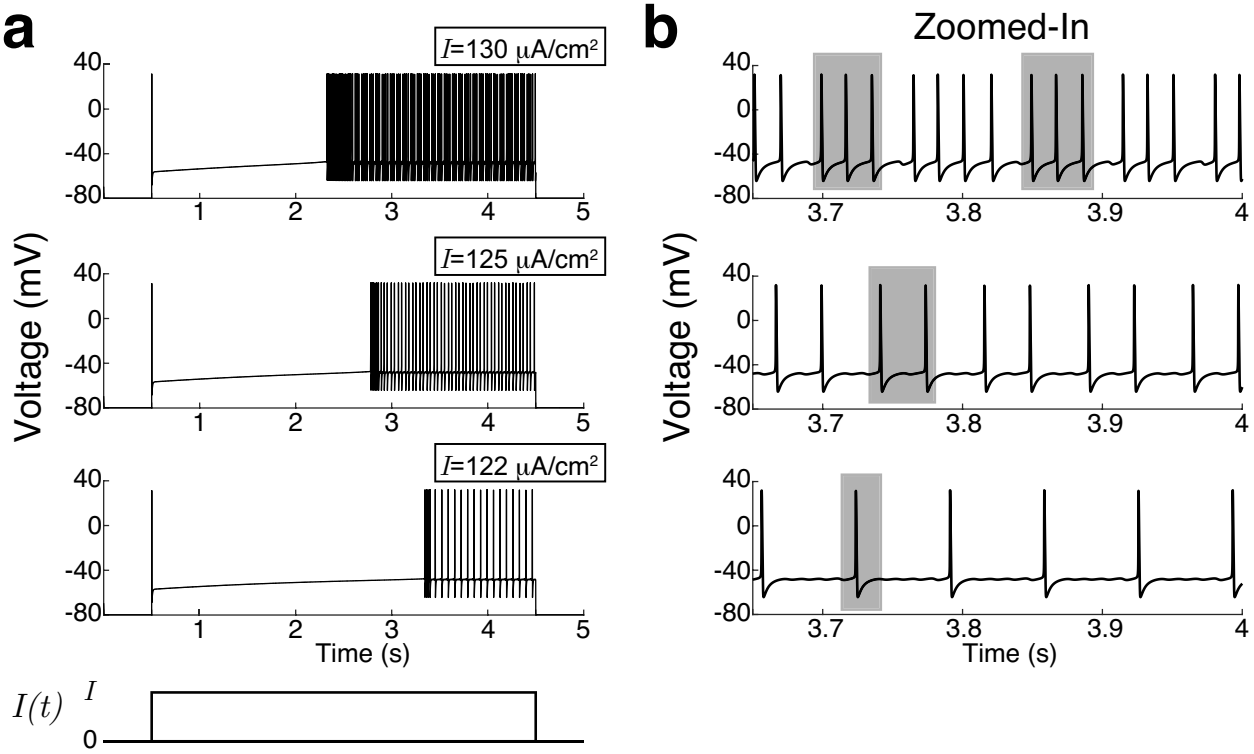

Fig. 3.1.: Single compartment MC model derived from a multi-compartment OB model captures known physiology.

The transient voltage dynamics from a rest state induced by a step increase of current injection to I. a) The voltage traces show a time delay to spiking that increases as the current injection value I decreases, consistent with [47, 48, 49] and multi-compartment model by [35]. b) Zoom-in view of the voltage trajectories shows the number of spikes increases and tends to cluster with current injection value, consistent with experiments reported in [49] and multi-compartment model by [35]. Shaded rectangle highlights the approximate burst size. Sub-threshold oscillations are apparent (also see Fig 3.2a).

Also the time between clusters of spikes decreases with increasing current [48]. Our model also has subthreshold voltage values that increases with current injection value (not shown), which was reported in real MCs [48]. Note that our model only qualitatively captures the physiology; the described effects are more pronounced in [47, 48, 49].

Another hallmark of MC voltage dynamics is sub-threshold oscillations [47, 48], which were not as apparent in Fig 3.1 because of horizontal axis scale, but evident in Fig 3.2a. Fig 3.2a shows ongoing voltage traces (long after the transient dynamics) with fixed current injection values. Notice that the temporal dynamics are complicated, with extended periods

of quiescence (no spiking), rapid spiking, as well as intermittent irregular spiking (all without any background noise $\sigma = 0$). The multiple time-scales are certainly evident, making standard mathematical analysis of the model difficult. These complex dynamics are perhaps not surprising given that the MC model has 13 state variables.

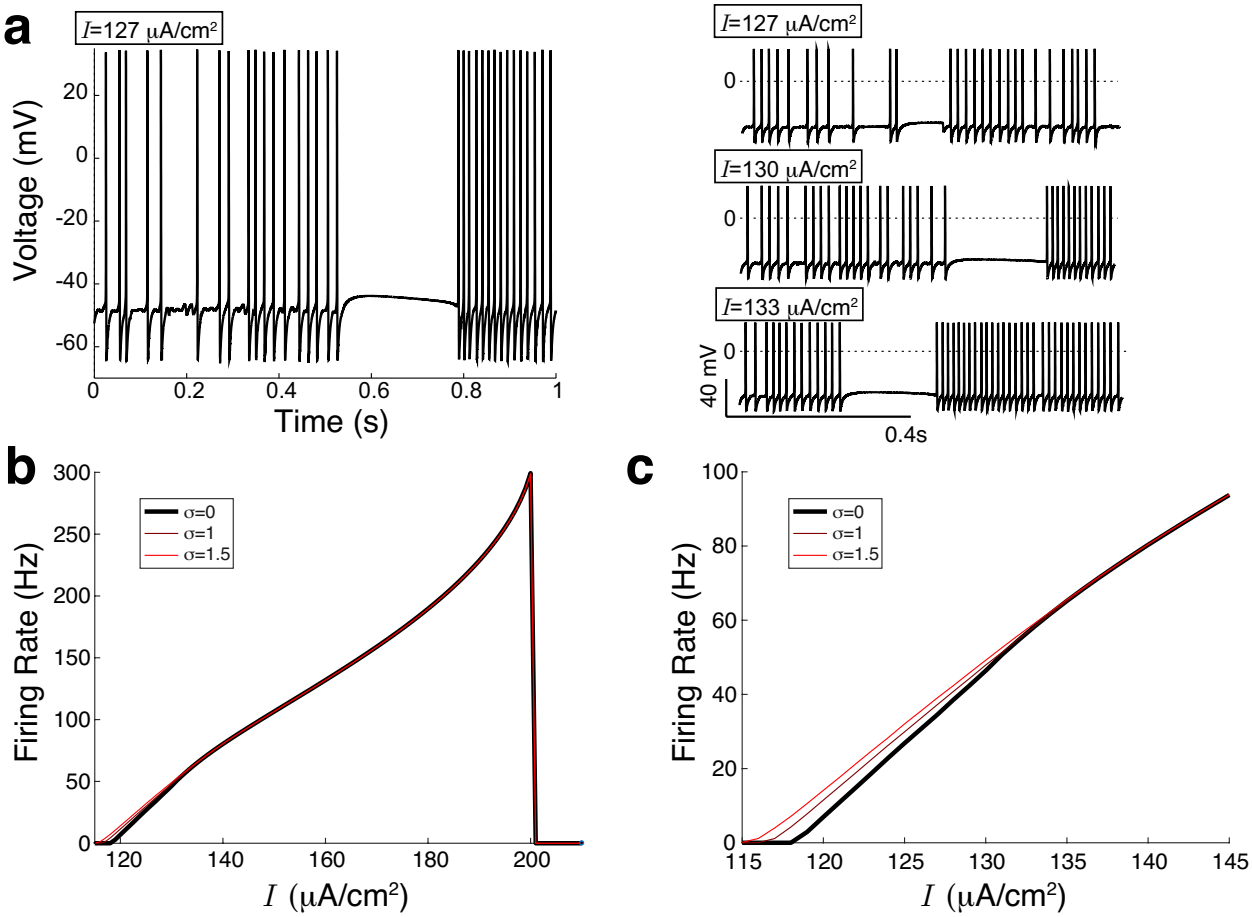

Fig. 3.2.: MC complex spiking behavior is not well-captured by (time-averaged) firing rate. a) Ongoing voltage traces (not transient, *cf.* Fig 3.1) with various current values I and $\sigma = 0$. The spiking behavior has multiple time-scales with periods of quiescence, rapid and intermittent spiking. b) The FI-curve (firing rate as a function of input current) does not change much with these noise values. c) Same as b) but zoomed-in to show the slight increase in firing rate with noise.

We next consider the 'FI-curve' (or transfer function) of the MC model, one of the most common entities to characterize spiking behavior. This is the output firing rate (total number of spikes divided by time) as a function of input current I. We consider both the baseline

case without noise (Fig 3.2b,c in black) and with relatively small noise (brown, red). Noise tends to increase the firing rates except when firing rates are very large [73]. We observe the largest changes in firing rates with increased noise where MC fires very little, consistent with many neuron models [73]. The curves in Fig 3.2b,c demonstrate that noise affects firing rate in a relatively simple manner, like what is observed in simpler low-dimensional spiking models, but firing rate (an average first order statistic) does not account for the aforementioned temporal dynamics in Fig 3.2a.

A natural entity to characterize spike statistics is the distribution of time between consecutive spikes, i.e., the ISI. The ISI has been used in many contexts [74], including classifying firing patterns from experimental data [75]. Multiple peaks are signatures of multiple time-scales of spiking dynamics. Fig 3.3 shows simulations of the ISI densities for 3 fixed current values. As noise increases, it is expected for the ISI densities to shift left as well as widen [74] which is seen for $I \in \{120, 140\}$ in Fig 3.3a & c. However, with $I = 130\,\mu\text{A/cm}^2$, the ISI has two prominent peaks that evolve into only one peak as noise increases (Fig 3.3b). It should be noted that the ISI for $I = 120\,\mu\text{A/cm}^2$ when $\sigma = 0$ also appears to have two peaks, however, these are not as well-separated as the two peaks seen for $I = 130\,\mu\text{A/cm}^2$ when $\sigma \in \{0, 0.5\}$. In these plots, simulating 500,000 spikes is computationally feasible because of our single-compartment model development.

A central focus of this paper is that the firing variability as measured by σ_{ISI} (standard deviation of ISI) and the Coefficient of **V**ariation ($\underline{\mathbf{CV}{:=}\sigma_{ISI}/\mu_{ISI}}$) are non-monotonic functions of input noise σ for realistic odor-induced firing rates (Fig 3.3e,f). For intermediate current values, ($I \in \{128, 129, 130, 131\}\,\mu\text{A/cm}^2$), the firing rates are in the range of what is reported in mammals' MC in OB *in vivo* [67, 76, 77, 37]. We observe as input noise increases, the firing variability initially increases, reaches a maximum, then slowly decreases for these intermediate current values. For $I = 120\,\mu\text{A/cm}^2$, the standard deviation of the ISI σ_{ISI} is also non-monotonic with respect to input noise σ. However, when it is normalized

by the mean via the CV, we see that it ($I = 120$) is simply a monotonically increasing function. Notice that the change in σ_{ISI} is large, over an order of magnitude with the input noise values we used. Lastly for very high firing rates ($I = 140\,\mu\text{A/cm}^2$), the dynamics are straight forward; uni-modal ISI with monotonically increasing spike variability with input noise.

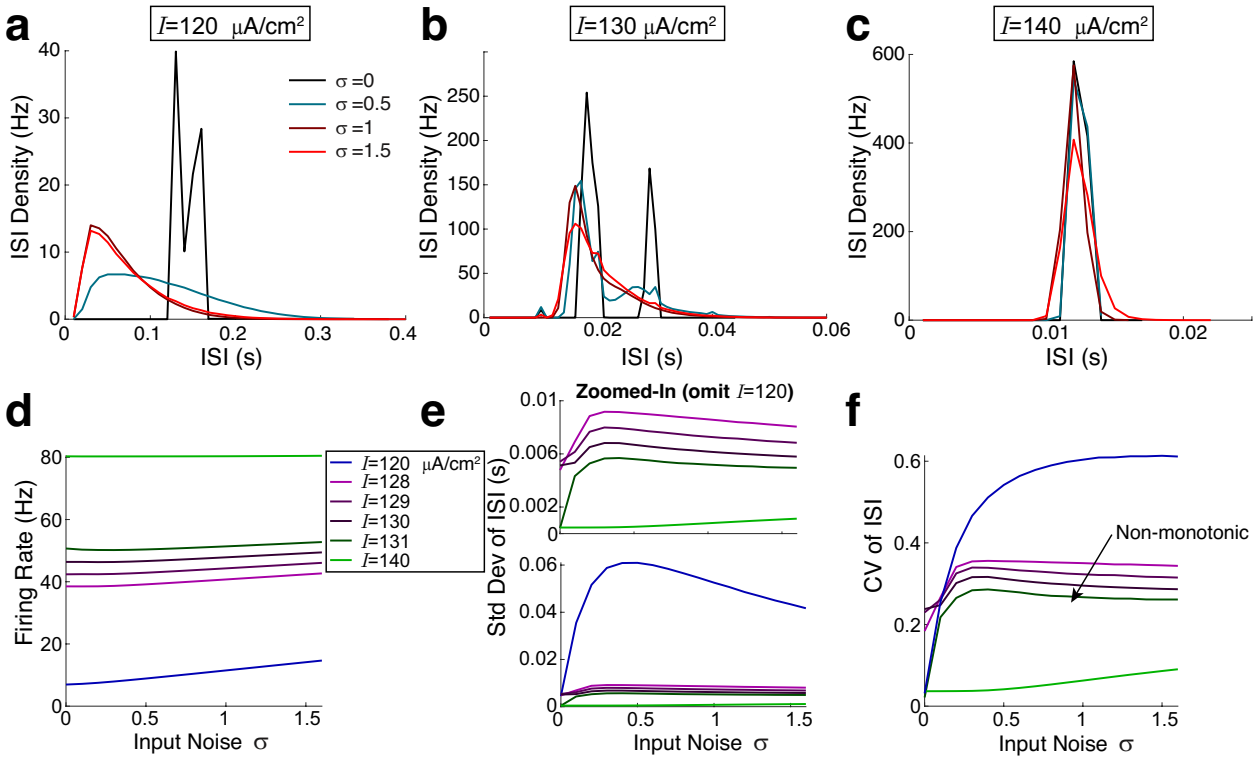

Fig. 3.3.: MC model simulation results show complex spike dynamics for physiological firing rates.

a)–c) The ISI density for fixed input current and different values of input noise: $\sigma = 0, 0.5, 1, 1.5$ using histogram bin widths of 0.01, 0.001, and 0.001 s, respectively. a) ($I = 120\,\mu\text{A/cm}^2$) and c) ($I = 140\,\mu\text{A/cm}^2$) show expected changes with noise: the distribution shifts to the left and widens, respectively, as $\sigma \nearrow$ [74]. b) However, with $I = 130\,\mu\text{A/cm}^2$, the ISI has 2 prominent peaks that eventually merges to 1 peak as noise increases. The ISI in a) for $\sigma = 0$ has peaks, but they are not as well-separated. d)–f) Summary ISI statistics for more σ values. d) The firing rate (inverse of mean ISI) unsurprisingly increases with noise for all I (although modest for $I = 140$). e) Std. dev. of ISI is a non-monotonic function of input noise σ except for large current: $I = 140$. f) The CV of ISI (std. dev. over mean) is a non-monotonic function of input noise σ for intermediate current values ($I \in \{128, 129, 130, 131\}$), coinciding with physiological firing rates.

Even with weak to modest background noise values, the multi-modal peaks in ISI density can disappear (e.g., with $I = 130\,\mu\text{A/cm}^2$ in Fig 3.3b). It is thus notable that MC bursting activity with multiple time-scales (as reported in slice recordings [49]) may not be operable in a network when background noise fluctuations are prominent. We do not explore the theoretical shapes of the ISIs, which may certainly have more or less modes than what is shown in Fig 3.3a,b,c, (a bin size was set; other bin-sizes will naturally give different shapes).

Standard neural spiking models like the leaky integrate-and-fire model do not exhibit non-monotonic spiking behavior as a function of (uncorrelated) input noise [72]. Even when the synaptic input events have temporal correlation and the spiking variability can go down with increasing input noise (see Fig 5A of [78]), the relationship is often monotonic – a notable exception is when there are a range of time-scales [79].

3.3.2 Capturing results with a phenomenological model

In this section we will describe the prior observations with a simple phenomenological that will enable us to dissect how the structure of the noise and intrinsic time-scales (i.e., multi-modal ISI density) contribute to non-monotonic spiking variability.

In Appendix D.1, we highlight possible avenues for analysis and argue that a more formal mathematical approach to describe the observations in the previous section is likely infeasible, at least in our opinion. Although we have not discounted every possible approach to analyze our MC model, describing these results likely requires a phenomenological approach, especially considering there are 13 state variables with a range of time scales.

We approximate the ISI with the random variable S, governed by the equations:

$$\frac{dS}{dt} = -f_{A/B}(S) + \tilde{\sigma}(S)\xi(t) \tag{3.5}$$

$$f_A(S) = (S - s_1)(S - s_2)(S - s_u), \text{ with } 0 < s_1 < s_u < s_2 \tag{3.6}$$

$$\text{or } f_B(S) = (S - s^*), \text{ with } 0 < s^*. \tag{3.7}$$

With weak noise, f_A results in a multi-modal ISI with 2 peaks (Fig 3.3b), f_B is uni-modal (Fig 3.3c). The advantage here is that the PDF of S

$$\Pr(S(t) \in (s, s+ds)) := \rho(s,t)\, ds$$

can be analytically solved for, in the steady state:

$$0 = \frac{\partial \rho}{\partial t} = -\frac{\partial}{\partial s}\left\{ -f_{A/B}(s)\rho - \frac{1}{2}\frac{\partial}{\partial s}\left\{\tilde{\sigma}^2(s)\rho\right\}\right\} \tag{3.8}$$

The solution is [80, 81]:

$$\rho(s) = \frac{N}{\tilde{\sigma}^2(s)} \exp\left\{ -2\int_0^s \frac{f_{A/B}(s')}{\tilde{\sigma}^2(s')}\, ds' \right\} \tag{3.9}$$

where $N^{-1} = \int_0^\infty \frac{\exp\left\{-2\int_0^s f_{A/B}(s')/\tilde{\sigma}^2(s')\, ds'\right\}}{\tilde{\sigma}^2(s)}\, ds$ is the constant to normalize ρ. When $\tilde{\sigma}$ is constant, the density is simply:

$$\rho_B(s) = \frac{1}{\tilde{\sigma}\sqrt{\pi}} \exp\left\{ -\left(\frac{s-s^*}{\tilde{\sigma}}\right)^2 \right\} \tag{3.10}$$

$$\rho_A(s) = N \exp\left\{ -\frac{F_A(s)}{\tilde{\sigma}^2} \right\} \tag{3.11}$$

where $F_A(s) = s^4 - \frac{4}{3}(s_1+s_2+s_u)s^3 + 2(s_1s_2+s_1s_u+s_2s_u)s^2 - 4(s_1s_2s_u)s$ has local mins at s_1, s_2 (global min is(are) the point(s) furthest from s_u) and a local max at s_u by construction, and $N^{-1} = \int_0^\infty \exp\left(-F_A(s)/\tilde{\sigma}^2\right) ds$ is the constant to normalize ρ. This formulation will thus allow us to assess how the number of peaks and the structure of the *effective* noise alters σ_S and σ_S/μ_S – these are respectively the representations of σ_{ISI} and CV from the biophysical MC model.

For exposition purposes, we set the fixed points to be $s_1 = 4, s_2 = 8, s_u = 6$ for f_A, and $s^* = 6$ for f_B. First consider the case of simple additive noise where $\tilde{\sigma}$ does not depend on S. In the uni-modal case (f_B), it is not surprising that the spiking variability (σ_{ISI}, CV) monotonically increase with $\tilde{\sigma}$ (Fig 3.4c,d) because the PDF (Eq (3.10)) is simply a Gaussian

distribution with $\sigma_S = \tilde{\sigma}/\sqrt{2}$ (Fig 3.4b). For the multi-modal case (f_A), we find that for a large range of $\tilde{\sigma}$, the spiking variability monotonically decreases with noise $\tilde{\sigma}$ (Fig 3.4c,d).

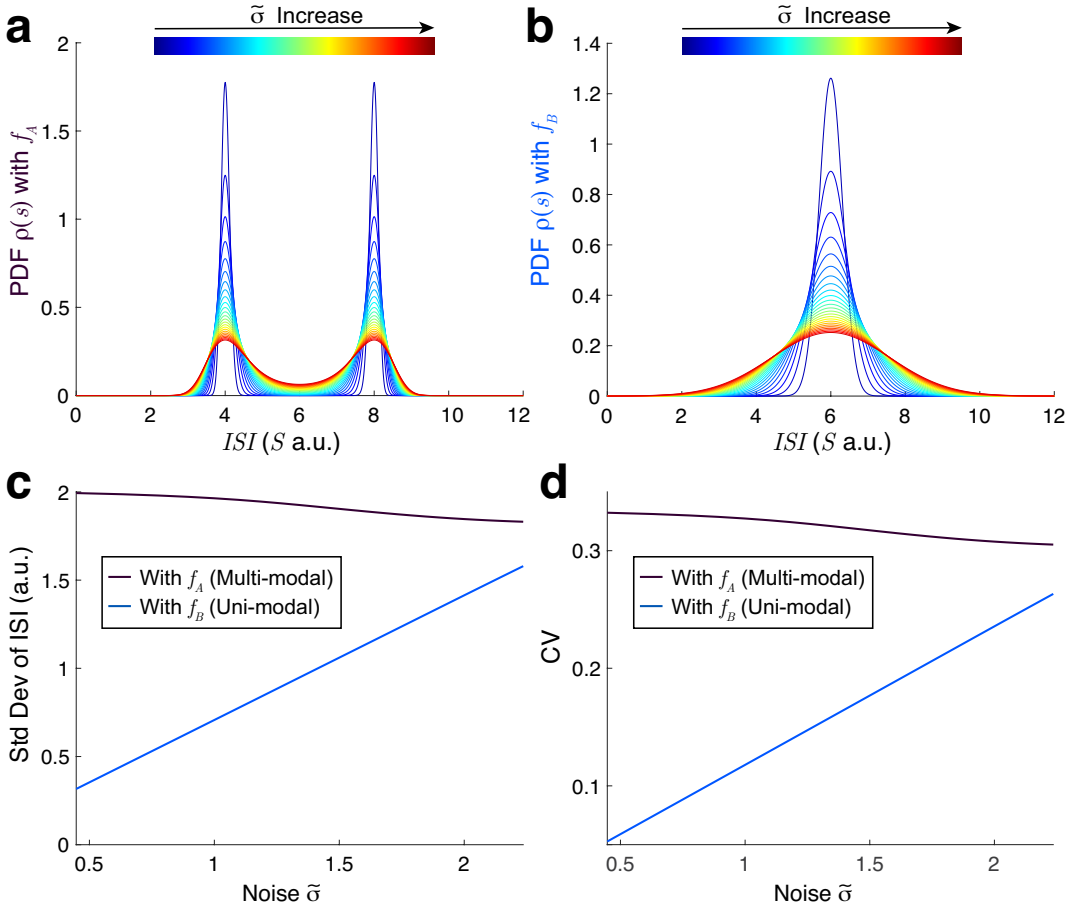

Fig. 3.4.: Phenomenological model of MC ISI (Eqs (3.5)–(3.7)) with additive noise. a) PDF of S with multiple stable fixed points (multi-modal), Eq (3.11). b) PDF of S with one stable fixed point, Eq (3.10). c) Resulting std. dev. of ISI (modeled with σ_S and CV (d) (modeled with σ_S/μ_S). The multi-modal case (blackish) with f_A shows that variability generally decreases while the uni-modal case (blueish) with f_B always increases with increasing input noise.

To capture the main results in Fig 3.3, the results in the prior paragraph suggests that the noise $\tilde{\sigma}$ has to be multiplicative (i.e., depend on S) in this specific model. Since increasing input noise generally results in a gradual diminishing of multi-modal peaks to uni-modal, we set $\tilde{\sigma}(s)$ in Eq (3.9) to be an inverted triangle with minimum at $s = 3$, and model increase in noise by an additive shift (see Fig 3.5a). These choices are arbitrary, but they nonetheless

capture the changes in the ISI distribution (Fig 3.5c,d) observed in the biophysical model (Fig 3.3e,f; the right peak broadens and flattens while left peak's height decreases as input noise increases).

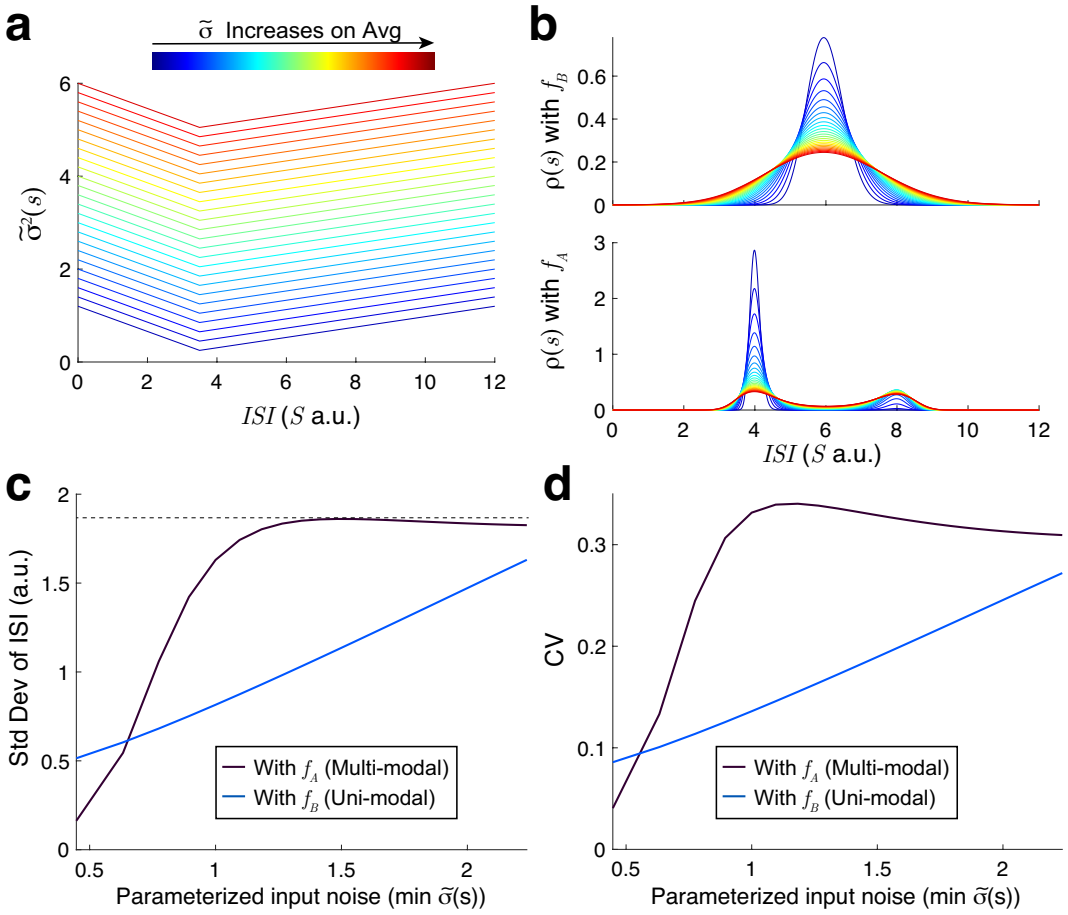

Fig. 3.5.: Phenomenological model of MC ISI (Eqs (3.5)–(3.7)) with multiplicative noise. a) Simple structure of multiplicative noise we chose (arbitrarily). b) Resulting PDFs (Eq (3.9)). c) The std. dev. and CV (d). The non-monotonic spiking variability is apparent with both f_A (multi-modal) and multiplicative noise, while with f_B (uni-modal) the resulting variability only increases.

Importantly, the uni-modal case (f_B) generally results in increases in spiking variability with noise, while the multi-modal case (f_A) exhibits an increase followed by a decrease in spiking variability as noise increase.

Taken together, we conclude that both the multi-modal peaks in the ISI and the (effec-

tive) multiplicative input noise (or ISI dependent) noise are crucial for the results we observe in this specific model. However, it is important to note that this observation is not a general fact; i.e., not all models with uni-modal ISI densities behave the same way as this scalar phenomenological model with input noise. Specifically, [79] used a simple Fitzhugh-Nagumo model with adaptation endowed with a large range of time-scales and found non-monotonic CV of spiking as input noise (and applied current) increased, with uni-modal ISI densities. Their work identifies the range of time-scales as a key signature in non-monotonic spiking CV, because when their adaptation variable has only one time-scale, the applied current (and perhaps input noise) is monotonically related to CV. See Section 3.4 and Appendix D.1 for further context.

We close with remarks about the biophysical connection and the generality of the phenomenological model results. In our specific model, the multiplicative noise $\tilde{\sigma}(s)$ does not have a direct connection to the biophysical MC model. But note that it is very common to have multiplicative noise in a reduced/transformed model from a larger biophysical model that originally has additive noise in the voltage. For example, see equation for phase reduced model (Eq (D.1)). We decided to use a state dependent $\tilde{\sigma}(s)$ for simplicity that did not require wholesale changes to the model above (Eq (3.5)–(3.7)). In our simple model (Eq (3.5)–(3.7)) the effect of $\tilde{\sigma}(s)$ is to broaden and flatten the right peak while lowering the height of the left peak while fixing the rest of the parameters. However, note that other scalar models with <u>additive noise</u> can capture the non-monotonic Std. Dev. and CV (increase followed by a decrease). For example, consider a mixture of two Gaussians with five parameters:

$$\rho_S(s) = cf_1(s) + (1-c)f_2(s);\ f_j(s) := \frac{1}{\tilde{\sigma}_j\sqrt{2\pi}} \exp\left\{-\frac{1}{2}\left(\frac{s-s_j}{\tilde{\sigma}_j}\right)^2\right\}.$$

After extensive numerical investigations, we found the simplest way to capture non-monotonic Std. Dev. and CV (increase followed by a decrease) is via: with the same s_j, let $\tilde{\sigma}_1 = \tilde{\sigma}_2$ be

the same additive input noise as in Fig 3.4a,b, and let c decrease: $c = 0.65 \searrow 0.3$.

3.4 Discussion

This paper provides insights to MC spiking variability modulation that relies first on a single-compartment reduction to pragmatically simulate large numbers of spikes, and then on a phenomenological framework to assess how input noise alters the output spike interval distribution. We find that the temporal dynamics of spiking can significantly change with input noise and that the spiking variability (measured by ISI) does not monotonically increase with biophysically realistic input noise level. These dynamics may impact odor processing as MCs are an important type of relay cells in the olfactory bulb that propagate odor information to downstream cortical brain regions. We remark that tufted cells, which we did not explicitly consider here, are also known to have a similar function. There is a recently developed tufted cell model [82] that may be simple enough to analyze in the same vein as here, and might be considered in future research.

Although we do not consider a comparison of an odor processing task between: i) MC model with a monotonically increasing relationship between spike variability and input noise, and ii) MC model with a non-monotonic relationship, we highlight possible implications of our results on OB odor processing. The input noise to MC comes from numerous sources, including olfactory receptor neurons (**ORNs**) from upstream, and within OB there are granule, periglomerular cells, and excitatory interneurons that are presynaptic to MC. So how the input noise precisely varies for a specific odor task is difficult to determine, but it is plausible that the input noise increases with odor compared to spontaneous activity via ORN inputs [83] – input noise could also change when there are multiple similar odors compared to a single odor [84], and in a multitude of ways. The MC spiking variability across trials is important for olfactory processing – awake behaving rats show reliable MC spiking for a given odor [67] with relatively small trial variability (see Fig 1D, 2A, 2C in

[67]). In zebrafish, [83] showed that MC spike variability (across trials) increased after odor presentation followed by dramatic decreases, which coincided with better odor identification as time proceeded from odor presentation. We did not consider populations of MC, but [83] found that decorrelation across populations of MCs played a large role in odor identification, consistent with [85]. Therefore, how MC spike variability modulates as input noise increases, particularly when a decrease in MC spiking variability is possible with increased input noise for physiologically relevant firing rates, could be important for odor processing.

3.4.1 Analyzing simulation results

There is often a trade-off between mathematical analysis and biological realism in model analysis, our results here focus on a realistic MC model. Some modelers have used simple MC models ([86, 87, 39] and even very recently: [76, 88, 89]) that, despite the virtue of these works, could result in overlooking important MC spiking behavior when the spike variability is crucial.

Describing the complexities of the ISI density in our single cell MC model with a quantitatively accurate reduction method is elusive, at least to the best of our knowledge. With constant current input, phase reductions methods are commonly used to analytically capture spiking dynamics when the time between spikes are relatively regular (which does not hold in the models here). Using such approaches to approximate the dynamics with a single scalar variable would yield approximations where the spiking variability monotonically increases with input noise [90] (see Appendix D.1), in contrast to our results. There have recently been a plethora of advances in phase reduction theory using more than one state variable (i.e., amplitude variables, not just phase) that can sometimes be viable for analysis [91, 92, 93]. For example, the standard assumptions of weak coupling [91] and noise [94, 95] can be relaxed in some of these formulations. However, the assumption of (nearly) periodic dynamics must still hold in all of the methods mentioned. These contemporary phase re-

duction methods generally require two or more state variables which often rely on numerical simulations anyway – we are unaware of any phase reduction theory where the approximate ISI density is readily available.

Another common analytic approach to understanding the effects of weak noise on (output) spiking in excitable systems is using the Arrhenius escape rate, i.e., potential well models, that have been successfully applied to many systems [79, 96, 97, 98, 99, 100]. Many of the derived formulas for the ISI distribution (see Appendix D.1 for more details) in these prior works are too simplistic for our MC model. However, using a separation of time-scales, [79] were able to analytically describe, with an Arrhenius-escape framework, the spiking dynamics of an excitable Fitzhugh-Nagumo model with multiple time-scales in the adaptation variable. Indeed, [79] found a non-monotonic relationship of the CV with input noise (in their Fig 2, see cross-section with a fixed I). Their approach applied to our MC model would require identifying all of the effective time-scales in our 13 variable model *and* having a significant separation of time-scales, then the slower variables are assumed to be fixed (then slowly varying) and the faster variables are included in the potential dynamics (see [96] too, also see Appendix D.1 for more details). The viability and the accuracy of this approach for capturing our results is an open question but beyond the scope of this current study. Our description of this particular non-monotonic relationship of escape rate (or spiking) variability with input noise in a large dimensional model compliments the results of [79] as an understudied phenomena not observed in standard/simple spiking models.

The result that the spiking variability is non-monotonic and maximal at an intermediate input noise value (for physiological firing rates) might seem related to the stochastic resonance phenomena that has been observed and analyzed in many areas of science [101]. Stochastic resonance refers to an optimal (maximum) response (i.e., firing or signal to noise) at an intermediate noise level [102]; or the related coherence resonance where there is an optimal frequency of sinusoidal input to illicit maximum responses [103, 104, 102]. Firing

rate response is different than spiking variability as measured by σ_{ISI} and CV. Although note that [102] showed an optimal level of input noise could minimize CV in a Fitzhugh-Nagumo model, which is the opposite of what we observe here (also see Appendix D.1).

Although we have observed a non-monotonic relationship between simple uncorrelated white noise input and output spiking variability (i.e., CV), note that there are other studies that have described dependence of CV on more complicated input types (e.g., with temporal correlation or adaptation and other features [105, 95]). We have considered a specific biological model for an important olfactory bulb cell, in contrast to these other papers that have analyzed general spiking models with some attributes – whether they are directly related to this paper is unlikely in our opinion, but could be explored in future research. Beyond the ISI, there are other statistical measures of a spike train, such as the autocorrelation and power spectrum, that could be unrelated to the ISI histogram (see Appendix D.2).

3.4.2 Limitations

There are several limitations of the work here. First, in the actual neural network, MCs are known to be coupled to other specific cells in the bulb (e.g., granule and periglomerular cells and other excitatory interneurons), and receive feedback input from piriform cortex. Related to this point, stochastic inputs can at times have more complex structure than white noise, even when considering an average over many cells. The synaptic coupling in the olfactory bulb is distinct from other neural networks, mediated by dendrodendritic interactions that results in faster coupling than the standard axon-to-dendrite coupling. These and other physiological details could change our results, at least quantitatively. Considering such extensions is an interesting avenue for future work.

CHAPTER 4

OLFACTORY BULB ENCODING OF ORTHO VERSUS RETRONASAL ODORS

4.1 Introduction

Olfaction is driven by odor molecules entering the nasal cavity that induce a cascade of action potentials in the nervous system to transmit and process odor information. There are two routes by which odor molecules can enter the nasal cavity: from the nose during inhalation and sniffing (**ortho**), or from the throat during exhalation and while eating and drinking (**retro**). Olfaction is primarily studied with orthonasal stimulation and is thus the basis for much of our understanding of odor processing. Prior imaging studies have shown differences in the activation of the regions of the nasal epithelium (before cortical processing) with ortho and retro stimulation [23, 6, 24], but we do not know whether ortho/retro information is transmitted to cortical brain regions, nor do we know the network attributes that promote efficient encoding of ortho versus retro input. Here, we show that the mode of the input stimuli (ortho versus retronasal) is indeed transmitted to cortical brain regions using *in vivo* rat data of the olfactory bulb (**OB**).

Before odor information reaches the brain, it is processed in the OB and relayed to higher brain regions via excitatory mitral cells (**MC**s) (and tufted cells). Thus, this area is critical in understanding whether ortho versus retronasal odors are encoded before being conveyed to the brain for decoding. Prior studies have shown MC response timing to orthonasal odors in relation to the sniff cycle is affected by inhibition [106, 77]. Ortho and retronasal stimuli emerge from the inhale and exhale, respectively, of the breath cycle, and we observed in Chapter 2 that temporal differences play a critical role in OB processing of the two routes.

Thus, we expect inhibition to influence OB processing of both ortho and retronasal despite not currently knowing the role of inhibitory cells.

To understand the OB circuit mechanisms that promote this encoding, we use two different drug preparations to manipulate fast inhibitory synapses and assess the affects on decoding: **Mus**cimol ($GABA_A$ agonist, overall increased inhibition), and **Bic**uculline($GABA_A$ antagonist, overall decreased inhibition). We found inhibition does indeed alter decoding accuracy and OB processing of ortho versus retro odors. In particular, we found baseline inhibition (no drug) to have the highest average decoding accuracy, and to be significantly higher than both drug preparations with altered inhibition. Additionally, we found that inhibitory drugs affected population-averaged firing rates differently for the two stimulus routes. The drugs altered ortho firing rates as expected (i.e., increasing with less inhibition, decreasing with more inhibition), but retro firing rates were not significantly changed between no drug and inhibitory drug preparations. Lastly, we find that the trial-to-trial variances of the various drug preparation align with the decoding accuracies. In other words, no drug preparation has both the largest average decoding accuracy and trial variance, while the inhibitory drugs have smaller average decoding accuracies and trial variance.

We then used these findings as the basis for constructing a Wilson-Cowan firing rate model to replicate the MC responses with different stimuli and levels of inhibition. Interestingly, our model better mimics differing drug effects on ortho vs retro firing rates observed in the rat data when including synaptic plasticity. In particular, we found synaptic depression to be the most effective plasticity rule in capturing these effects. Not surprisingly, other studies have found plasticity within the OB circuitry [107, 108, 109], and more specifically short-term depression [110]. Lastly, the model is able to replicate decoding accuracy differences between drug preparations while retaining trends of associated trial-variances.

The analyses and findings described above were from anesthetized rat data that do not explicitly account for natural breath cycles and sniffing behavior. Thus, we replicate

the data analysis on awake mice data previously collected from other studies [111, 112, 113]. The awake data analysis confirms that ortho versus retronasal stimulus information is transmitted to cortical brain regions by the OB. Additionally, differences in inhibition were found to alter decoding accuracy and have differing effects on firing rate for only one of the two stimulus routes. However, we observed contrasting trends in that baseline inhibition (no drug) had the lower average decoding accuracy and retronasal stimulus firing rate was affected by drug preparation while orthonasal was not. The anesthetized and awake data sets are not flawlessly comparable, thus, we believe these findings are a starting point from which the methodology and insights could be used to inform future experiments.

4.2 Materials and methods

4.2.1 Anesthetized data analysis

Data was collected *in vivo* from the mitral cell (**MC**) layer in the olfactory bulb (**OB**) of multiple anaesthetised rats using a multi-electrode array recording. The data consisted of spike recordings of multiple MC spike responses to Ethyl-Butyrate (**EB** - a food odor) presented by the two routes of stimulation, orthonasally and retronasally, for a total of 20 trials (10 ortho, 10 retro). The spike counts were calculated using 100 ms overlapping time windows over duration of a 30 s trial. However, we consider the spontaneous state to be 3 s before odor onset (defined as $t = 0$), and the evoked state to be the 1 s of odor presentation as well as 1 s of activity after odor is no longer present (i.e., 2 s total evoked state time). Further, three separate drug preparations were used in order to analyze inhibitory effects on MC spiking responses: no drug (control), bicuculline ($GABA_A$ antagonist, i.e., decreasing inhibition), and muscimol ($GABA_A$ agonist, i.e., increasing inhibition). See Table 4 for total number of rats and respective individual cells for each drug preparation.

We used a form of linear discriminant analysis (**LDA**) to define decoding accuracy, using a threshold that gives the maximum decoding accuracy. The decoding accuracy is the

Table 3.: Number of anesthetized rats and respective individual cells for each drug preparation.

EB	No Drug	Bicuculline	Muscimol
Rats	8	4	3
Cells	913	413	419

fraction of trials correctly classified by a threshold. We define the set of observations ($\vec{x_k}$) for all trials $k = 1, 2, ..., K$ as the sum of the evoked spike counts ($s_k(t)$ where $t \in [0, T]$) normalized by subtracting off the mean spontaneous activity (μ_k^{sp} where $t < 0$). We refer to this as the normalized summed spike count, $\vec{x_k}$ for trial k, more succinctly summarized as:

$$\vec{x}_k = \sum_{t=0}^{T} (s_k(t))/T - \mu_k^{\text{sp}}$$

The data consists of $k = 20$ trials total (10 ortho/10 retro) for each individual cell. We consider all possible thresholds θ_k:

$$\begin{cases} \theta_k = x_k - \epsilon, & x_k = \max(\vec{x}_k) \\ \theta_k = x_k + \epsilon, & \text{else} \end{cases}$$

where an optimal threshold θ^* is determined for each individual cell as the θ that results in the most accurate separation of ortho/retro observations (the $\epsilon \approx 10^{-16}$ denoting machine precision).

In order to more efficiently analyze the differences in decoding accuracy with different drug preparations, we selected the time windows that resulted in the most significant differences. We evaluated decoding accuracy from 100 ms to 1 s in 100 ms increments in the evoked state for each drug preparation. We then used a two sample t-test assuming unequal variances between no drug preparation and bicuculline as well as no drug preparation and muscimol. This resulted in 10 different $p-$values corresponding to each time window

where the most significant $p-$values for both combinations of no drug/bicuculline and no drug/muscimol determined the optimal time window. Additionally, we repeated this process with three different lengths of time in the spontaneous state (1 s, 2 s, and 3 s) with which the evoked summed spike counts were normalized. The optimal time window (t^*) was determined to be 900 ms in the evoked state and 2 s in the spontaneous state. See Figs E.1 and E.3 for these results.

The available data included MC spike responses to two different odors, Ethyl-Butyrate (EB- a food odor) and 1-Hexanol (Hex- a nonfood odor). However, stimulation with Hex did not result in consistently significant differences in average decoding accuracy between different drug preparations (see Fig E.2). Moreover, the population-averaged PSTH showed no differences in either ortho or retro stimulation when bicuculline or muscimol was applied (Fig E.4). Therefore, we decided to focus our analysis on EB food odor that contrarily resulted in consistently significant differences in net decoding accuracy with different drug preparations (see Figs E.1 and E.3). Note that natural retronasal olfaction only occurs with food odors [2], so it stands to reason that animal brains might not be structured to distinguish ortho versus retro stimulation with non-food odors.

4.2.2 Awake data analysis

Data from Bolding & Franks [111] was used to conduct analogous analysis of decoding accuracy in awake mice. The data include electrophysiological recordings of OB MCs in response to different odors including EB used in our anesthetized data. Further, the data have simultaneously recorded MC responses to odor with baseline levels of inhibition and with decreased inhibition from selectively blocking piriform cortex (**PCx**) centrifugal projections. This was done by injecting adeno-associated viruses (**AAVs**) into one hemisphere of the PCx to selectively express tetanus toxin light chain (**TeLC**) in cortical principal cells. The expression of TeLC blocks transmitter release from all synapses in AAV infected cells,

including centrifugal projections from PCx back to the OB. The centrifugal inputs from PCx contact GABAergic OB neurons that ultimately suppress MC (and tufted cell) output [64, 65]. Thus, the non-infected PCx and associated OB hemispheres receiving centrifugal projections will have the expected, control levels of MC firing while the infected PCx and associated OB hemispheres not receiving centrifugal projections will have increased MC firing from decreased GABAergic neuron inhibition. In this way, we are able to compare awake odor response with varying levels of inhibition most similar to the no drug and bicuculline drug preparation used in the anesthetized data. The methods used for collecting this data is described in further detail in [113, 112].

The awake data [111, 112, 113] was collected to understand the role of recurrent cortical circuits in concentration-invariant coding, with regard to only the orthonasal route. Thus, there was no distinction between orthonasal and retronasal stimulus routes. However, since orthonasal and retronasal routes are associated with the inhale and exhale of the breath cycle, respectively, we specified inhale time window as orthonasal and exhale time window as retronasal, see Fig 4.6A for depiction. Breath cycle was determined in Bolding & Franks [112] by measuring respiration using a microbridge mass airflow sensor (Honeywell AWM3300V) positioned directly opposite the animal's nose. Thus, decreasing of air flow aligns with inhale (i.e., ortho) and increasing of air flow aligns with exhale (i.e., retro). However, this measurement is prone to noisy fluctuations over time, so the original respiration measurements were filtered using a zero-phase digital filter of the measurements in both the forward and reverse directions, with a 2nd-order low pass digital Butterworth filter with normalized edge frequencies of 1.0000e-05 and 0.007 (note: these are scaled based on 2 kHz sampling rate of data). This results in zero phase distortion; a filter transfer function equal to the squared magnitude of the original filter transfer function; and a filter order that is double the order of the filter specified by the Butterworth filter output. Finally, we perform a Hilbert Transform of the zero-phase digital filter to gather the phase angle in the interval $[-\pi, \pi]$ for

each element of the analytical signal. From this filtering, we have a smooth filtered phase representation of the noisy air flow measurements to more readily determine the length of the breath cycle and what times correspond to inhale/exhale. See Fig E.5 for comparison of original airflow over time to filtered phase for all 4 rats and 10 trials.

With the distinction of ortho versus retronasal time windows, we measured the respective spike counts $s_k(t)$ during the first breath cycle after each EB odor was presented for the k^{th} trial. This was done by defining $t = 0$ as the start of first inhale after stimulus (always = stimulus onset time, see Fig E.5), phase switch at filtered phase = $-\pi$ to indicate end of inhale and start of exhale, and end of exhale at filtered phase = 0. Note, the time windows T_k of inhale and exhale were variable within trials and between trials, therefore we use the firing rate (Hz) $\vec{R}_k$ defined by equation below as input for LDA.

$$\vec{R}_k = \frac{1}{T_k} \sum_{t=0}^{T_k} s_k(t)$$

We have $k = 10$ trials total (10 ortho/10 retro) for each individual cell. See Table 4 for number of rats and cells for each drug preparation. We use the same methodology as described in 4.2.1 to determine the optimal decoding threshold θ^* for each individual cell resulting in the most accurate classification of ortho/retro stimulation.

Table 4.: Number of awake rats and respective individual cells for each drug preparation.

EB	No Drug	TeLC
Rats	4	4
Cells	71	66

4.2.3 Firing rate model

We can reduce neuron cell types to either excitatory (**E**) or inhibitory (**I**) neurons since we focus on individual MC decoding. These classifications relate to the type of synaptic

connection of these (presynaptic) cells have to their postsynaptic cells. An excitatory cell causes the postsynaptic cell to increase in voltage while the inhibitory cell causes the postsynaptic cell to decrease in voltage. The OB is made up of clusters called glomeruli that have reciprocally coupled networks of E/I cells: Mitral Cells (MC - E), Granule Cells (**GC** - I), and Periglomerular Cells (**PGC** – I).

Assuming a large population of densely coupled neurons, we use a space-clamped Wilson-Cowan firing rate model of coupled E-I cells: MC (excitatory) and PGC/GC (inhibitory). The models of the respective cell firing rate, $A_j(t)$ $j \in (E, I)$, are modeled by the following ordinary differential equations:

$$\tau_E \frac{dA_E}{dt} = -A_E(t) + F_E(w_{I,E} I_E(t) - w_I S_I(t)) \tag{4.1}$$

$$\tau_I \frac{dA_I}{dt} = -A_I(t) + F_I(w_{I,I} I_I(t) + w_E S_E(t)) \tag{4.2}$$

where the synaptic term, $S_j(t)$ $j \in (E, I)$, is defined by alpha-synapses with rise and decay time scales (same τ_{rise}, τ_{decay} for E/I) as follows:

$$\tau_{\text{decay}} \frac{dS_j(t)}{dt} = -S_j(t) + X_j(t) \tag{4.3}$$

$$\tau_{\text{rise}} \frac{dX_j(t)}{dt} = -X_j(t) + \tau_{\text{rise}} A_j(t) \tag{4.4}$$

In Eqs 4.1 and 4.2, $I_j(t)$ is the sum of external currents (e.g., cortical feedback, stimulus input, etc.) that varies over time to account for stimulus input (i.e., spontaneous versus evoked state), $w_{I,j}$ are the coupling strengths of olfactory receptor neuron (**ORN**) input to respective cell j, w_j are the respective coupling strengths from cell j to the other cell, and the function F is assumed to be a piece-wise linear function:

$$F_j(x) = \max(x - x_{\min}, 0), \quad j \in \{E, I\} \tag{4.5}$$

where $x_{\min}$ is the minimal current needed to induce firing. Neurons are known to linearly filter inputs, and this linearity makes it possible to analyze this function.

In order to account for the different inhibitory drug effects (i.e., less inhibition with bicuculline and more inhibition with muscimol) we change the inhibitory synaptic strength(w_I) to be larger or smaller for more or less inhibition, respectively. We then considered the effects of including synaptic plasticity in the model for capturing the drug effects observed, described in Section 4.3.2. Specifically, for the excitatory weight (w_E) we define:

$$\tau_w \frac{dw_E}{dt} = -w_E + A_E(t) \tag{4.6}$$

where

$$F(x) = \frac{2}{1+e^x} - 1 \tag{4.7}$$

In order to account for differences in ortho versus retronasal stimulus, we define ORN input, $I_j(t)$ $j \in (E, I)$, as time-varying. We define ortho-like ORN input, $I_O(t)$, to increase and decay faster than retro-like ORN input $I_R(t)$, with odor onset at time 0 s based on prior imaging studies [6, 24].

Lastly, we simulate trial-to-trial variance of spike counts as a negative binomial random variable:

$$\mu_{NB} = \frac{r(1-p)}{p} \tag{4.8}$$

Given output from the Wilson-Cowan model (Eqs 4.1 and 4.2), we define:

$$\mu_{NB} = \int A_M(t)dt \tag{4.9}$$

Through trial and error, we elected to use the values listed in Table 5 to define p where then by construction $r = \mu_{NB}p/(1-p)$.

Table 5.: Values defined for negative binomial p for different stimulus type and drug preparations.

Drug Prep	Ortho	Retro
No Drug	0.000155	0.000155
Muscimol	0.0001	0.00004
Bicuculine	0.00015	0.00015

4.3 Results

The results from Chapter 2 suggest that pre-cortical decoding of ortho/retro may be possible since we observed differences in the processing of the two stimulus routes at the OB level. Further, previous studies have shown inhibition plays a role in modifying MC response timing [106, 77]. Therefore, we first determined if ortho/retro are distinguishable at the individual cell level, and then whether inhibition affects OB encoding of the two routes.

4.3.1 LDA results

To get a more precise understanding of whether OB cells can decode ortho versus retronasal stimulus, a summary of methodology and results for conducting LDA of individual cell decoding accuracy can be found in Fig 4.1. As evident in Fig 4.1D, we find OB MCs are able to discriminant between ortho and retro odors since the decoding accuracies are between 0.5 (i.e., chance) and 1 (i.e., perfect decoding), with no drug having mean decoding accuracy of 0.74, and both drug preparations have mean decoding accuracy of 0.69. Further, the difference in decoding accuracy is statistically significant ($\alpha = 0.01$) between no drug and both drug preparations using two-sample T-test, Wilcoxon rank-sum test, and one-way ANOVA. Refer to Figs E.1 and E.3b for $p-$values.

Figure 4.1E shows proportion of ortho- and retro- selective cells as measured by the

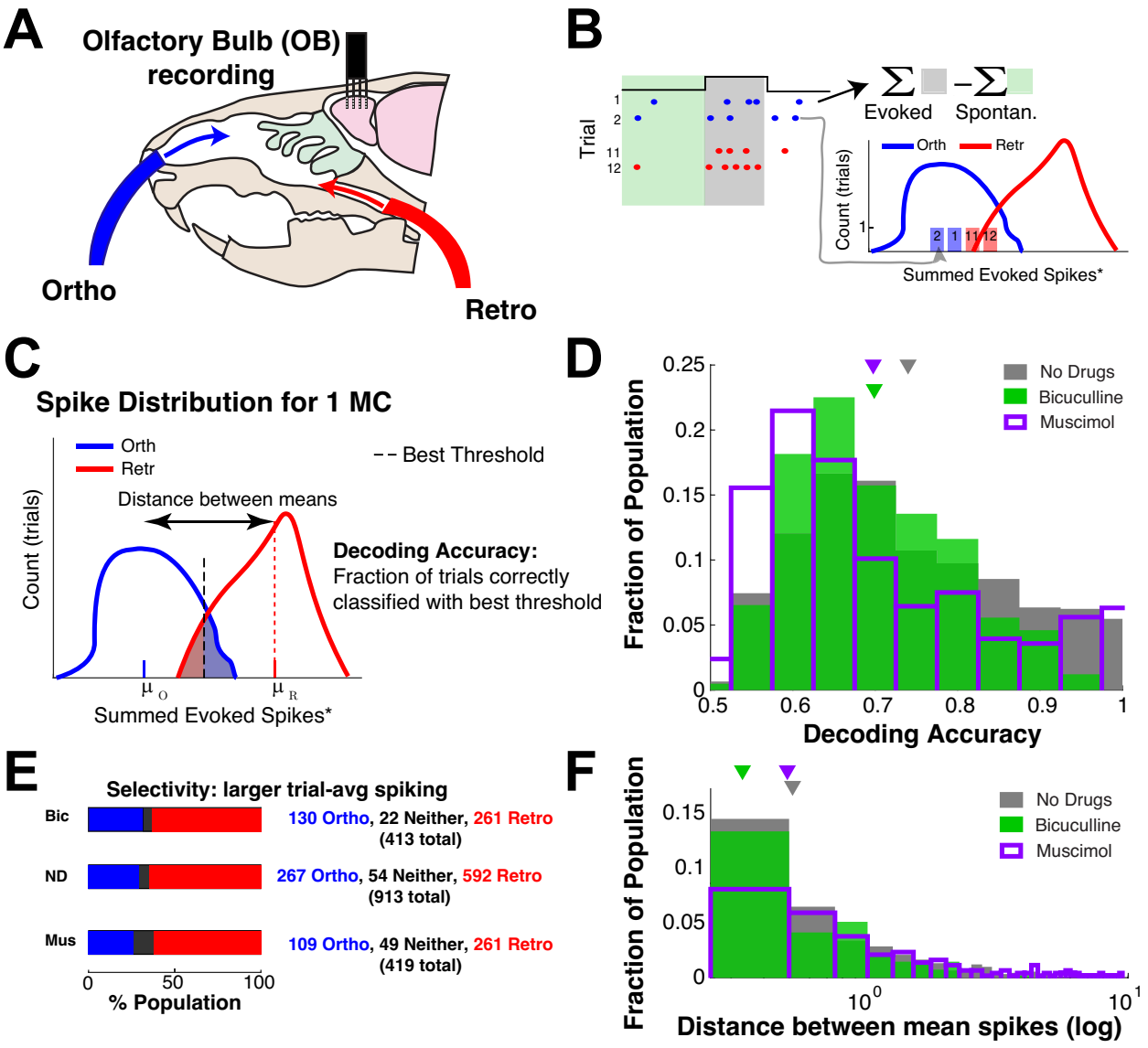

Fig. 4.1.: Methodology and summary of anesthetized *in vivo* rat individual cell decoding accuracy using LDA.
A) Diagram of *in vivo* multi-electrode array recordings of anesthetized rat OB with orthonasal (blue) and retronasal (red) stimulus routes. B) Summary of method for calculating the normalized summed spike count, $\vec{x}_k$ for trial k described in Subsection 4.2.1 C) Summary of method for determining best threshold, calculating distance between means, and defining decoding accuracy. D) Histogram of individual cell decoding accuracies for each drug preparation where the mean is denoted by triangles. E) Proportion of cell selectivity based on larger trial-average spiking for each drug prep. F) Histogram of distances between (trial-averaged) means; no drug is largest but only statistically significantly larger than bicuculline (not muscimol).

larger trial-avg firing. To better understand the dynamics of decoding, we consider the spike count distributions for ortho versus retronasal and calculate the distance between trial-averaged means (Fig 4.1C). The histograms depicting these distances are in Fig 4.1F, showing that no drug preparation indeed has the largest distance (on average) between ortho and retro spiking compared to the other drug preparations. This difference is significant ($\alpha = 0.01$) for bicuculline, however, it is not statistically significant for muscimol. The distance between ortho and retro mean spiking is strongly related to decoding accuracy for each individual cell – Fig 4.2A shows that there is a clear correlation (stronger rank correlation than Pearson's).

4.3.2 Comparing drug effects

Given that the individual cell LDA decoding accuracies were effected by inhibitory drugs and that in all cases the distance between the trial-averaged spiking and decoding accuracy were related, we considered the how the drugs effected the population firing rates with ortho and retro stimulation (Fig 4.2). As expected, muscimol (increased inhibition) causes firing rates to generally decrease and bicuculline (less inhibition) generally leads to increased firing. Within a given mode of stimulation, the evoked firing rates for ortho stimulus (Fig 4.2A) are significantly different ($\alpha = 0.01$) between all drug preparations for nearly all time points. This is more clearly shown by the distinguishing separation of curves in Fig 4.2B. However, with retro stimulation, the differences in evoked firing between drug preparations is no longer significantly different (Fig 4.2B).

The differences in drug effects given different stimulus type observed in Fig 4.2 led to our formulation of predictions on how these differences affect decoding accuracy. Drugs were observed to not significantly change retro spiking response, therefore we assume the distribution to be nearly invariant. Then, if orthonasal spiking response is assumed to significantly change (muscimol decreasing firing rate, shifting spike response left; bicuculline increasing firing rate, shifting spike response right) we get the resulting overlapping of ortho

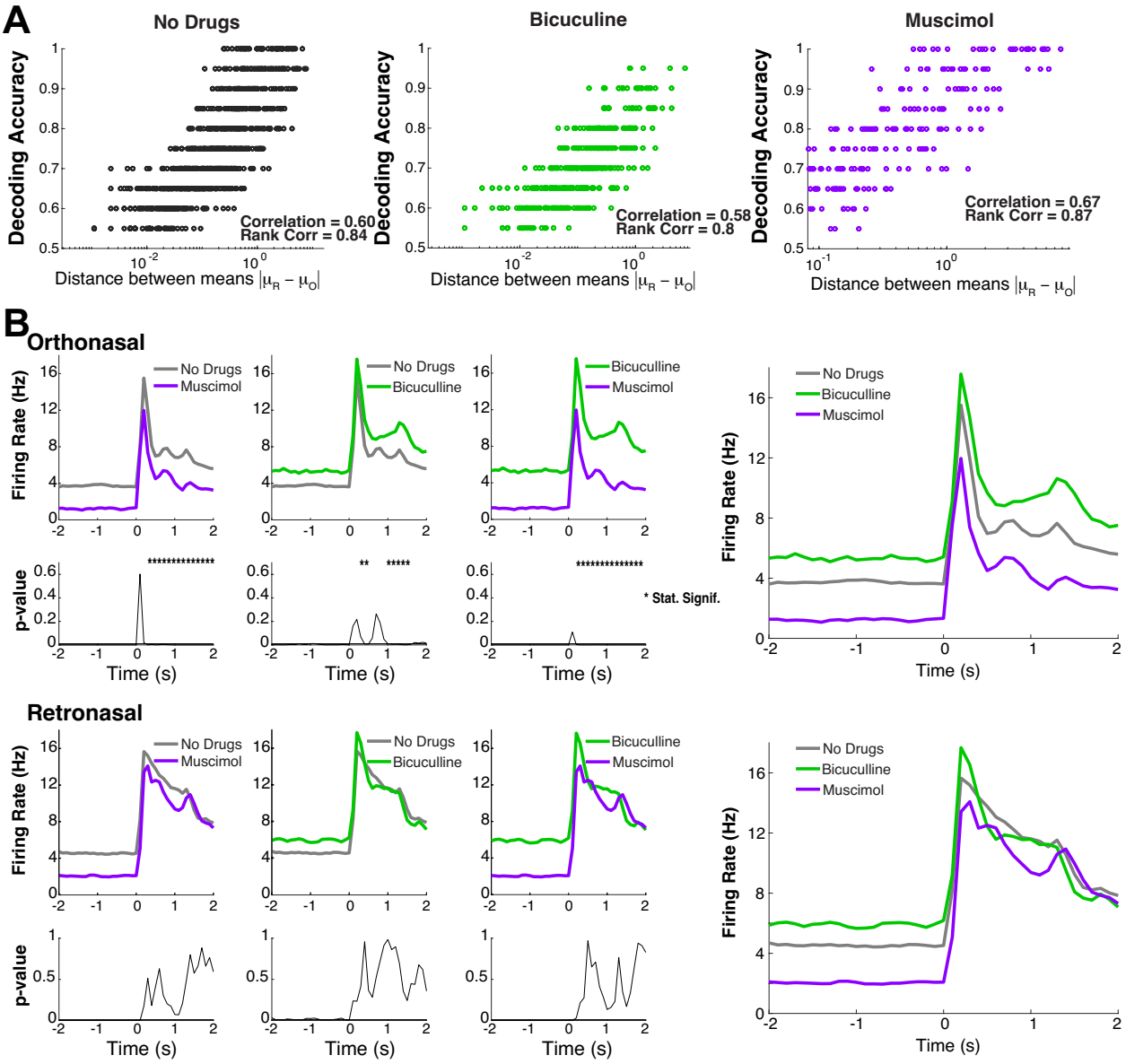

Fig. 4.2.: Population firing rates of anesthetized *in vivo* rat data comparing inhibitory drug effects for both stimulus types.
A) Distance between normalized summed spike count means $|\mu_R - \mu_O|$ is strongly related to decoding accuracy for each drug preparation along with listed Pearson's correlation (referred to as "correlation") and rank correlation. B) Firing rates and respective two-sample T-test p-values for orthonasal (top) and retronasal (bottom) stimulus comparing drug combinations (left - no drug/muscimol, center left - no drug/bicuculline, center right - bicuculline/muscimol). Far right image shows overlay of all drug preparation firing rates given orthonasal (top) and retronasal (bottom) stimulus.

versus retronasal odor distributions for $\mu_R > \mu_O$ (4.3A) and $\mu_O > \mu_R$ (4.3B). Thus, the predictions from the data are as follows:

1. When $\mu_O < \mu_R$:
   (a) Bicuculline = less accuracy*
   (b) Muscimol = more accuracy
2. When $\mu_R < \mu_O$:
   (a) Muscimol = less accuracy*
   (b) Bicuculline = more accuracy

The results of these predictions are shown in Figs 4.3C (prediction 1a), 4.3D (prediction 2a), 4.3E (prediction 1b), and 4.3F (prediction 2b). Predictions 1a and 2a denoted by asterisk are statistically significant in difference ($\alpha = 0.01$). The other two predictions (1b and 2b shown in Figs 4.3E and 4.3F, respectively) do not hold and the differences in means are not statistically significant. However, the predictions are partially validated as follows. In Fig 4.3E restricting to cells with $\mu_O < \mu_R$ with musicmol leads to a statistically significant increase in the average decoding accuracy when compared to all cells with muscimol, but the increase is not large enough to be significantly greater than no drug. In Fig 4.3F, restricting to cells with $\mu_R < \mu_O$ with bicuculline leads to an increase in decoding accuracy, so much so that it is statistically indistinguishable from the no drug case (but not significantly larger than no drug).

4.3.3 Model results

The model (Eqs 4.1 and 4.2) results are shown in Fig 4.4, comparing model output with and without synaptic depression. In both cases, the model results follow the firing rate trends as observed in Fig 4.2. Specifically, orthonasal MC firing rates (top left in Fig 4.4)

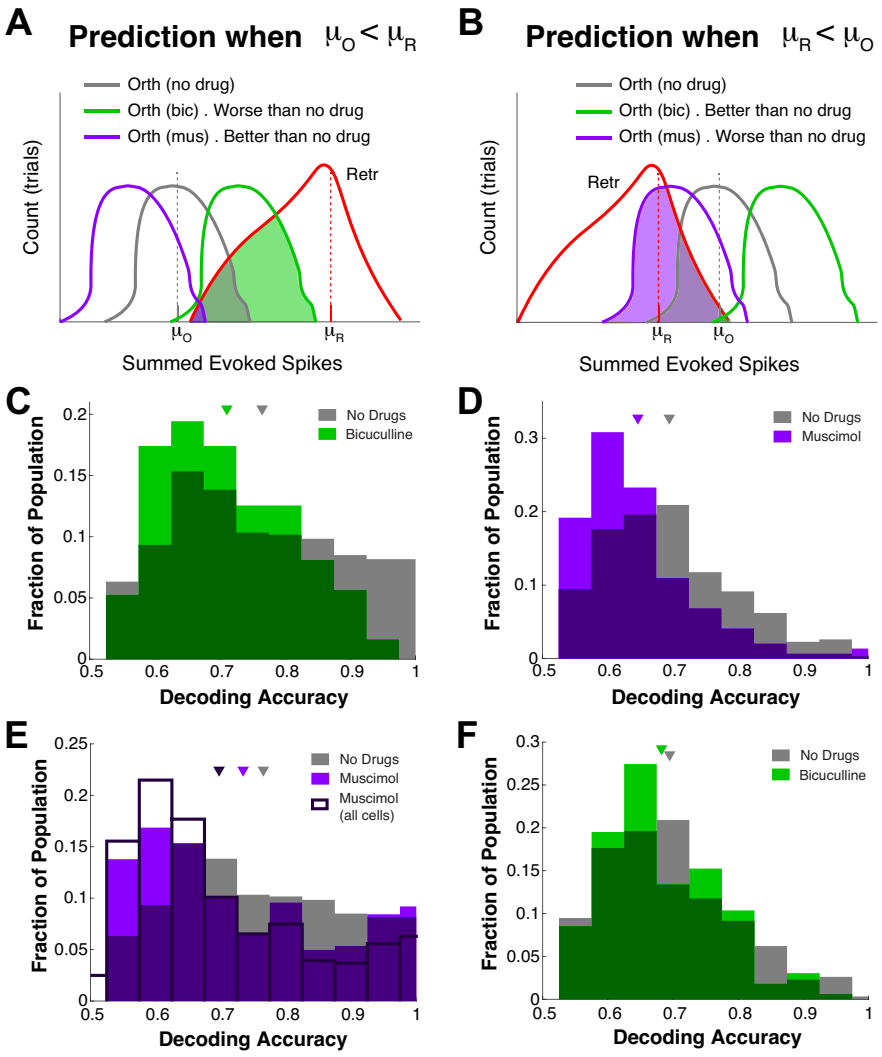

Fig. 4.3.: Summary of decoding accuracy predictions based on observed differences in drug effects on anesthetized *in vivo* firing rates.

A) Summary of prediction of decoding accuracy for different drug preparations given $\mu_O < \mu_R$. B) Summary of prediction of decoding accuracy for different drug preparations given $\mu_R < \mu_O$ C) Histogram of decoding accuracies for no drug and bicuculline given $\mu_O < \mu_R$ where mean decoding accuracy is denoted by triangle. D) Histogram of decoding accuracies for no drug and muscimol given $\mu_R < \mu_O$ where mean decoding accuracy is denoted by triangle. E) Histogram of decoding accuracies for no drug and muscimol given $\mu_O < \mu_R$ where mean decoding accuracy is denoted by triangle. Further, shown in outlined dark purple is the histogram for muscimol decoding accuracy for all cells (i.e., not only those where $\mu_O < \mu_R$). F) Histogram of decoding accuracies for no drug and bicuculline given $\mu_R < \mu_O$ where mean decoding accuracy is denoted by triangle.

with different drug preparations are most distinctly separated than retronasal MC firing rates (bottom left in Fig 4.4). In comparing model output with or without synaptic plasticity,

we see the drug effects are enhanced (i.e., less difference between retronasal firing rates with different drug preparations) when synaptic depression is included (see Tables 6 and 7 for relative differences). This aligns with findings that synaptic short-term depression exists in synapses from MC to GC [108].

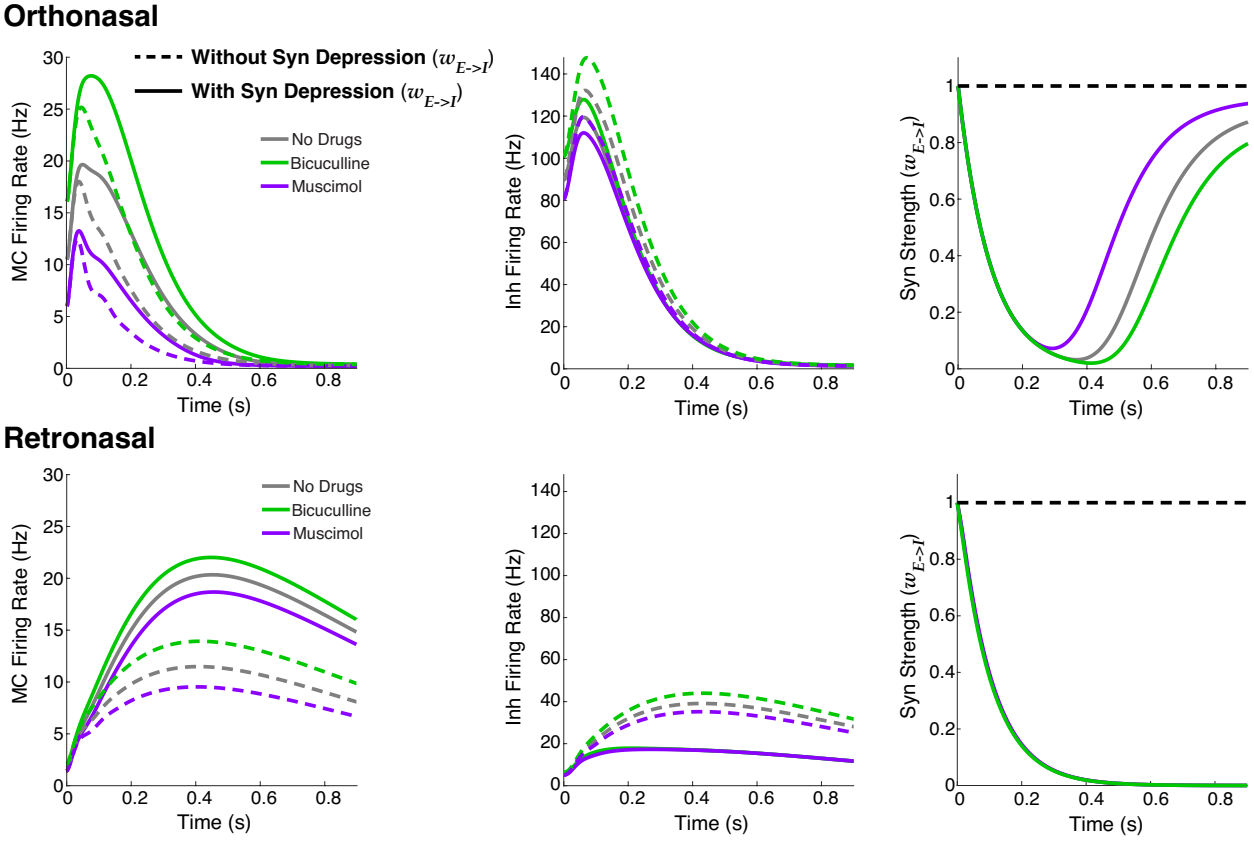

Fig. 4.4.: Comparison of firing rate model results with and without synaptic plasticity. Wilson-Cowan firing rate model (as described by Eqs 4.1 and 4.2) output for orthonasal (top row) and retronasal (bottom row) stimulus compared when synaptic depression is included (solid lines) or not included (dashed lines). Left column - excitatory MC output, center column - inhibitory PGC output, and right column - synaptic strengths ($W_{E\to I}$).

Lastly, we evaluate decoding accuracy given a simulated trial-to-trial variability as a negative binomial random variable with parameters $r > 0$ and $p \in (0, 1)$. Based on the model output, we set the mean to be

$$\int_0^T A_E(t)\, dt = r\frac{1-p}{p}, \tag{4.10}$$

Table 6.: Firing rate model output relative difference between no drug and inhibitory drugs for retronasal stimulus without plasticity.

Retronasal without Plasticity	Relative difference (%)
No drug/Bicuculline	20.97
No drug/Muscimol	16.84

Table 7.: Firing rate model output relative difference between no drug and inhibitory drugs for retronasal stimulus with plasticity.

Retronasal with Plasticity	Relative difference (%)
No drug/Bicuculline	8.88
No drug/Muscimol	8.69

manually varying p (see Table 5) to match the mean decoding accuracies in the data (0.74 for no drug, 0.69 for muscimol and bicuculline). Once p is determined, we set $r = \frac{p}{1-p}\Big(\int_0^T A_E(t)\,dt\Big)$ from Eq. (4.10). These results are summarized in Figs 4.5A)–C), showing that the model decoding accuracy captures the data trend by construction.

Figure 4.5D show that the values defined for p(O/R,ND/Bic/Mus) (see Table 5) in the negative binomial in Fig 4.5A)–C), consistently maintain decoding accuracy trends. The points on this plot are created by varying the mean firing rate model simulations $\int_0^T A_E(t;\text{O/R,ND/Bic/Mus})\,dt$ (solid curves in Fig 4.4 left panel) such that we define:

$$\mu^* = \int_0^T A_E(t;\text{O/R,ND/Bic/Mus})\,dt \pm M$$

$$r^* = \mu^* \frac{p(\text{O/R,ND/Bic/Mus})}{1-p(\text{O/R,ND/Bic/Mus})}$$

This gives different means of spike counts (averaged over trials) for ortho and retro, and thus different decoding accuracies from the simulated trial-to-trial variability. The values of M were chosen so that μ^* varied significantly from baseline: $\approx 64\%$ to $\approx 282\%$ for ortho,

and $\approx 62\%$ to $\approx 480\%$ for retro. Specifically, $M = -1000 + j * 250$ for $j \in \{1, 2, \ldots, 24\}$ for ortho, $M \in \{-5000, \ldots, 50000\}$ on a log-scale using 25 points for retro. We see in Figure 4.5D that the trend that decoding accuracies are better with no drug than with is robust.

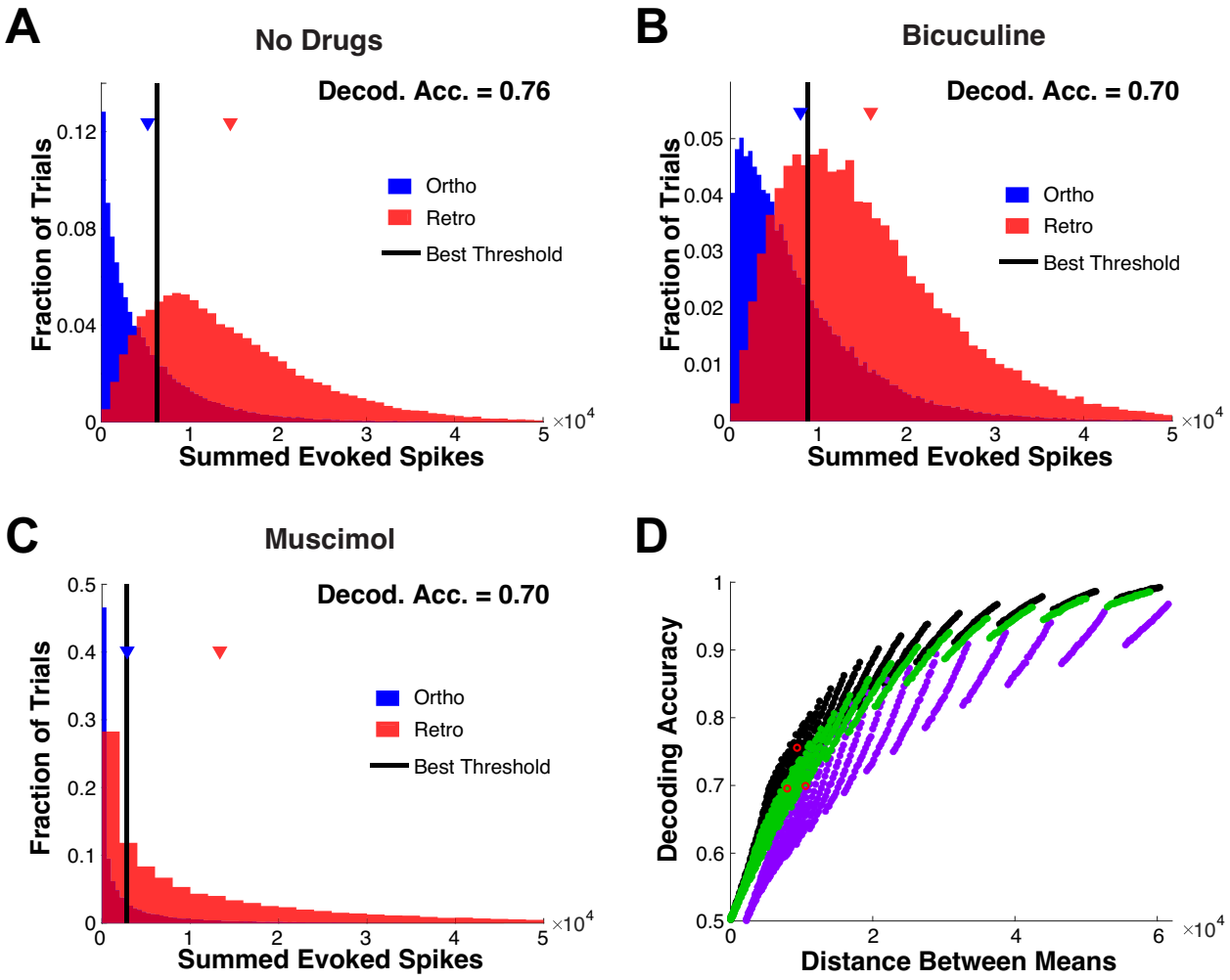

Fig. 4.5.: Decoding accuracies for simulated trial-to-trial variability by negative binomial random variable.

Example ortho versus retronasal stimulus distributions over simulated trials and noted optimal threshold (black line) with associated decoding accuracy listed for A) no drugs , B) bicuculline , and C) muscimol . D) Mapping of distance between means and decoding accuracies for each drug preparation (black - no drugs, green - bicuculline, purple - muscimol) where red dots indicate example distributions in (A)–(C). The trail of data points for each drug preparation displays behavior of decoding accuracy from the simulated negative binomial random variable output given small perturbations in the input mean firing rate.

4.3.4 Trial variability

For a more detailed understanding of the decoding accuracy dynamics, we also consider the trial-to-trial variability of spiking for each individual cell. In considering the population averaged trial variability, muscimol has the least variability followed by bicuculline and no drug (i.e., muscimol < bicuculline < no drugs) for both ortho and retro trials. The significance ($p-$values) between no drug preparation and the two inhibitory drugs are summarized in Tables 8 and 9 for ortho and retro trials, respectively, using three different statistical tests: t-test assuming unequal variances, Wilcoxon rank sum, and analysis of variances (ANOVA). For ortho stimulation, muscimol ¡ no drugs is significant for all three tests ($\alpha = 0.01$ for T-test and Wilcoxon rank sum, $\alpha = 0.05$ for ANOVA), while bicuculline ¡ no drugs is only significant by Wilcoxon rank sum. For retro, both relationships (muscimol ¡ no drug, no drug ¡ bicuculline) are significant by Wilcoxon rank sum ($\alpha = 0.05$ for bicuculline < no drugs; $\alpha = 0.01$ for muscimol < no drugs), but not significant with the other two tests.

Table 8.: Orthonasal trial significance (p-values) of trial variance differences between drugs for various statistical tests.

Relationship	T-test	Rank Sum	ANOVA
Mus < ND	0.0018	8.98e-8	0.0221
Bic < ND	0.8517	5.64e-5	0.8572

Table 9.: Retronasal trial significance (p-values) of trial variance differences between drugs for various statistical tests.

Relationship	T-test	Rank Sum	ANOVA
Mus < ND	0.0651	1.68e-4	0.1449
Bic < ND	0.4341	0.0270	0.4799

Keeping in mind the trend of trial variability in the *in vivo* data, we calculated the

variances of our simulated trials assuming a negative binomial distribution for spiking across trials. The values are listed in Table 10 and show that retronasal trial variance trends are consistent with the data (i.e., muscimol < bicuculline < no drugs) while orthonasal trial variance retains that muscimol has the least variance, but is then followed by no drugs and bicuculline (i.e., muscimol < no drugs < bicuculline). Note, these simulations are defined based on a population-averaged firing rate from the Wilson-Cowan model output, therefore, the calculated simulation trial variance is one value for each drug preparation, rather than variances over a population of individual cells. For this reason, it is not possible to calculate the significance of the differences between these variance values.

Table 10.: Calculated simulation trial variance given for different inhibitory drugs.

	Muscimol	No Drugs	Bicuculline
Orthonasal	1.75e-5	1.01e-4	1.55e-4
Retronasal	1.01e-4	0.0016	0.0015

Overall, the trial-to-trial variances between the data and simulations are consistent at times: muscimol drug preparation has both the smallest average decoding accuracy and trial variance while the no drug state has both the largest average decoding accuracy and trial variance (except in the model with ortho stimulation). Trial variability is expected to play a role in decoding accuracy differences.

4.3.5 Awake data results

Although we observe reliable encoding of ortho/retro by individual cells in our *in vivo* anesthetized rat data, it is unknown whether our results apply to awake rats. The anesthetized state provides the most controlled environment where we can set the initial odor concentrations to be the same for ortho and retro, but does not precisely capture odor processing of awake animals. For this reason, we analogously analyzed awake mice data from

Bolding & Franks [111, 112, 113] t compare with our results: can reliable encoding of ortho versus retronasal stimuli occur, and what role does inhibition play? A summary of the methodology (described in detail in Subsection 4.2.2) and results of the awake data analysis can be found in Fig 4.6.

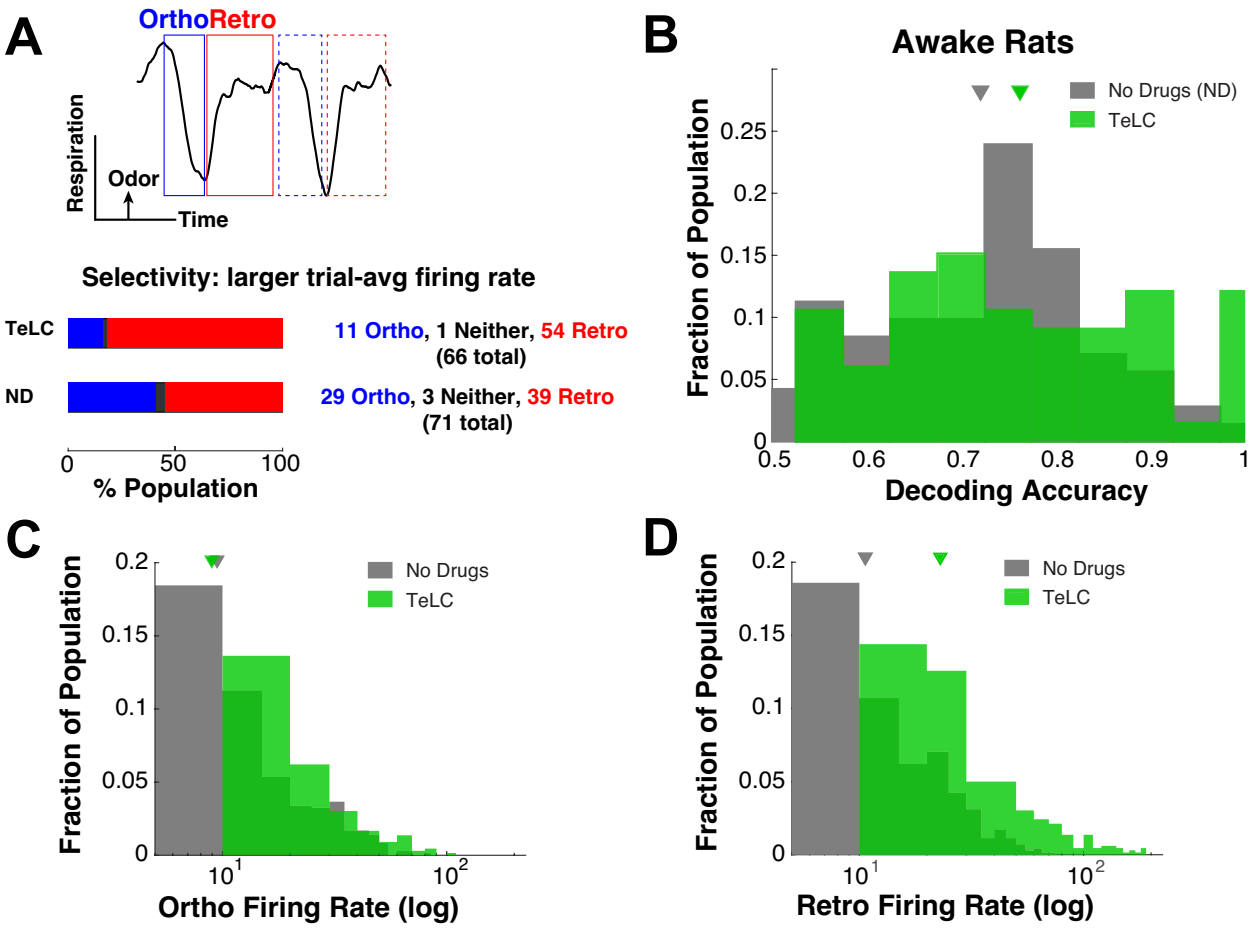

Fig. 4.6.: Methodology and summary of awake *in vivo* rat individual cell decoding accuracy using LDA.
A) Distinction of ortho (blue) versus retro (red) time bins according to breath cycle as described in Subsection 4.2.1 and proportion of cell selectivity based on larger trial-average spiking for both drug preparations. B) Histogram of individual cell trial-averaged decoding accuracies for both drug preparations where the means are denoted by triangles. C) Histogram of orthonasal firing rates ($\vec{R}_k$) used for LDA for both drug preparations where the means are denoted by triangles. D) Histogram of retronasal firing rates ($\vec{R}_k$) used for LDA for both drug preparations where the means are denoted by triangles.

Fig 4.6A summarizes the methodology used to characterize ortho and retronasal time

windows based on inhale and exhale times, respectively. Comparison of the trial-averaged firing rates $\mu_{\vec{R}_k}$ show a similar proportion of selectivity of individuals cells shown in the bottom of Fig 4.6A to the proportions anesthetized rats (Fig 4.1E) for the no drug case only; with TeLC drug (less inhibition by blocking feedback from cortex) the proportion of retro selective cells is much larger. Further, we observe that individual cells can indeed decode ortho versus retro in awake rats as shown in Fig 4.6B analogous to anesthetized rats Fig 4.1D. However, in the awake data, the average decoding accuracy is greater with drug (i.e., less inhibition) with mean decoding accuracy of 0.76 than with no drug (i.e., baseline inhibition) with mean decoding accuracy of 0.72; this is the opposite of what we observe in the anesthetized data. The significance level of this difference in decoding accuracy in the awake data based on a two-sample t-test assuming unequal variances is $p = 0.0621$.

Figs 4.6C and D acts as a comparable figure to the anesthetized state Fig 4.2B by comparing drug effects on ortho and retronasal firing rates separately. The main differentiation between the two depictions is that we analyze the population-averaged, time-varying firing rate in the anesthetized state, whereas we analyze the entire distribution of individual cell firing rates (averaged over the inhale/exhale times) in the awake state due to the highly variable and often short time windows in which ortho or retro spikes are summed over the first breath cycle. Interestingly, the opposite trend as in the anesthetized state is observed in the awake state when comparing drug effects on ortho versus retro firing rates. Specifically, retro firing rates are significantly altered (increased) with drugs whereas ortho is nearly unchanged. Note the decreased inhibition in the anesthetized data is caused by a depleted transmission capability of the synaptic connections between inhibitory GABAergic cells to MC, which differs from the awake data inhibition reduction caused by diminishing the firing of inhibitory GABAergic (granule) cells. Thus, the data may indicate varying roles of inhibition in coding ortho vs retro depending on a synaptic versus an inhibitory cell output source.

Finally, we evaluated trial variance of ortho and retro firing rates and the effects of TeLC drug. We observe a similar trend in the awake data that the TeLC drug having greater average decoding accuracy also has greater average trial variance (i.e., in anesthetized data, we find that no drug preparation has the largest average decoding accuracy as well as largest average trial variance). The significance levels of the trial variance differences using various statistical tests for the awake data are listed in Table 11. For both anesthetized and awake, the only significant difference arises with the stimulus that is most affected by inhibitory changes. In other words, the only significant difference for the anesthetized data is with orthonasal stimulus and only retronasal stimulus for the awake data both of which are the more likely to see firing rate changes given inhibitory drugs.

Table 11.: Significance ($p-$values) of trial variance differences between drug preparations in awake data using various statistical tests.

Stim Type	Relationship	T-test	Rank Sum	ANOVA
Ortho	ND < TeLC	0.5169	0.2646	0.5050
Retro	ND < TeLC	0.0082	1.41e-4	0.0054

4.4 Discussion

In this work, we show that stimulus route information is transmitted to higher brain regions by OB. Further, this work examines the circuit components that promote efficient coding of individual MCs with drug manipulations of inhibitory synapses. In our *in vivo* anesthetized rat data, we observe significantly larger average decoding accuracies for classifying ortho/retro with baseline levels of inhibition compared to less or more drug-induced inhibition. We also found that inhibitory drugs affect MC firing responses with orthonasal odor, but do not significantly change firing response with retronasal odor.

We constructed a simple firing rate model to capture the varying drug effects for ortho

versus retronasal stimulus. This model with only temporal differences of stimulus input to differentiate ortho versus retronasal stimulus captures the differing drug effects on each stimulus type. Based on intuition of how the reciprocally coupled network is structured, we hypothesized a form of plasticity existed in the MC to inhibitory population synaptic connections that weakened the inhibitory drug effects provided the longer time scales of retronasal input. Interestingly, using short-term depression in the model on the excitatory synaptic strength ($w_{E\to I}$) further distinguishes the inhibitory drug effects on ortho and retronasal response. Indeed, a review of the current literature revealed evidence of plasticity in OB circuitry [107, 109], and more specifically of short-term synaptic depression in the main OB [110] and from MC to GC [108]. However, we did not evaluate all plasticity types and did not consider existence of synaptic plasticity on the inhibitory strength ($w_{I\to E}$). This would be a fairly exhaustive search to consider all combinations of types and direction of plasticity, and it would be an important future effort to undertake as stand alone work.

Prior experiments show evidence of plasticity in OB circuitry [107, 109], and more specifically evidence of short-term synaptic depression in the main OB [110] and from MC to GC [108]. In [107], the amplitude and slope of the excitatory synaptic potentials correlate with odor concentration indicating the ability of this synapse to have different response levels based on odor information. Further, [109] found that changes in sniffing pattern with awake mice were insufficient to explain the entirety of the response changes of MC (and tufted cells). Thus, their findings indicate either top-down modulation and/or plasticity of the circuits within the OB to be critical in regulating MC/tufted cell responses. Based on our modelling, short-term synaptic depression from MC to GC specifically improved how well the model replicated differing drug effects on MC responses to ortho versus retronasal stimulus. Although [108] found forms of short-term depression from the MC to GC specifically, altogether they showed "heterogeneous" forms of short-term synaptic plasticity from the MC to GC synapse, with some depressing and some facilitating. Our work cannot defini-

tively say whether plasticity or top-down modulation drives response differences. Additional experiments and modelling efforts could further investigate these issues.

We then simulated trial-to-trial variability of spike counts with a negative binomial random variable with mean defined by the firing rate model output. This random variable model consistently captures the decoding accuracy trends given different inhibitory drugs observed in our data. Further, the calculated trial variance by negative binomial reflects the relationship of the lowest and highest average decoding accuracy aligning with the lowest and highest trial variance, respectively, that is partially consistent with our experimental data.

Finally, we applied a similar analytical methodology to awake mouse data comparing MC firing response during inhale (i.e., ortho) and exhale (i.e., retro) of first breath cycle after stimulus onset. We find robustly that individual cells are able to decode ortho and retro stimuli based on spiking information alone. Moreover, we observe that differences in inhibitory levels in the main OB cause changes in decoding accuracy and that these inhibitory changes affect one stimulus route only while not significantly affecting the other. The contrasting finding from analyzing the awake data is that changes in inhibition resulted in higher average decoding accuracy versus baseline inhibition in anesthetized, and that retro population firing response are altered with drugs (while only ortho population firing was altered with drugs in anesthetized rats).

The awake data from Bolding & Franks was used due to its availability and containing a drug preparation to alter the inhibition in the OB circuit. Although it was the most convenient option to compare with our anesthetized data, a direct comparison is not fair for the following reasons. It is well known that awake rats have much higher spontaneous MC firing ($\approx$20 Hz) [112, 67] than anesthetized rats ($\approx$5 Hz), meaning that even identically conducted experiments could have different MC responses. Also, the two sets of data did not use identical methodology, and the awake data was collected with no intention of including

analysis of retronasal odor processing [112]. We elected to characterize ortho as the inhale and retro as the exhale time window of the breath cycle based on physiological insights, but the odor was not delivered in a controlled manner to the ortho and retronasal routes, like in our anesthetized data, to ensure identical initial odor concentrations. Further, the concentration amounts used for the awake data (0.3% v/v) is less than the concentration used for the anesthetized data (1% v/v). In addition to this difference in odor concentration and presentation, the awake data considered a different source of inhibition than the anesthetized data. Although the mechanism seems similar, not that reduced inhibitory synaptic strength to MC (anesthetized data) can be different than lowering the firing rate of inhibitory neurons via blocking cortex input (awake data), especially in a reciprocally coupled network such as OB. This difference especially limits the extent by which we can compare the awake and anesthetized data results. Future studies are required to distinguish whether similar results are observed in awake and anesthetized animals and to confirm the role of inhibition in processing ortho versus retronasal stimulus.

Appendix A

ELECTROPHYSIOLOGICAL RECORDINGS

All procedures were carried out in accordance with the recommendations in the Guide for the Care and Use of Laboratory Animals of the National Institutes of Health and approved by University of Arkansas Institutional Animal Care and Use Committee (protocol #14049). Data were collected from 11 adult male rats (240-427 g; *Rattus Norvegicus*, Sprague-Dawley outbred, Harlan Laboratories, TX, USA) housed in an environment of controlled humidity (60%) and temperature (23°C) with 12h light-dark cycles. The experiments were performed in the light phase.

Surgical preparations. Anesthesia was induced with isoflurane inhalation and maintained with urethane (1.5 g/kg body weight (**bw**) dissolved in saline, intraperitoneal injection (**ip**)). Dexamethasone (2 mg/kg bw, ip) and atropine sulphate (0.4 mg/kg bw, ip) were administered before performing surgical procedures. Throughout surgery and electrophysiological recordings, core body temperature was maintained at 37°C with a thermostatically controlled heating pad. To isolate the effects of olfactory stimulation from breath-related effects, we performed a double tracheotomy surgery as described previously [6]. A Teflon tube (OD 2.1 mm, upper tracheotomy tube) was inserted 10mm into the nasopharynx through the rostral end of the tracheal cut. Another Teflon tube (OD 2.3 mm, lower tracheotomy tube) was inserted into the caudal end of the tracheal cut to allow breathing, with the breath bypassing the nasal cavity. Both tubes were fixed and sealed to the tissues using surgical thread. Local anesthetic (2% Lidocaine) was applied at all pressure points and incisions. Subsequently, a craniotomy was performed on the dorsal surface of the skull over the right

olfactory bulb (2 mm × 2 mm, centered 8.5 mm rostral to bregma and 1.5 mm lateral from midline).

Olfactory stimulation. A Teflon tube was inserted into the right nostril and the left nostril was sealed by suturing. The upper tracheotomy tube inserted into the nasopharynx was used to deliver odor stimuli retronasally. Odorized air was delivered for 1 s in duration at 1 minute intervals, with a flow rate of 250 ml/min and 1% of saturated vapor. The odorant was Ethyl Butyrate (EB). We note that the full experimental data set included additional odors, but here we consider only EB.

Electrophysiology. A 32-channel microelectrode array (MEA, A4x2tet, NeuroNexus, MI, USA) was inserted 400 μm deep from dorsal surface of OB targeting tufted and mitral cell populations. The MEA probe consisted of 4 shanks (diameter: 15 μm, inter-shank spacing: 200 μm), each with eight iridium recording sites arranged in two tetrode groups near the shank tip (inter-tetrode spacing: 150 μm, within tetrode spacing 25 μm). Simultaneous with the OB recordings, we recorded from a second MEA placed in anterior piriform cortex. Voltage was measured with respect to an AgCl ground pellet placed in the saline-soaked gel foams covering the exposed brain surface around the inserted MEAs. Voltages were digitized with 30 kHz sample rate (Cereplex + Cerebus, Blackrock Microsystems, UT, USA). Recordings were band-pass filtered between 300 and 3000Hz and semiautomatic spike sorting was performed using Klustakwik software, which is well suited to the type of electrode arrays used here [114].

Appendix B

BIOPHYSICAL OB MODEL PARAMETER DESCRIPTIONS

Table 12.: Description of biophysical OB model parameters and values.

Each of these values are the same as defined by [35, 36] with the exception of maximal conductance values which are the sum of all cell compartments (soma, dendrite, axon, etc.) as defined by [36]. Additionally, any conductance value denoted by $-$ implies that this ionic current is not included in the associated cell. All MC values listed are those used for the uncoupled MC model described in Chapter 3 with the exception that $g_{DR} = 70\,\mathrm{mS/cm^2}$ for the full OB model in Chapter 2 and in [9], but set to $g_{DR} = 15\,\mathrm{mS/cm^2}$ in Chapter 3 and in [70] as indicated in parenthesis.

Resistance and Capacitance				
Description	**Variable**	**MC Value**	**GC Value**	**PGC Value**
Membrane Resistance (KΩ-cm^2)	R_{m}	30	30	20
Membrane Capacitance (μF/cm^2)	C_{m}	1.2	2.0	1.2
Cytoplasmic (Axial) Resistance (Ω-cm)	R_{a}	70	70	80
Ionic Currents (μA/cm^2) and Maximal Conductance (mS/cm^2)				
Description	**Variable**	**MC Value**	**GC Value**	**PGC Value**
Fast, Spike-Generating Sodium Current (I_{Na})	g_{Na}	120	70	70
Persistent Sodium Current (I_{NaP})	g_{NaP}	0.42	—	—
Potassium Delayed Rectifier (I_{DR})	g_{DR}	70 (15)	25	25
Fast-Activating Transient Potassium Current (I_{A})	g_{A}	10	80	40
Noninactivating Muscarinic Potassium Current (I_{M})	g_{M}	—	0.5	1.0
Slow-Inactivating Transient Potassium Current (I_{KS})	g_{KS}	84	—	—
Hyperpolarization-Activated Current (I_{H})	g_{H}	—	—	0.2
L-type Calcium Current (I_{CaL})	g_{CaL}	0.85	—	—
High-Threshold Calcium Current ($I_{\mathrm{CaP/N}}$)	$g_{\mathrm{CaP/N}}$	—	0.2	1.0
Low-Threshold Inactivating Calcium Current (I_{CaT})	g_{CaT}	—	0.1	3.0
CA^{2+}-Activated Nonspecific Cation Current (I_{CAN})	g_{CAN}	—	1.0	—
CA^{2+}-Dependent Potassium Current (I_{KCa})	g_{KCa}	5	0.5	2.0
Reversal Potentials (mV)				
Description	**Variable**	**MC Value**	**GC Value**	**PGC Value**
Leak Current Reversal Potential	E_{L}	-60	-60	-65
Sodium Reversal Potential	E_{Na}	45		
Potassium Reversal Potential	E_{K}	-80		
Hyperpolarization-Activated Reversal Potential	E_{H}	0		
Ca^{2+}-Activated Nonspecific Cation Reversal Potential	E_{cation}	10		
Calcium Reversal Potential	E_{Ca}	$\frac{RT}{2F}\log\left(\frac{10}{[\mathrm{Ca}^{2+}]}\right)$		
Calcium Dynamics				
Description	**Variable**	**MC Value**	**GC Value**	**PGC Value**
Perimembrane Thickness (μm)	w	1	0.2	0.2
Ion Valence	z	2		
Boltzman Constant * Temperature / Faraday Constant	$\frac{RT}{F}$	26.55 mV		
Ca^{2+} Removal Rate (ms)	τ_{Ca}	10	800	800
Intracellular Ca^{2+} Concentration	$[\mathrm{Ca}^{2+}]$	dynamic		
Ca^{2+} Resting Concentration (μmol/1)	$[\mathrm{Ca}^{2+}]_{\mathrm{rest}}$	0.05		

Table 13.: Gating variable dynamics in the MC model.

Same dynamics as was used in [35], except we used a function fit for I_{DR} rather than a lookup table. When gating variables are given as X_∞ and τ_X, the equation is: $\frac{dX}{dt} = \frac{X_\infty - X}{\tau_X}$ rather than (3.3). The last column refers to the following references: [1] [115], [2] [116], [3] [117].

Ionic Current	**Gating Var**	α_x **or** x_∞	β_x **or** τ_x **(ms)**	**Source**
I_{Na}	$p = 3$	$\alpha_m = \frac{0.32(V+45)}{1-\exp(-(V+45)/4)}$	$\beta_m = \frac{-.28(V+18)}{1-\exp((V+18)/5)}$	1
	$q = 1$	$\alpha_h = \frac{.128}{\exp((V+41)/18)}$	$\beta_h = \frac{4}{1+\exp(-(V+18)/5)}$	
I_{NaP}	$p = 1$	$m_\infty = \frac{1}{1+\exp(-(V+50)/5)}$		3
I_{DR}	$p = 2$	$m_\infty = \frac{((V+100)/150)^{8.585}}{.575^{8.585}+((V+100)/150)^{8.585}}$	$\tau_m = \frac{\exp(-(V+30)/66.378)}{.27654} + \frac{2.89}{1+\exp(-(V-19.0524)/12.879)}$	1
	$q = 1$	$h_\infty = .433(1 + \tanh(-\frac{V+13.925}{13.02})) + .1337$	$\tau_h = 50$	
I_A	$p = 1$	$m_\infty = \frac{1}{1+\exp(-(V-17.5)/14)}$	$\tau_m = \frac{25\exp((V+45)/13.3)}{3.3(1+\exp((V+45)/10))}$	2
	$q = 1$	$h_\infty = \frac{1}{1+\exp((V+41.7)/6)}$	$\tau_h = \frac{55.5\exp((V+70)/5.1)}{3.3(1+\exp((V+70)/5))}$	
I_{KS}	$p = 1$	$m_\infty = \frac{1}{1+\exp(-(V+34)/6.5)}$	$\tau_m = 10$	3
	$q = 1$	$h_\infty = \frac{1}{1+\exp((V+68)/6.6)}$	$\tau_h = 200 + \frac{330}{1+\exp(-(V+71.6)/6.85)}$	
I_{CaL}	$p = 1$	$\alpha_m = \frac{7.5}{1+\exp(-(V-13)/17)}$	$\beta_m = \frac{1.65}{1+\exp(-(V-14)/4)}$	1
	$q = 1$	$\alpha_h = \frac{6.8\times10^{-3}}{1+\exp((V+30)/12)}$	$\beta_h = \frac{.06}{1+\exp(-V/11)}$	
I_{KCa}	$p = 1$	$\alpha_m = \frac{-500\exp((V-65)/27)(0.015-[\mathrm{Ca}^{2+}]}{1-\exp(-([\mathrm{Ca}^{2+}]-.015)/.0013)}$	$\beta_m = 0.05$	1

Table 14.: Gating variable dynamics in the GC and PGC model.

Same dynamics as was used in [35], except we used a function fit for I_{DR} rather than a lookup table. When gating variables are given as X_∞ and τ_X, the equation is: $\frac{dX}{dt} = \frac{X_\infty - X}{\tau_X}$ rather than (3.3). The last column refers to the following references: [1] [115], [2] [116], [3] [118], [4] [119].

Ionic Current	**Gating Var**	α_x **or** x_∞	β_x **or** τ_x **(ms)**	**Source**
I_{Na}	$p = 3$	$\alpha_m = \frac{0.4(V+25)}{1-\exp(-(V+25)/7.2)}$	$\beta_m = \frac{-0.124(V+25)}{1-\exp((V+25)/7.2)}$	2
		$m_\infty = \alpha_m/(\alpha_m + \beta_m)$	$\tau_m = \frac{1}{2.1}\max\{1/(\alpha_m + \beta_m), 0.02\}$	
	$q = 1$	$\alpha_h = \frac{0.03(V+40)}{1-\exp(-(V+40)/1.5}$	$\beta_h = \frac{-0.01(V+40)}{1-\exp((V+40)/1.5)}$	
		$h_\infty = \frac{1}{1+\exp((V+45)/4)}$	$\tau_h = \frac{1}{2.1}\max\{1/(\alpha_h + \beta_h), 0.5\}$	
I_{DR}	$p = 1$	$m_\infty = \frac{1}{1+\exp(-(V-21)/10)}$	$\tau_m = \frac{285.7\exp((V+50)/36.4)}{3.3(1+\exp((V+50)/18.2))}$	2
I_M	$p = 1$	$m_\infty = \frac{1}{1+\exp(-(V+35)/5)}$	$\tau_m = \frac{1000}{3.3\exp((V+35)/40+\exp(-(V+35)/20)}$	1
I_A	$p = 1$	$m_\infty = \frac{1}{1+\exp(-(V-7.6)/14)}$	$\tau_m = \frac{25\exp((V+45)/13.3)}{3.3(1+\exp((V+45)/10))}$	2
	$q = 1$	$h_\infty = \frac{1}{1+\exp((V+67.4)/6)}$	$\tau_h = \frac{138.8\exp((V+70)/5.1)}{3.3(1+\exp((V+70)/5))}$	
I_H	$p = 1$	$m_\infty = \frac{1}{1+\exp(-(V+80)/10)}$	$\tau_m = \frac{1176.5\exp((V+65)/23.5)}{2.1(1+\exp((V+65)/11.8))}$	4
$I_{CaP/N}$	$p = 2$	$m_\infty = \frac{1}{1+\exp(-(V+10)/4)}$	$\tau_m = 0.4 + \frac{0.7}{\exp(-(V+5)/15)+\exp((V+5)/15)}$	3
	$q = 1$	$h_\infty = \frac{1}{1+\exp((V+25)/2)}$	$\tau_h = 300 + \frac{100}{\exp(-(V+40)/9.5)+\exp((V+40/9.5)}$	
I_{CaT}	$p = 2$	$m_\infty = \frac{1}{1+\exp(-(V+44-V_a)/5.5)}$	$\tau_m = 1.5 + \frac{3.5}{\exp(-(V+30-V_a)/15+\exp((V+30-V_a)/15}$	3
	$q = 1$	$h_\infty = \frac{1}{1+\exp((V+70)/4)}$	$\tau_h = 10 + \frac{40}{\exp(-(V+50)/15)+\exp((V+50)/15)}$	
I_{CAN}	$p = 1$	$m_\infty = \frac{1}{1+\exp(-(V+43)/5.2)}$	$\tau_m = 1.6 + \frac{2.7}{\exp(-(V+55)/15+\exp((V+55)/15)}$	3
I_{KCa}	$p = 1$	See Table 13	See Table 13	1

Appendix C

CHAPTER 2 SUPPLEMENTAL MATERIAL

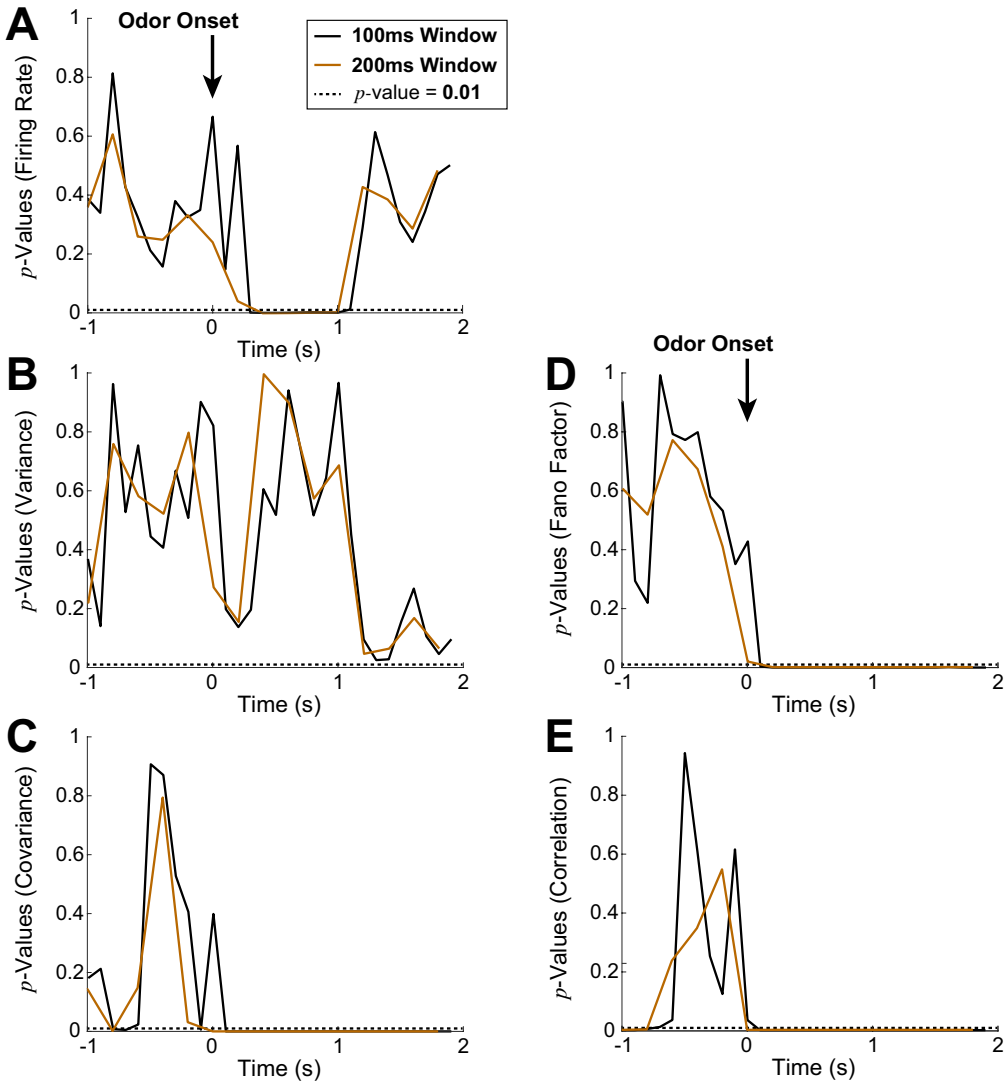

Fig. C.1.: Statistical significance of different spike count statistics from *in vivo* rat data. We performed two-sample t-tests assuming unequal variances for each point in time to assess whether the spike count statistics are significantly different with ortho and retro stimulation. We find statistical significance ($\alpha = 0.01$) between ortho and retronasal firing rate (A) after and for the duration of odor stimulation ($0.3 \leq t \leq 1\,\text{s}$ with 100 ms time windows and $0.5 \leq t \leq 1.1\,\text{s}$ with 200 ms time windows) as well as spike count covariance (C) for the entirety of the evoked state ($0 \leq t \leq 2\,\text{s}$ excluding $t = 0\,\text{s}$ with 200 ms time window). Spike count variance (B) is not found to have any statistical significant differences between ortho and retro. For completeness, significance of Fano Factor (D) and Pearson's correlation (E) are also significantly different for ortho and retro in the evoked state ($0 < t \leq 2$ s for Fano Factor and $0 \leq t \leq 2\,\text{s}$ excluding $t = 0\,\text{s}$ with 100 ms time window for correlation).

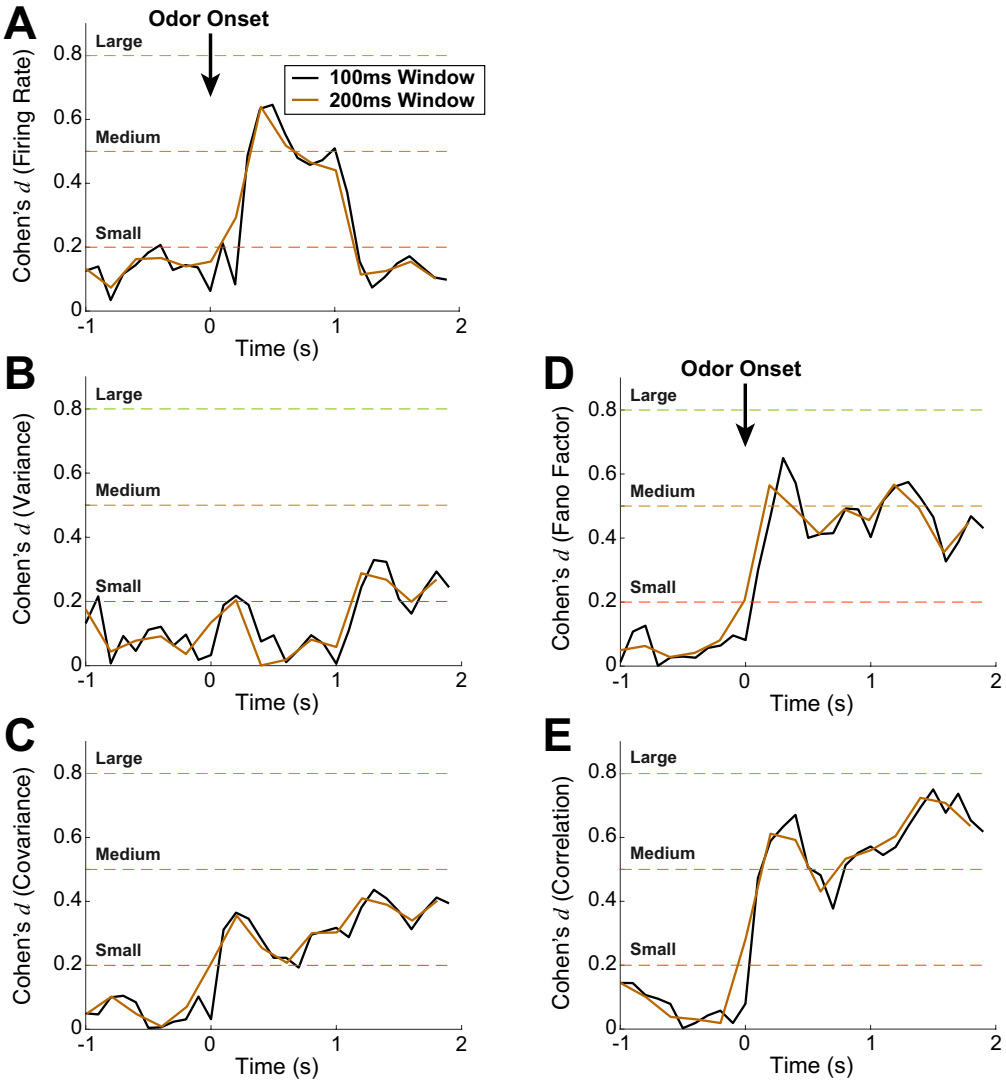

Fig. C.2.: Statistical measure of effect size using Cohen's d for *in vivo* rat data.

We calculated Cohen's d value for the nondirectional (two-tailed) case to measure effect size index for t-tests of means (see Fig C.1) in standard units. We find small ($t = 0.3$, $0.7 \leq t \leq 0.9$ s with 100 ms; $0.6 < t \leq 1$ s with 200 ms) and medium ($0.3 < t < 0.7$ s, $t = 1$ s with 100 ms; $0.4 \leq t \leq 0.6$ s with 200 ms) effect size of statistical significance between ortho and retronasal firing rate (A) as well as small ($0 \leq t \leq 2$ s excluding $t = 0$ s with 200 ms time windows) effect size of spike count covariance (C). Spike count variance (B) does not have a measure of effect size since it is not found to have any statistical significant differences between ortho and retro. For completeness, effect size of Fano Factor (D) and Pearson's correlation (E) are also found to be small ($0 < t \leq 0.2$ s $\cup$ $0.4 < t \leq 1$ $\cup$ $1.4 < t \leq 2$ s for Fano Factor, and $0 \leq t < 0.2$ $\cup$ $0.5 < t < 0.8$ excluding $t = 0$ s with 100 ms time windows for correlation) and medium ($0.2 < t \leq 0.4$ $\cup$ $1 < t \leq 1.4$ s for Fano Factor and $0.2 \leq t \leq 0.5$ $\cup$ $0.8 \leq t \leq 2$ s for correlation).

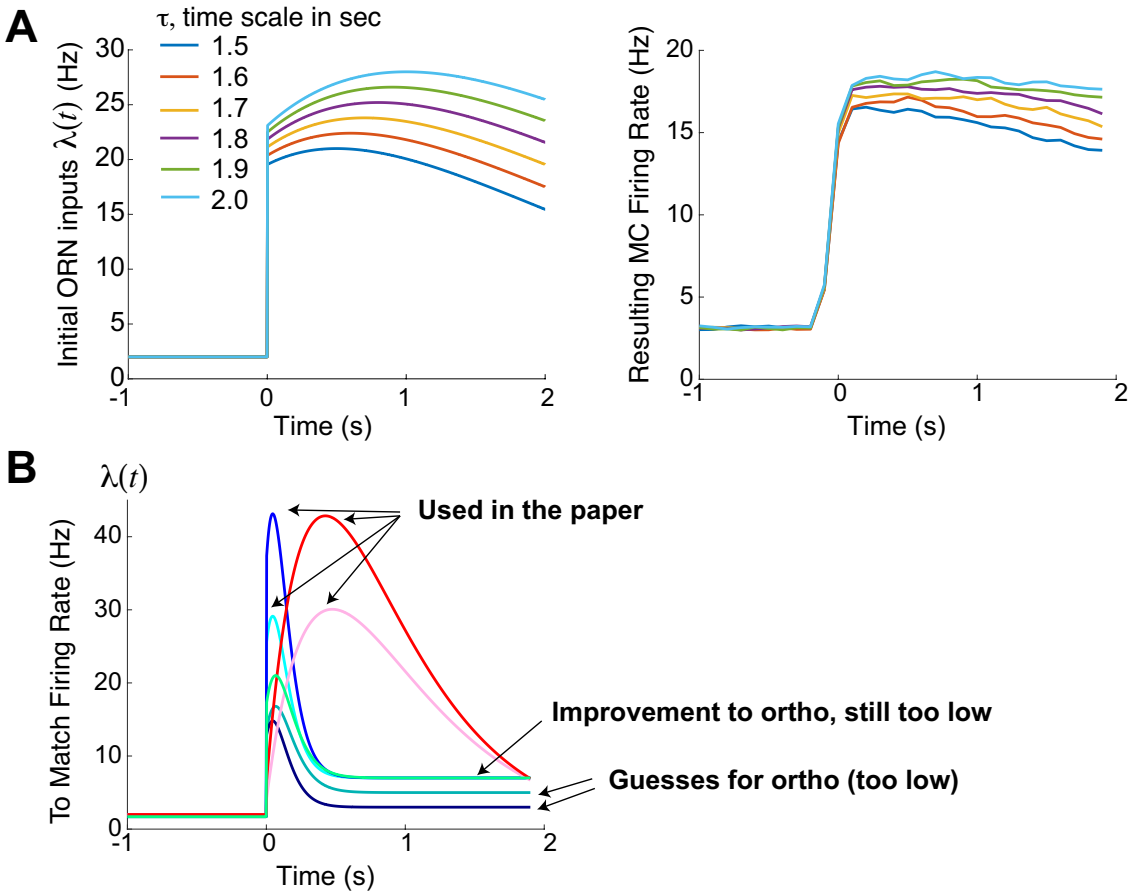

Fig. C.3.: Details of various ORN input rates we surveyed $\lambda(t)$ for OB model.

Various ORN input rates surveyed achieved via trial and error. A) Left: initial set of ORN inputs $\lambda(t)$ (with evoked $\lambda(t) = (t+1)e^{-(t+1)/\tau}$) we surveyed to better understand the MC firing rate (right), calculated with 2,000 realizations. B) Fitting the ortho firing rate well enough required considering many $\lambda_O(t)$, and we even shifted the spontaneous input rate up slightly at some point. However, the only 2 retro inputs we tried (pink and red) were relatively accurate.

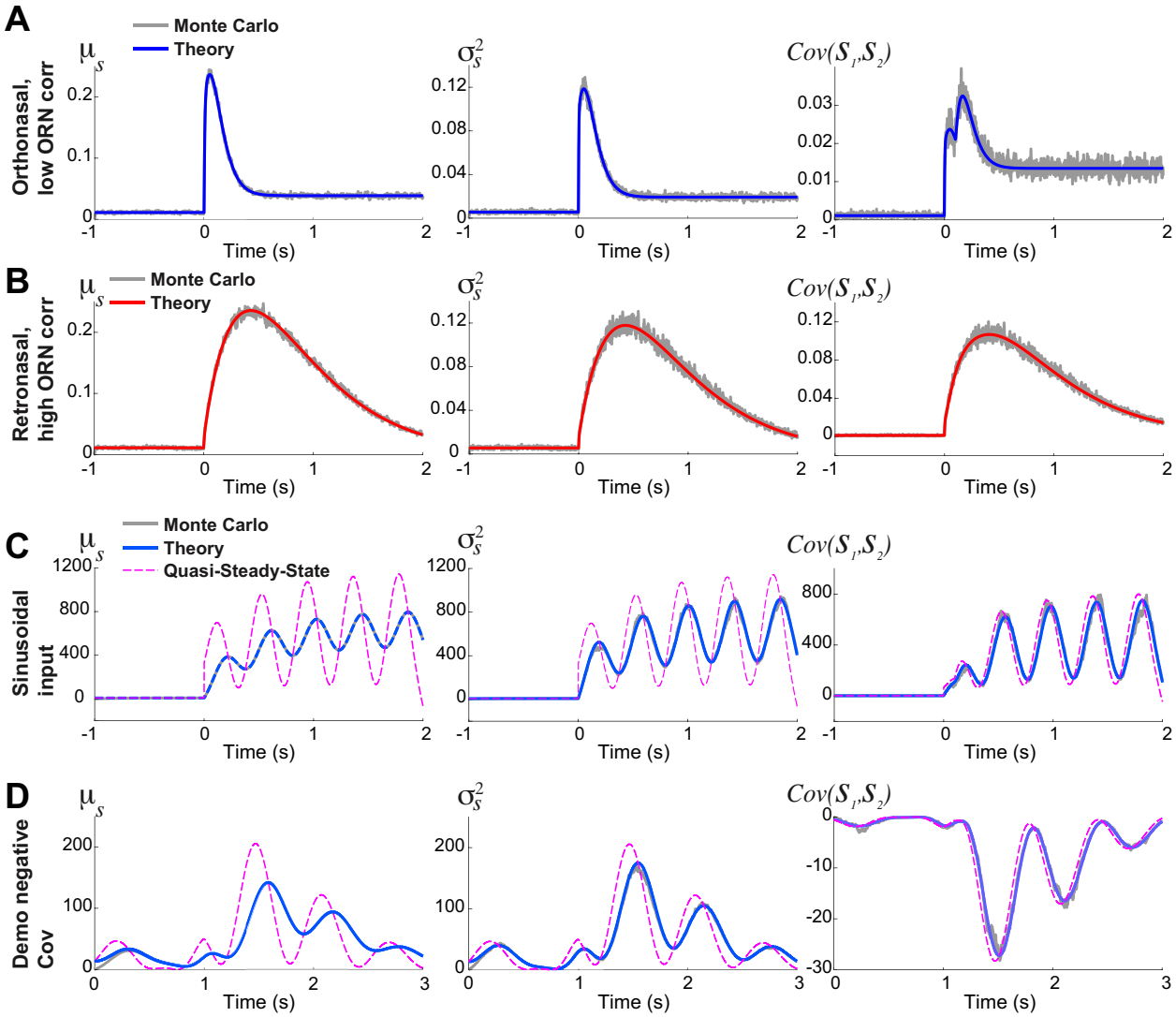

Fig. C.4.: Example of theoretical statistic calculation for ORN synapse compared to Monte-Carlo simulation of true statistic from OB model.

Our theory for the ORN synaptic input statistics (Eqs (2.8), (2.13), (2.17)) is accurate for time-varying inhomogeneous Poisson process rates and time-varying input correlation. A) Ortho-like input (fast rise and decay of Poisson rate) with same amplitude as retro (high), but with low input correlation used to capture data. Notice how the theory captures the fine structure of the covariance (double-hump). B) Retro-like input (slow rise and decay) with same amplitude as ortho (high), but with high input correlation used to capture data. C, D) Demonstrating accuracy of dynamic theory with much slower (unrealistic) time-scales: $\tau_1 = 50\,\text{ms}$ and $\tau_2 = 100\,\text{ms}$ and faster relative change in Poisson rate (all with low input correlation). Showing the quasi-steady-state approximation (Eqs (2.18) – (2.20)) in magenta. **C)** Sinusoidal input and time-varying amplitude: evoked $\lambda(t) = 0.2 + 0.8(1 - 0.8\sin(-15t))(1 - e^{-2t})$, with synapse jump sizes $a_1 = 2$, $a_2 = 5$. D) Here the jump sizes have opposite signs to get negative covariances: $a_1 = 2$, $a_2 = -1$, with $\lambda(t) = 2(t + 2.25)^2 * (1 - 0.9\sin(10t))e^{-|t-1|/0.35}$. Gray curves (Monte Carlo) are much harder to see in C,D than in A,B because of the much larger magnitudes.

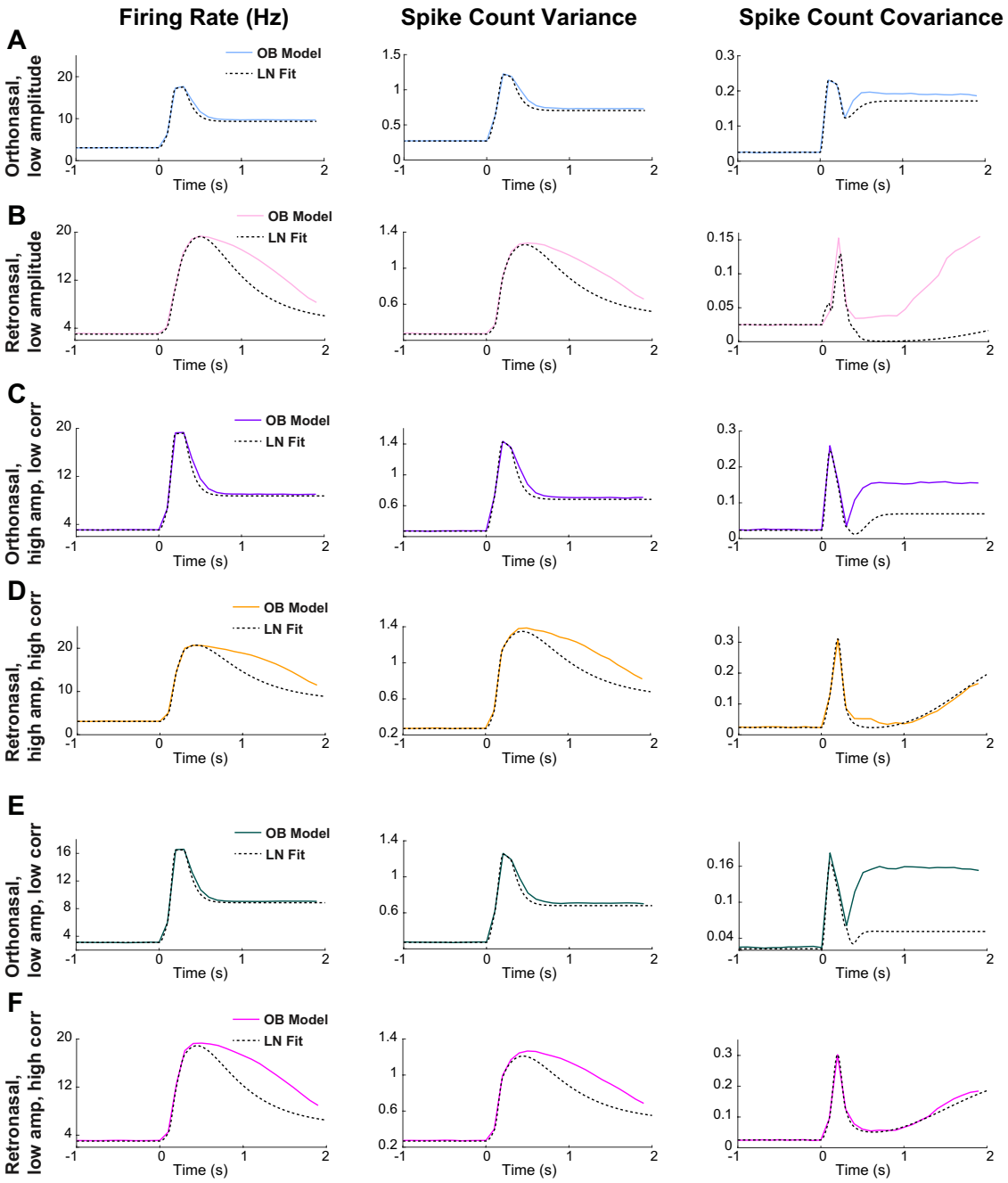

Fig. C.5.: The LN fits to the OB model statistics are good overall.

We consider 8 total different combinations of ORN inputs varying: temporal profile, amplitude height, input correlation (2 ways each). Despite the simplistic LN model, the resulting fits to the OB model are generally very good. The only exceptions are when the input correlation is relatively smaller, in which case the LN model does not accurately capture the evoked spike count covariance after several hundred milliseconds.

Appendix D

CHAPTER 3 SUPPLEMENTAL MATERIAL

D.1 Viability of alternative approaches

A common approach to reduce the number of state variables in describing (regular) spiking is to apply a phase reduction, which seems appealing because the results hold for relatively weak noise forcing where firing rates do not vary much. This motivated us to analyze the bifurcation between quiescence and spiking (using XPP–AUTO [120, 121]), in the noiseless case (Fig D.1a). We see that the stable rest state loses stability via a saddle-node on invariant circle (**SNIC**) bifurcation as the applied current increases. However, we do not find actual periodic solutions for relevant firing rates with which to calculate commonly used entities for analysis like the Phase-Resetting Curve (**PRC**). Curiously, the bifurcation diagram shows stable period solutions (green dots) that are interlaced with unstable periodic solutions. Fig D.1b shows that even with $I_{\text{app}} = 144\,\mu\text{A/cm}^2$ where the diagram (Fig D.1a) suggests there is a well-behaved periodic solution, the voltage (and other variables) are not strictly periodic. Note that with $I = 144$, the firing rates are large (91.13 Hz) and not physiologically relevant. Also, for $I = 144$ although the PRC is numerically calculable (Fig D.1c), the rather large negative region does not resemble canonical PRCs associated with a SNIC [122, 123].

Note that in a standard phase reduced scalar model [71]:

$$\frac{d\Theta}{dt} = \omega + \frac{\sigma^2}{2}\Delta'(\Theta)\Delta(\Theta) + \sigma\Delta(\Theta)\xi(t) \tag{D.1}$$

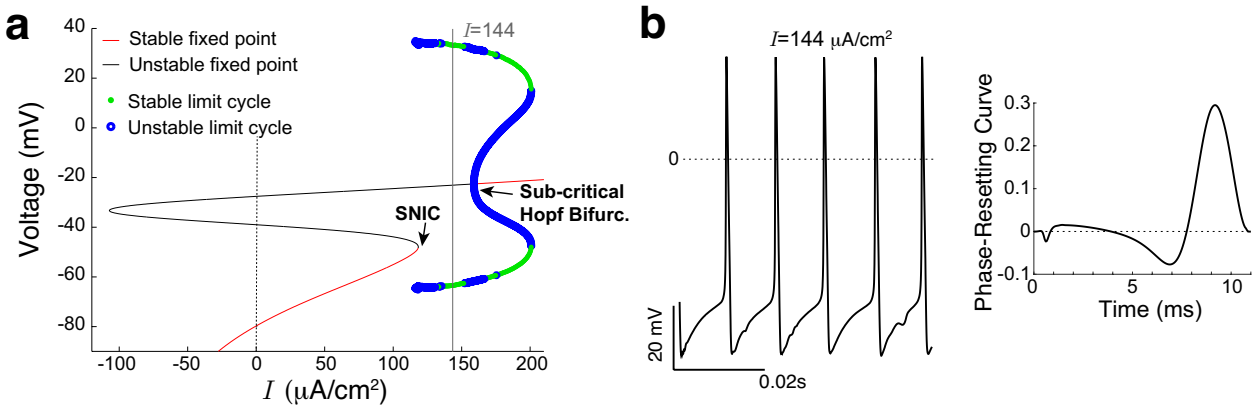

Fig. D.1.: Dynamics of noiseless MC model: phase reduction assumptions violated. a) Bifurcation diagram of voltage varying I shows SNIC at onset of spiking. b) The voltage traces in Fig3.2a are not strictly periodic, even for an ideal well-behaved I value. For unrealistically high firing rates ($I = 144\,\mu\text{A/cm}^2$, firing rate: 91.13 Hz), we see the system is not periodic despite the bifurcation diagram suggesting it should be. The infinitesimal Phase-resetting curve can be numerically calculated with XPP [120]; notice that the negative region is rather large, not resembling canonical PRCs synonymous with a SNIC [122, 123]. This all suggests phase reduction descriptions would likely be inadequate to capture the observed phenomena in the regimes we are interested in (i.e., smaller I with physiological firing rates).

the ISI density can be approximated (assuming weak noise) via [90]:

$$f_{ISI}(t) \approx \frac{1}{\sigma\sqrt{2\pi\int_0^t \Delta^2(s)\,ds}} \exp\left(-\frac{\left(t-\frac{1}{\omega}+\frac{\sigma^2\Delta^2(t)}{4}\right)^2}{2\sigma^2\int_0^t \Delta^2(s)\,dx}\right). \tag{D.2}$$

Since the formula closely resembles a normal distribution, the σ_{ISI} generally increases as $\sigma \nearrow$. Even though there is multiplicative noise: $\sigma\Delta(\Theta)$, these models would not help describe observations in Fig 3.3.

Another common approach to model analysis with weak noise is use a potential well: $\frac{dV}{dt} = -U'(V) + \sigma\xi(t)$, where U is the potential function, either principally derived from the system (simple) or ad-hoc (high-dimensional). E.g., for the leaky-integrate-and-fire model, $U(V) \propto \frac{1}{2}(V - V_L)^2$ and V has a stable fixed point at the global minimum $V = V_L$. This approach was pioneered in physics by [100] and has been applied to several neural models where "exiting" from the potential well from crossing a threshold is spiking. The rate of

spiking is often $\propto e^{-U/\sigma^2}$, which is not directly related to spiking variability. The signal–to–noise ratio (**SNR**) in these systems, and in other applications of stochastic resonance, often have a maximal SNR value for an intermediate level of noise [101]. However, this dynamic is associated with a minimum variability value in the denominator (ignoring the dynamics of the signal in the numerator) of SNR, rather than a maximal spiking variability for intermediate input noise level, as we have observed in the MC model.

Whether the potential well or "Arrhenius escape" approach by [79] for a low-dimensional Fitzhugh-Nagumo model (with 1 activity variable x and a set of identical adaptation variables H endowed with multiple time-scales that depend on x) could be successfully applied to our MC model is an open question. [79] exploited a separation of time scales, the slow variable was fixed and the mean first passage time (or escape) T could be calculated (in the fast variable) and set to the inverse of the mean firing rate: $\lambda(H(t)) = 1/T(H(t))$. The ISI density is approximated with:

$$\rho(t) = \lambda(H(t))e^{-\int_0^t \lambda(H(t'))\,dt'}$$

we see how the slow variation in H affects $\rho(t)$. This framework successfully described the non-monotonic spiking dynamics (in the CV at least) in their model. As previously mentioned in the Discussion 3.4, an analogous approach would require identifying all of the effective time-scales in our 13 variable model *and* having a significant separation of time-scales when the neuron is excitable. Even if the slow variables are frozen, one would still have to calculate the mean first passage time with the remaining fast variables, which is generally not feasible unless the resulting dimension is small. Solving for the mean first passage time requires solving an ODE system derived from the backward Fokker-Planck equation, a PDE with the number of dimensions equal to the number of state variables [81, 80]. The viability and the accuracy of this approach for capturing our results is an open question but beyond the scope of this current study.

D.2 Other spike statistics

We have focused on the ISI distribution, but there are other commonly used entities to characterize neural spike trains. For instance, the autocorrelation function (ACF) and power spectrum (P), defined below, are commonly used and can be unrelated to the ISI, in particular when the system does not reset after a spike. Letting $R(t)$ denote the spike train consisting of 0's and 1's, the (normalized) autocorrelation function is:

$$ACF(\tau) = \Big(\mathbb{E}_t\left[R(t+\tau)R(\tau)\right] - \mathbb{E}_t[R(t)]^2\Big) \Big/ ACF(0) \tag{D.3}$$

and the power spectrum:

$$P(\omega) = \Big(\Big| \int ACF(t) e^{-i2\pi\omega t}\, dt \Big|^2\Big) \Big/ P(0) \tag{D.4}$$

Fig D.2 shows these entities for the biophysical MC model with various applied current and input noise values.

With $I = 120\,\mu\text{A/cm}^2$, $ACF(\tau)$ is relatively flat for these input noise values, while $P(\omega)$ changes from having peaks at regularly spaced intervals with no noise (black) to being relatively flat with $\tilde{\sigma} > 0$. With $I = 130\,\mu\text{A/cm}^2$, $ACF(\tau)$ has local maximas at irregularly spaced τ with no noise (black) that flatten out as input noise increases; the $P(\omega)$ is similar to $I = 120, \mu\text{A/cm}^2$ but the curves have smaller values compared to $I = 120$. With $I = 140\,\mu\text{A/cm}^2$, $ACF(\tau)$ indicates relatively regular spiking, although increased input noise shifts and broadens the peaks (same for $P(\omega)$). The flatter ACF with $I = 120$ compared to larger I indicates that the spiking has less temporal regularity, which is not surprising. For a given value of I (i.e., a row in Fig D.2), increasing input noise flattens the $ACF(\tau)$ and shifts and/or diminishes peaks (local max), and for $P(\omega)$ input noise can broaden/shift/diminish peaks. Overall, the effects of input noise are nonlinear and highly dependent on I.

The ACF and P were plotted using built-in functions in MATLAB, and there appears

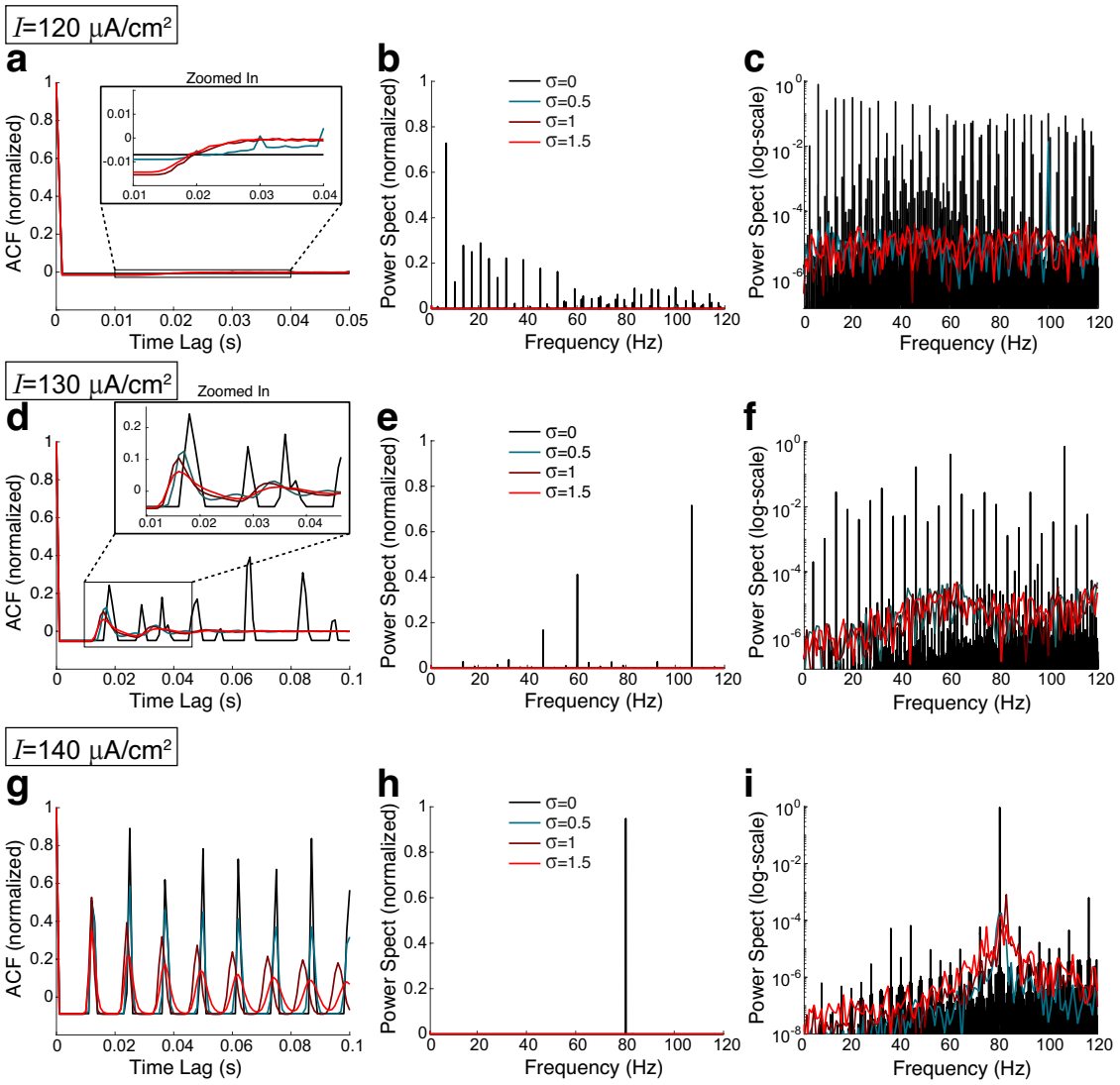

Fig. D.2.: The autocorrelation function (Eq (D.3)) and power spectrum (Eq (D.4)) of the MC model.

Three values of input current: $I = 120\,\mu\text{A/cm}^2$ in a)–c), $I = 130\,\mu\text{A/cm}^2$ in d)–f), $I = 140\,\mu\text{A/cm}^2$ in g)–i), with each panel showing the effects of increasing input noise $\tilde{\sigma}$. The effects of input noise are nonlinear and highly dependent on I.

to be slight numerical round-off errors in the ACF, e.g., between the peaks in Fig D.2g, $ACF \approx 0$, and likely in the P. Nevertheless, these plots given insight to some dynamics of the various spike trains.

Appendix E

CHAPTER 4 SUPPLEMENTAL MATERIAL

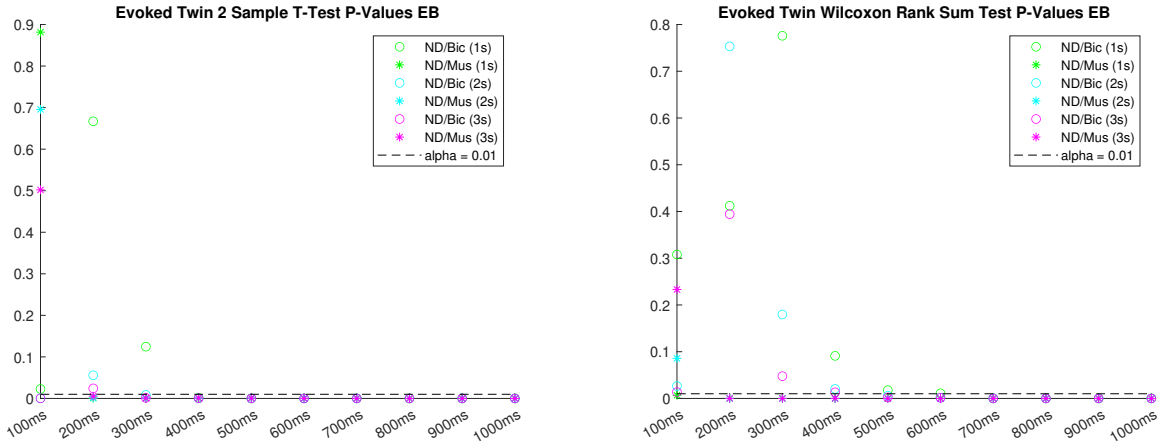

(a) Two Sample T-test

(b) Wilcoxon Rank-Sum Test

Fig. E.1.: EB food odor provides consistently significant differences between drug preparations.

Evoked state time window p-values of net decoding accuracies with different drug preparations for EB (food odor) using two different statistical tests. Dot points indicate no drug and bicuculline comparison, asterisk points indicate no drug and muscimol comparison while colors denote amount of spontaneous state time included (green = 1 s, cyan = 2 s, and magenta = 3 s). (a) Using 2 sample t-test, net decoding accuracy is significantly different ($\alpha = 0.01$, denoted by dashed black line) between no drug and muscimol for all spontaneous times when evoked time window ≥ 200 ms. Net decoding accuracy for no drug and bicuculline is significantly different for all spontaneous times when evoked time window ≥ 400 ms. Other time windows for either drug combinations are inconsistent with significance based on different spontaneous times. (b) Using Wilcoxon rank-sum test, net decoding accuracy is significantly different ($\alpha = 0.01$) between no drug and muscimol for all spontaneous times when evoked time window ≥ 200 ms. Net decoding accuracy for no drug and bicuculline is significantly different for all spontaneous times when evoked time window ≥ 700 ms. Other time windows for either drug combinations are inconsistent with significance based on different spontaneous times.

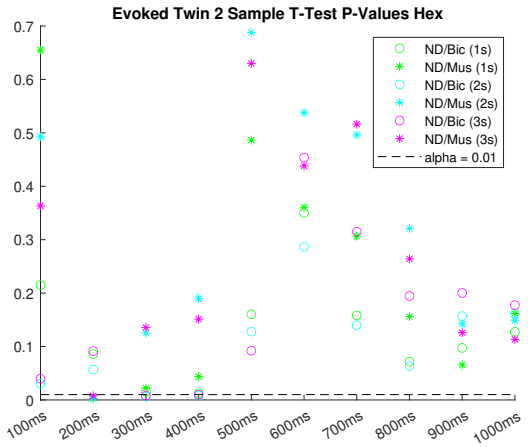

(a) Two Sample T-test

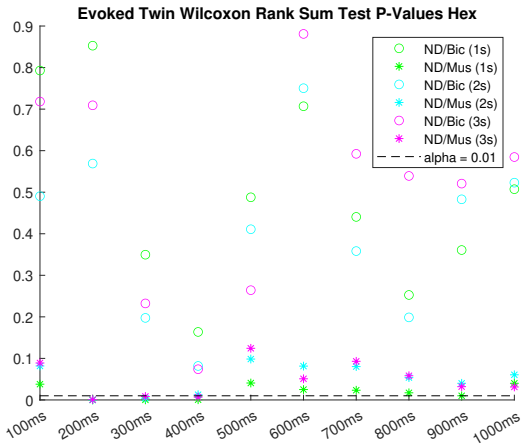

(b) Wilcoxon Rank-Sum Test

Fig. E.2.: Hex nonfood odor does not provide consistently significant differences between drug preparations.

Evoked state time window p-values of net decoding accuracies with different drug preparations for EB (food odor) using two different statistical tests. Dot points indicate no drug and bicuculline comparison, asterisk points indicate no drug and muscimol comparison while colors denote amount of spontaneous state time included (green = 1 s, cyan = 2 s, and magenta = 3 s). (a) Using 2 sample t-test, net decoding accuracy is significantly different ($\alpha = 0.01$, denoted by dashed black line) between no drug and muscimol for all spontaneous state times with evoked time window of 200 ms. Net decoding accuracy for no drug and bicuculline is significantly different for 300 ms and 400 ms evoked time window with 2 s and 3 s spontaneous state. Otherwise, there is no significant difference between no drug and bicuculline for $\alpha = 0.01$. If $\alpha = 00.05$ is considered, then this difference is significant with all spontaneous state times for evoked time windows of 300 ms and 400 ms. (b) Using Wilcoxon rank-sum test, net decoding accuracy is significantly different ($\alpha = 0.01$) between no drug and muscimol for all spontaneous state times with evoked time window of 200 ms, 300 ms and 400 ms. Net decoding accuracy for no drug and bicuculline is not significantly different for any spontaneous state times or evoked time windows, even if considering $\alpha = 0.05$.

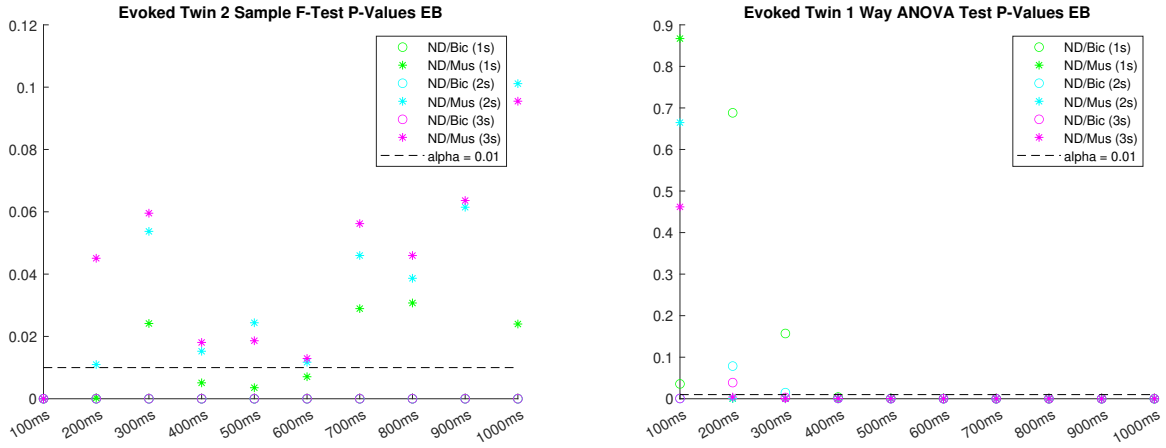

(a) Two Sample F-test

(b) One-Way ANOVA Test

Fig. E.3.: Additional statistical tests for variances for EB food odor.

Evoked state time window p-values of net decoding accuracies with different drug preparations for EB (food odor) using two different statistical tests of variances. Dot points indicate no drug and bicuculline comparison, asterisk points indicate no drug and muscimol comparison while colors denote amount of spontaneous state time included (green = 1 s, cyan = 2 s, and magenta = 3 s). (a) Using 2 sample F-test of unequal variances, net decoding accuracy is significantly different ($\alpha = 0.01$, denoted by dashed black line) between no drug and bicuculline for all evoked and spontaneous time windows. Net decoding accuracy between no drug and muscimol is significantly different ($\alpha = 0.01$) only for 1s spontaneous time window when evoke time window is $\in [400\text{ms}, 500\text{ms}, 600\text{ms}]$. Although, all other p-values are ≤ 0.11 between no drug and muscimol net decoding accuracy with most below 0.08. (b) Using 1-way ANOVA test, net decoding accuracy is significantly different ($\alpha = 0.01$) between no drug and bicuculline for all spontaneous time windows when evoked time window is ≥ 400ms. Net decoding accuracy between no drug and muscimol is significantly different ($\alpha = 0.01$) for all spontaneoues time windows when evoked time window is ≥ 200ms.

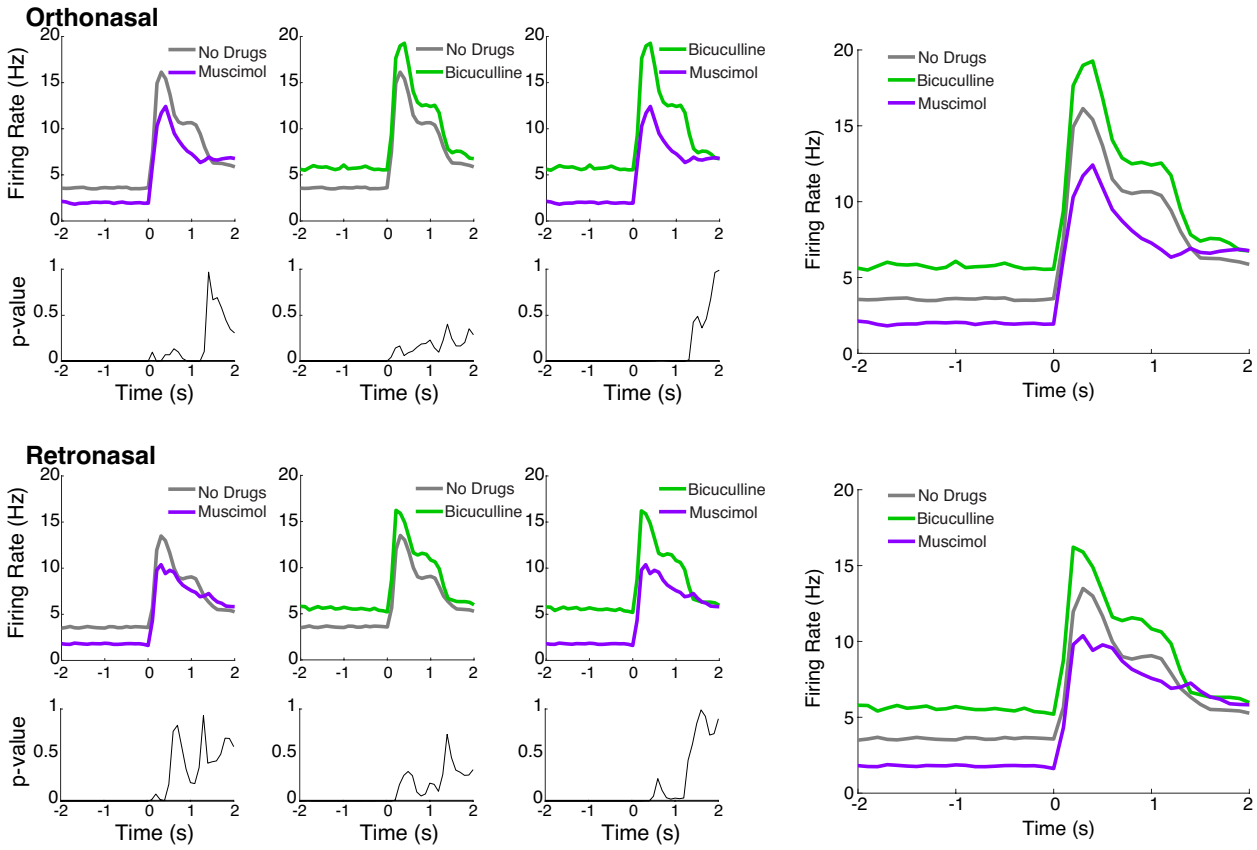

Fig. E.4.: Population firing rates of anesthetized *in vivo* rat data comparing inhibitory drug effects for both stimulus types given Hex odor.
Firing rates and respective two-sample T-test p-values for orthonasal (top) and retronasal (bottom) stimulus comparing drug combinations (left - no drug/muscimol, center left - no drug/bicuculline, center right - bicuculline/muscimol). Far right image shows overlay of all drug preparation firing rates given orthonasal (top) and retronasal (bottom) stimulus.

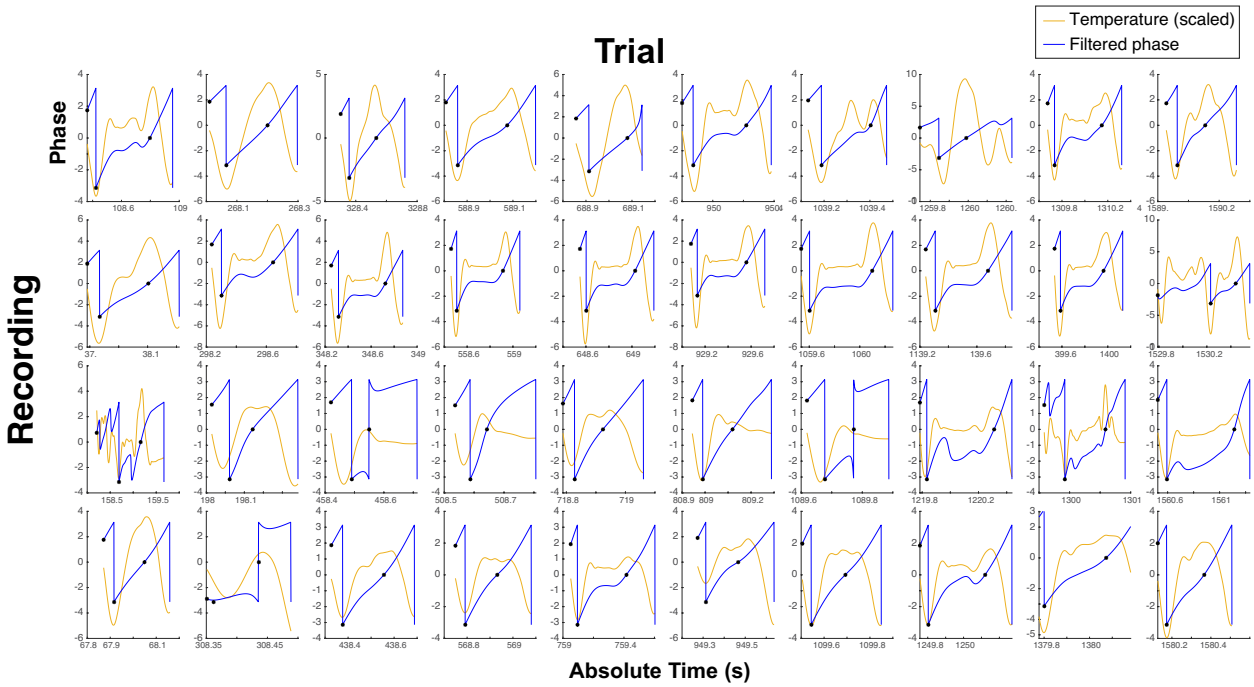

Fig. E.5.: Breath cycles used for awake data analysis.

For each trial (n =10, rows) and each experiment recording (n =4, columns), the first breath cycle immediately after odor stimulus is shown. The original measurement of air flow from [111] is shown over absolute time (s) in orange while the filtered phase used to determine breath cycle for inhale and exhale time windows is shown in blue. Additionally, the stimulus onset (start time of inhale for all trials and recordings), phase switch (end of inhale and beginning of exhale), and end of exhale are shown in consecutively placed asterisks ($*$) over time in each plot.

REFERENCES

[1] Viola Bojanowski and Thomas Hummel. "Retronasal perception of odors". In: *Physiology and Behavior* 107.4 (2012), pp. 484–487.

[2] Dana M. Small et al. "Differential neural responses evoked by orthonasal versus retronasal odorant perception in humans". In: *Neuron* 47.4 (2005), pp. 593–605. ISSN: 08966273. DOI: 10.1016/j.neuron.2005.07.022.

[3] Genevieve Bender et al. "Separate signals for orthonasal vs. retronasal perception of food but not nonfood odors". In: *Behavioral neuroscience* 123.3 (2009), p. 481.

[4] Alan R Hirsch. *Nutrition and Sensation*. CRC Press, 2022.

[5] Shree Hari Gautam et al. "Maximizing sensory dynamic range by tuning the cortical state to criticality". In: *PLoS Computational Biology* 11.12 (2015), e1004576.

[6] Shree Hari Gautam and Justus V Verhagen. "Retronasal odor representations in the dorsal olfactory bulb of rats". In: *The Journal of Neuroscience* 32.23 (2012), pp. 7949–7959.

[7] Shree Hari Gautam and Justus V Verhagen. "Direct behavioral evidence for retronasal olfaction in rats". In: *PloS one* 7.9 (2012), e44781.

[8] Rui Ni et al. "Optimal directional volatile transport in retronasal olfaction". In: *Proceedings of the National Academy of Sciences of the United States of America* 112.47 (2015), pp. 14700–14704.

[9] M.F. Craft et al. "Differences in olfactory bulb mitral cell spiking with ortho- and retronasal stimulation revealed by data-driven models". In: *PLoS Computational Biology* 17.9 (2021), e1009169. DOI: 10.1371/journal.pcbi.1009169. URL: https:

//journals.plos.org/ploscompbiol/article?id=10.1371/journal.pcbi.1009169.

[10] Nelika K Hughes, Catherine J Price, and Peter B Banks. "Predators are attracted to the olfactory signals of prey". In: *PLoS One* 5.9 (2010), e13114.

[11] Ashiq Hussain et al. "High-affinity olfactory receptor for the death-associated odor cadaverine". In: *Proceedings of the National Academy of Sciences* 110.48 (2013), pp. 19579–19584.

[12] Shree Hari Gautam and Justus V Verhagen. "Evidence that the sweetness of odors depends on experience in rats". In: *Chemical senses* 35.9 (2010), pp. 767–776.

[13] Claire Murphy and William S Cain. "Taste and olfaction: independence vs interaction". In: *Physiology & Behavior* 24.3 (1980), pp. 601–605.

[14] Claire Murphy, William S Cain, and Linda M Bartoshuk. "Mutual action of taste and olfaction." In: *Sensory processes* (1977).

[15] Debra Ann Fadool, Kristal Tucker, and Paola Pedarzani. "Mitral cells of the olfactory bulb perform metabolic sensing and are disrupted by obesity at the level of the Kv1. 3 ion channel". In: *PloS one* 6.9 (2011), e24921.

[16] Pascaline Aimé et al. "Modulation of olfactory sensitivity and glucose-sensing by the feeding state in obese Zucker rats". In: *Frontiers in Behavioral Neuroscience* 8 (2014), p. 326.

[17] Nicolas Thiebaud et al. "Hyperlipidemic diet causes loss of olfactory sensory neurons, reduces olfactory discrimination, and disrupts odor-reversal learning". In: *Journal of neuroscience* 34.20 (2014), pp. 6970–6984.

[18] Mackenzie E Hannum, Jenna A Fryer, and Christopher T Simons. "Non-food odors and the Duality of Smell: Impact of odorant delivery pathway and labeling convention on olfactory perception". In: *Physiology & Behavior* 238 (2021), p. 113480.

[19] Adam Kohn et al. "Correlations and Neuronal Population Information". In: *Annual review of neuroscience* 39.0 (2016).

[20] Rubén Moreno-Bote et al. "Information-limiting correlations". In: *Nature neuroscience* 17.10 (2014), pp. 1410–1417.

[21] B.B. Averbeck, P.E. Latham, and A. Pouget. "Neural correlations, population coding and computation". In: *Nature Reviews Neuroscience* 7 (2006), pp. 358–366.

[22] P. Dayan and L.F. Abbott. *Theoretical neuroscience: Computational and mathematical modeling of neural systems*. Taylor & Francis, 2001.

[23] Basavaraju G Sanganahalli et al. "Orthonasal versus retronasal glomerular activity in rat olfactory bulb by fMRI". In: *NeuroImage* 212 (2020).

[24] Yuichi Furudono, Ginny Cruz, and Graeme Lowe. "Glomerular input patterns in the mouse olfactory bulb evoked by retronasal odor stimuli". In: *BMC neuroscience* 14.1 (2013), p. 45.

[25] Hartwig Spors et al. "Temporal dynamics and latency patterns of receptor neuron input to the olfactory bulb". In: *Journal of Neuroscience* 26.4 (2006), pp. 1247–1259.

[26] John W Scott et al. "Responses of the rat olfactory epithelium to retronasal air flow". In: *Journal of neurophysiology* 97.3 (2007), pp. 1941–1950.

[27] Ryan M Carey et al. "Temporal structure of receptor neuron input to the olfactory bulb imaged in behaving rats". In: *Journal of neurophysiology* 101.2 (2009), pp. 1073–1088.

[28] David PA Schulz, Maneesh Sahani, and Matteo Carandini. "Five key factors determining pairwise correlations in visual cortex". In: *Journal of neurophysiology* 114.2 (2015), pp. 1022–1033.

[29] S. Ostojic, N. Brunel, and V. Hakim. "How connectivity, background activity, and synaptic properties shape the cross-correlation between spike trains". In: *The Journal of Neuroscience* 29 (2009), pp. 10234–10253.

[30] A.K. Barreiro and C. Ly. "When do correlations increase with firing rates in recurrent networks?" In: *PLoS Computational Biology* 13 (2017), e1005506. DOI: 10.1371/journal.pcbi.1005506.

[31] A. Barreiro and C. Ly. "Investigating the correlation-firing rate relationship in heterogeneous recurrent networks". In: *Journal of Mathematical Neuroscience* 8 (2018), p. 8. DOI: 10.1186/s13408-018-0063-y.

[32] Wilfrid Rall et al. "Dendrodendritic synaptic pathway for inhibition in the olfactory bulb". In: *Experimental neurology* 14.1 (1966), pp. 44–56.

[33] Nathan E Schoppa and Nathan N Urban. "Dendritic processing within olfactory bulb circuits". In: *Trends in neurosciences* 26.9 (2003), pp. 501–506.

[34] Patricia Duchamp-Viret et al. "Patterns of spontaneous activity in single rat olfactory receptor neurons are different in normally breathing and tracheotomized animals". In: *Journal of Neurobiology* 65.2 (2005), pp. 97–114.

[35] Guoshi Li and Thomas A Cleland. "A two-layer biophysical model of cholinergic neuromodulation in olfactory bulb". In: *Journal of Neuroscience* 33.7 (2013), pp. 3037–3058.

[36] Guoshi Li and Thomas A Cleland. "A coupled-oscillator model of olfactory bulb gamma oscillations". In: *PLoS computational biology* 13.11 (2017), e1005760.

[37] Cheng Ly et al. “Odor-evoked increases in olfactory bulb mitral cell spiking variability”. In: *iScience* 24.9 (2021), p. 102946.

[38] Hokto Kazama and Rachel I Wilson. “Origins of correlated activity in an olfactory circuit”. In: *Nature neuroscience* 12.9 (2009), p. 1136.

[39] Sashi Marella and Bard Ermentrout. “Amplification of asynchronous inhibition-mediated synchronization by feedback in recurrent networks”. In: *PLoS Computational Biology* 6.2 (2010), e1000679.

[40] Srdjan Ostojic and Nicolas Brunel. “From spiking neuron models to linear-nonlinear models”. In: *PLoS Computational Biology* 7.1 (2011), e1001056.

[41] Eero P Simoncelli et al. “Characterization of neural responses with stochastic stimuli”. In: *The cognitive neurosciences* 3.327-338 (2004), p. 1.

[42] Hiroko M Sakai. “White-noise analysis in neurophysiology”. In: *Physiological Reviews* 72.2 (1992), pp. 491–505.

[43] V Negus. *The comparative anatomy and physiology of the nose and paranasal sinuses.* Edinburgh and Longon, Livingston, 1958.

[44] Kai Zhao et al. “Numerical modeling of turbulent and laminar airflow and odorant transport during sniffing in the human and rat nose”. In: *Chemical senses* 31.2 (2006), pp. 107–118.

[45] Kai Zhao et al. “Effect of anatomy on human nasal air flow and odorant transport patterns: implications for olfaction”. In: *Chemical senses* 29.5 (2004), pp. 365–379.

[46] Jacob Cohen. *Statistical power analysis for the behavioral sciences*. Routledge, 2013.

[47] Wei R Chen and Gordon M Shepherd. “Membrane and synaptic properties of mitral cells in slices of rat olfactory bulb”. In: *Brain research* 745.1-2 (1997), pp. 189–196.

[48] David Desmaisons, Jean-Didier Vincent, and Pierre-Marie Lledo. "Control of action potential timing by intrinsic subthreshold oscillations in olfactory bulb output neurons". In: *Journal of Neuroscience* 19.24 (1999), pp. 10727–10737.

[49] Ramani Balu, Phillip Larimer, and Ben W Strowbridge. "Phasic stimuli evoke precisely timed spikes in intermittently discharging mitral cells". In: *Journal of neurophysiology* 92.2 (2004), pp. 743–753.

[50] NE Schoppa and GL Westbrook. "Regulation of synaptic timing in the olfactory bulb by an A-type potassium current". In: *Nature neuroscience* 2.12 (1999), pp. 1106–1113.

[51] R Todd Pressler and Ben W Strowbridge. "Blanes cells mediate persistent feedforward inhibition onto granule cells in the olfactory bulb". In: *Neuron* 49.6 (2006), pp. 889–904.

[52] AR McQuiston and LC Katz. "Electrophysiology of interneurons in the glomerular layer of the rat olfactory bulb." In: *Journal of neurophysiology* 86.4 (2001), pp. 1899–1907.

[53] Sonya Giridhar, Brent Doiron, and Nathaniel N Urban. "Timescale-dependent shaping of correlation by olfactory bulb lateral inhibition". In: *Proceedings of the National Academy of Sciences* 108.14 (2011), pp. 5843–5848.

[54] R.F. Galán et al. "Correlation-induced synchronization of oscillations in olfactory bulb neurons". In: *The Journal of Neuroscience* 26 (2006), pp. 3646–3655.

[55] Haym Benaroya, Seon Mi Han, and Mark Nagurka. *Probability models in engineering and science*. Vol. 192. CRC press, 2005.

[56] A. Barreiro and C. Ly. "Practical approximation method for firing-rate models of coupled neural networks with correlated inputs". In: *Physical Review E* 96 (2017), p. 022413. DOI: 10.1103/PhysRevE.96.022413.

[57] C. Ly, W. Shew, and A. Barreiro. "Efficient calculation of heterogeneous non-equilibrium statistics in coupled firing rate models". In: *Journal of Mathematical Neuroscience* 9 (2019), p. 2. DOI: 10.1186/s13408-019-0070-7.

[58] J. de la Rocha et al. "Correlation between neural spike trains increases with firing rate". In: *Nature* 448 (2007), pp. 802–806.

[59] Jonathan W Pillow and Eero P Simoncelli. "Dimensionality reduction in neural models: an information-theoretic generalization of spike-triggered average and covariance analysis". In: *Journal of vision* 6.4 (2006), pp. 9–9.

[60] Jonathan W Pillow et al. "Spatio-temporal correlations and visual signalling in a complete neuronal population". In: *Nature* 454.7207 (2008), pp. 995–999.

[61] Jonathan W Pillow, Yashar Ahmadian, and Liam Paninski. "Model-based decoding, information estimation, and change-point detection techniques for multineuron spike trains". In: *Neural computation* 23.1 (2011), pp. 1–45.

[62] Johannes Frasnelli, Mary Ungermann, and Thomas Hummel. "Ortho-and retronasal presentation of olfactory stimuli modulates odor percepts". In: *Chemosensory Perception* 1.1 (2008), pp. 9–15.

[63] Krishnan Padmanabhan et al. "Centrifugal inputs to the main olfactory bulb revealed through whole brain circuit-mapping". In: *Frontiers in neuroanatomy* 12 (2019), p. 115.

[64] Foivos Markopoulos et al. "Functional properties of cortical feedback projections to the olfactory bulb". In: *Neuron* 76.6 (2012), pp. 1175–1188.

[65] Alison M Boyd et al. "Cortical feedback control of olfactory bulb circuits". In: *Neuron* 76.6 (2012), pp. 1161–1174.

[66] Gonzalo H Otazu et al. “Cortical feedback decorrelates olfactory bulb output in awake mice”. In: *Neuron* 86.6 (2015), pp. 1461–1477.

[67] Kevin M Cury and Naoshige Uchida. “Robust odor coding via inhalation-coupled transient activity in the mammalian olfactory bulb”. In: *Neuron* 68.3 (2010), pp. 570–585.

[68] Matt Wachowiak. “All in a sniff: olfaction as a model for active sensing”. In: *Neuron* 71.6 (2011), pp. 962–973.

[69] Dmitry Rinberg, Alex Koulakov, and Alan Gelperin. “Sparse odor coding in awake behaving mice”. In: *Journal of Neuroscience* 26.34 (Aug. 2006), pp. 8857–8865. ISSN: 02706474. DOI: 10.1523/JNEUROSCI.0884-06.2006.

[70] Michelle Craft and Cheng Ly. “The effects of background noise on a biophysical model of olfactory bulb mitral cells”. In: *Bulletin of Mathematical Biology* 84.10 (2022), pp. 1–20.

[71] B. Ermentrout and D.H. Terman. *Mathematical foundations of neuroscience*. Vol. 64. Springer, 2010.

[72] W. Gerstner and W. Kistler. “Spiking Neuron Models”. In: Cambridge, United Kingdom: Cambridge University Press, 2002. Chap. 5, pp. 147–163.

[73] Benjamin Lindner, André Longtin, and Adi Bulsara. “Analytic expressions for rate and CV of a type I neuron driven by white gaussian noise”. In: *Neural computation* 15.8 (2003), pp. 1761–1788.

[74] Srdjan Ostojic. “Interspike interval distributions of spiking neurons driven by fluctuating inputs”. In: *Journal of neurophysiology* 106.1 (2011), pp. 361–373.

[75] L Sacerdote, AEP Villa, and Cristina Zucca. "On the classification of experimental data modeled via a stochastic leaky integrate and fire model through boundary values". In: *Bulletin of mathematical biology* 68.6 (2006), pp. 1257–1274.

[76] A. Barreiro et al. "A theoretical framework for analyzing coupled neuronal networks: Application to the olfactory system". In: *PLoS Computational Biology* 13 (2017), e1005780. DOI: 10.1371/journal.pcbi.1005780.

[77] Ronit Shmuel, Lavi Secundo, and Rafi Haddad. "Strong, weak and neuron type dependent lateral inhibition in the olfactory bulb". In: *Scientific Reports* 9.1 (2019), pp. 1–11.

[78] C. Ly and D. Tranchina. "Spike Train Statistics and Dynamics with Synaptic Input from any Renewal Process: A Population Density Approach". In: *Neural Computation* 21 (2009), pp. 360–396. DOI: 10.1162/neco.2008.03-08-743.

[79] W. H. Nesse, A. Borisyuk, and P.C. Bressloff. "Fluctuation-driven rhythmogenesis in an excitatory neuronal network with slow adaptation". In: *Journal of Computational Neuroscience* 25 (2008), pp. 317–333.

[80] H. Risken. "The Fokker-Planck equation: methods of solutions and applications". In: New York, NY: Springer-Verlag, 1989. Chap. 1.

[81] C.W. Gardiner. *Handbook of stochastic methods*. Springer-Verlag, 1985.

[82] Ryan Viertel and Alla Borisyuk. "A Computational model of the mammalian external tufted cell". In: *Journal of theoretical biology* 462 (2019), pp. 109–121.

[83] Rainer W Friedrich and Gilles Laurent. "Dynamics of olfactory bulb input and output activity during odor stimulation in zebrafish". In: *Journal of neurophysiology* 91.6 (2004), pp. 2658–2669.

[84] Jean-Pierre Rospars et al. “Competitive and noncompetitive odorant interactions in the early neural coding of odorant mixtures”. In: *Journal of Neuroscience* 28.10 (2008), pp. 2659–2666.

[85] Adrian A Wanner and Rainer W Friedrich. “Whitening of odor representations by the wiring diagram of the olfactory bulb”. In: *Nature Neuroscience* 23.3 (2020), pp. 433–442.

[86] P. Zhou et al. “Impact of neuronal heterogeneity on correlated colored noise-induced synchronization”. In: *Frontiers in Computational Neuroscience* 7 (2013).

[87] S. Marella and B. Ermentrout. “Class-II neurons display a higher degree of stochastic synchronization than class-I neurons”. In: *Physical Review E* 77 (2008), p. 041918.

[88] Pamela B Pyzza et al. “Network mechanism for insect olfaction”. In: *Cognitive Neurodynamics* 15.1 (2021), pp. 103–129.

[89] Mainak Patel and Aaditya Rangan. “Olfactory encoding within the insect antennal lobe: The emergence and role of higher order temporal correlations in the dynamics of antennal lobe spiking activity”. In: *Journal of theoretical biology* 522 (2021), p. 110700.

[90] C. Ly and B. Ermentrout. “Analytic Approximations of Statistical Quantities and Response of Noisy Oscillators”. In: *Physica D* 240 (2011), pp. 719–731.

[91] Dan Wilson and Bard Ermentrout. “Augmented phase reduction of (not so) weakly perturbed coupled oscillators”. In: *SIAM Review* 61.2 (2019), pp. 277–315.

[92] Peter Ashwin, Stephen Coombes, and Rachel Nicks. “Mathematical frameworks for oscillatory network dynamics in neuroscience”. In: *The Journal of Mathematical Neuroscience* 6.1 (2016), pp. 1–92.

[93] K. CA Wedgwood et al. “Phase-amplitude descriptions of neural oscillator models”. In: *Journal of Mathematical Neuroscience* 3 (2013), p. 2.

[94] Peter J Thomas and Benjamin Lindner. “Asymptotic phase for stochastic oscillators”. In: *Physical review letters* 113.25 (2014), p. 254101.

[95] Justus TC Schwabedal and Arkady Pikovsky. “Phase description of stochastic oscillations”. In: *Physical review letters* 110.20 (2013), p. 204102.

[96] Cheng Ly and Brent Doiron. “Noise-enhanced coding in phasic neuron spike trains”. In: *Plos one* 12.5 (2017), e0176963.

[97] H. E. Plesser and W. Gerstner. “Noise in Integrate-and-Fire Neurons: From Stochastic Input to Escape Rates”. In: *Neural Computation* 12 (2000), pp. 367–384.

[98] RE Lee Deville, Cyrill B Muratov, and Eric Vanden-Eijnden. “Non-meanfield deterministic limits in chemical reaction kinetics”. In: *The Journal of chemical physics* 124.23 (2006), p. 231102.

[99] Brian Nils Lundstrom et al. “Sensitivity of firing rate to input fluctuations depends on time scale separation between fast and slow variables in single neurons”. In: *Journal of computational neuroscience* 27.2 (2009), pp. 277–290.

[100] HA Kramers. “Physica (Utrecht) 7, 284”. In: *MathSciNet ADS zbMATH* (1940).

[101] Luca Gammaitoni et al. “Stochastic resonance”. In: *Reviews of modern physics* 70.1 (1998), p. 223.

[102] B. Lindner. “Coherence and Stochastic Resonance in Nonlinear Dynamical Systems”. PhD thesis. Humboldt University of Berlin, 2002.

[103] Stefan Reinker, Ernest Puil, and Robert M Miura. “Resonances and noise in a stochastic Hindmarsh-Rose model of thalamic neurons”. In: *Bulletin of mathematical biology* 65.4 (2003), pp. 641–663.

[104] Stefan Reinker, Yue-Xian Li, and Rachel Kuske. "Noise-induced coherence and network oscillations in a reduced bursting model". In: *Bulletin of mathematical biology* 68.6 (2006), pp. 1401–1427.

[105] Tilo Schwalger and Lutz Schimansky-Geier. "Interspike interval statistics of a leaky integrate-and-fire neuron driven by Gaussian noise with large correlation times". In: *Physical Review E* 77.3 (2008), p. 031914.

[106] Izumi Fukunaga et al. "Two distinct channels of olfactory bulb output". In: *Neuron* 75.2 (2012), pp. 320–329.

[107] Jianhua Cang and Jeffry S Isaacson. "In vivo whole-cell recording of odor-evoked synaptic transmission in the rat olfactory bulb". In: *Journal of Neuroscience* 23.10 (2003), pp. 4108–4116.

[108] Shelby B Dietz and Venkatesh N Murthy. "Contrasting short-term plasticity at two sides of the mitral–granule reciprocal synapse in the mammalian olfactory bulb". In: *The Journal of physiology* 569.2 (2005), pp. 475–488.

[109] Rebecca Jordan et al. "Active sampling state dynamically enhances olfactory bulb odor representation". In: *Neuron* 98.6 (2018), pp. 1214–1228.

[110] Ze-Jun Wang, Liqin Sun, and Thomas Heinbockel. "Cannabinoid receptor-mediated regulation of neuronal activity and signaling in glomeruli of the main olfactory bulb". In: *Journal of Neuroscience* 32.25 (2012), pp. 8475–8479.

[111] KA Bolding and KM Franks. "Simultaneous extracellular recordings from mice olfactory bulb (OB) and piriform cortex (PCx) and respiration data in response to odor stimuli and optogenetic stimulation of OB". In: *CRCNS. org Date accessed: January* (2021).

[112] Kevin A Bolding and Kevin M Franks. "Recurrent cortical circuits implement concentration-invariant odor coding". In: *Science* 361.6407 (2018), eaat6904.

[113] Kevin A Bolding and Kevin M Franks. "Complementary codes for odor identity and intensity in olfactory cortex". In: *Elife* 6 (2017), e22630.

[114] C Rossant et al. "Spike sorting for large, dense electrode arrays." In: *Nature neuroscience* 19.4 (2016), pp. 634–641.

[115] UPINDER S Bhalla and JAMES M Bower. "Exploring parameter space in detailed single neuron models: simulations of the mitral and granule cells of the olfactory bulb". In: *Journal of neurophysiology* 69.6 (1993), pp. 1948–1965.

[116] Michele Migliore, Michael L Hines, and Gordon M Shepherd. "The role of distal dendritic gap junctions in synchronization of mitral cell axonal output". In: *Journal of computational neuroscience* 18.2 (2005), pp. 151–161.

[117] Xiao-Jing Wang. "Ionic basis for intrinsic 40 Hz neuronal oscillations." In: *Neuroreport* 5.3 (1993), pp. 221–224.

[118] Tsuyoshi Inoue and Ben W Strowbridge. "Transient activity induces a long-lasting increase in the excitability of olfactory bulb interneurons". In: *Journal of neurophysiology* 99.1 (2008), pp. 187–199.

[119] Lucia Cadetti and Ottorino Belluzzi. "Hyperpolarisation-activated current in glomerular cells of the rat olfactory bulb". In: *Neuroreport* 12.14 (2001), pp. 3117–3120.

[120] B. Ermentrout. *Simulating, Analyzing, and Animating Dynamical Systems: A Guide to XPPAUT for Researchers and Students*. SIAM, 2002.

[121] Eusebius J Doedel. "AUTO: A program for the automatic bifurcation analysis of autonomous systems". In: *Congr. Numer* 30.265-284 (1981), pp. 25–93.

[122] J. Rinzel and B. Ermentrout. "Analysis of Neural Excitability and Oscillations". In: *Methods in Neuronal Modeling: From Synapses to Networks*. Ed. by I. Segev. MIT Press, 1989, pp. 135–169.

[123] B. Ermentrout. “Type I membranes, phase-resetting curves, and synchrony”. In: *Neural Computation* 8 (1996), pp. 979–1001.